AD_____

Award Number: W81XWH-11-1-0121

TITLE: Noninvasive Spatially Offset and Transmission Raman Mapping of Breast Tissue: A Multimodal Approach toward the in Vivo Assessment of Tissue Pathology

PRINCIPAL INVESTIGATOR: Dr. Matthew Schulmerich

CONTRACTING ORGANIZATION: University of Illinois
                          Urbana, IL 61801

REPORT DATE: April 2012

TYPE OF REPORT: Annual Summary

PREPARED FOR: U.S. Army Medical Research and Materiel Command
              Fort Detrick, Maryland 21702-5012

DISTRIBUTION STATEMENT: Approved for public release; distribution unlimited

The views, opinions and/or findings contained in this report are those of the author(s) and should not be construed as an official Department of the Army position, policy or decision unless so designated by other documentation.

REPORT DOCUMENTATION PAGE

Public reporting burden for this collection of information is estimated to average 1 hour per response, including the time for reviewing instructions, searching existing data sources, gathering and maintaining the data needed, and completing and reviewing this collection of information. Send comments regarding this burden estimate or any other aspect of this collection of information, including suggestions for reducing this burden to Department of Defense, Washington Headquarters Services, Directorate for Information Operations and Reports (0704-0188), 1215 Jefferson Davis Highway, Suite 1204, Arlington, VA 22202-4302. Respondents should be aware that notwithstanding any other provision of law, no person shall be subject to any penalty for failing to comply with a collection of information if it does not display a currently valid OMB control number. **PLEASE DO NOT RETURN YOUR FORM TO THE ABOVE ADDRESS.**

1. REPORT DATE *(DD-MM-YYYY)* 01-04-2012	2. REPORT TYPE Annual Summary	3. DATES COVERED *(From - To)* 1 Apr 2011 - 31 Mar 2012

4. TITLE AND SUBTITLE	
Noninvasive Spatially Offset and Transmission Raman Mapping of Breast Tissue: A Multimodal Approach toward the in Vivo Assessment of Tissue Pathology	5a. CONTRACT NUMBER
	5b. GRANT NUMBER W81XWH-11-1-0121
	5c. PROGRAM ELEMENT NUMBER

6. AUTHOR(S)	
Dr. Matthew Schulmerich	5d. PROJECT NUMBER
	5e. TASK NUMBER
E-Mail: schulmer@illinois.edu	5f. WORK UNIT NUMBER

7. PERFORMING ORGANIZATION NAME(S) AND ADDRESS(ES)	8. PERFORMING ORGANIZATION REPORT NUMBER
University of Illinois Urbana, IL 61801	

9. SPONSORING / MONITORING AGENCY NAME(S) AND ADDRESS(ES)	10. SPONSOR/MONITOR'S ACRONYM(S)
U.S. Army Medical Research and Materiel Command Fort Detrick, Maryland 21702-5012	
	11. SPONSOR/MONITOR'S REPORT NUMBER(S)

12. DISTRIBUTION / AVAILABILITY STATEMENT
Approved for Public Release; Distribution Unlimited

13. SUPPLEMENTARY NOTES

14. ABSTRACT
Abstract on next page.

15. SUBJECT TERMS
Subject terms on next page.

16. SECURITY CLASSIFICATION OF:			17. LIMITATION OF ABSTRACT	18. NUMBER OF PAGES	19a. NAME OF RESPONSIBLE PERSON USAMRMC
a. REPORT U	b. ABSTRACT U	c. THIS PAGE U	UU	72	19b. TELEPHONE NUMBER *(include area code)*

14. ABSTRACT

The purpose of this research project is to develop new approaches that can impact early diagnosis of breast cancer, post-biopsy analysis, lymph node examinations, and drug delivery studies. The scope of this training involves optimizing Raman instrumentation and methods for efficient illumination and collection of Raman scattered light originating from deep within breast tissue. Experiments encompass designing tissue phantoms using Intralipid®, dyes/pigments, inclusions, and agarose gel to quantitatively characterize the instruments' capabilities and performance. Additionally, we conduct spectroscopy on tissue biopsies to correlate spectral bands with healthy and diseased breast tissue. Observed spectral changes are compared to infrared images and H&E/HIS-stained images to relate observed biochemical changes to histology. The Raman data will be used to generate and train classification algorithms for automated histopathology as a starting point for in vivo work at the culmination of this training program. This report outlines progress for year 1 of the 3 year training program. In the approved statement of work 5 tasks were stated. All 5 tasks were successfully completed. We now have a working relationship with local clinicians. We have built-up a comprehensive database consisting of micrographs and IR spectral images for identify breast tissue histology and tissue chemistry. We have acquired Raman measurements on biopsied tissue. We have identified Raman spectral bands that can be used for distinguishing between different tissue types and have applied those Raman spectral bands to achieve cell-level contrast in Raman spectral images. Additionally, we have used clinical observations and interaction with clinicians to develop a conceptual design for a Raman Tomography instrument aimed at breast cancer screening. Finally for Raman tomographic reconstruction, we have evaluated existing diffuse optical tomography algorithms specifically for Raman measurements and have adapted a Monte Carlo framework for our Raman tomographic reconstruction. Through modeling and experimentation we characterized different instrument configurations and have implemented the transmission fan style configuration into our prototype instrument design which uses fiber-optics in-contact with tissue to give the maximum collection efficiency.

15. SUBJECT TERMS

Raman Spectroscopy, Breast Cancer, SORS, Transmission spectroscopy, Raman Tomography, Raman Imaging, Infrared Imaging

Table of Contents

INTRODUCTION: The **subject** of this research is to develop non-invasive optical instrumentation and methods for obtaining chemical contrast from deep within breast tissue. The overarching goal of this training program is to become steeped in breast cancer clinical practice and research to independently develop a new technology from a concept. My learning objectives include the following: first, fill in the gaps in my basic knowledge of breast cancer and pathology. Second, build a knowledge base as to the chemical changes that are occurring within breast tissue and how those changes are reflected in the vibrational spectra. Third, to understand the optics of breast tissue to gain most efficient illumination and collection schemes for instrumental design. The **purpose** of this research project is to develop new approaches that can impact early diagnosis of breast cancer, post-biopsy analysis, lymph node examinations, and drug delivery studies. Additionally, this technology could be used to study animal models for tissue engineering, 3D tissue scaffolds and has a variety of other basic research as well as clinical applications. The **scope** of this training involves optimizing Raman instrumentation and methods for efficient illumination and collection of Raman scattered light originating from deep within breast tissue. Experiments encompass designing tissue phantoms using Intralipid®, dyes/pigments, inclusions, and agarose gel to quantitatively characterize the instruments' capabilities and performance. Additionally, we conduct spectroscopy on tissue biopsies to correlate spectral bands with healthy and diseased breast tissue.   Observed spectral changes are compared to infrared images and H&E/HIS-stained images to relate observed biochemical changes to histology. The Raman data will be used to generate and train classification algorithms for automated histopathology as a starting point for *in vivo* work at the culmination of this training program.

BODY: The approved statement of work is illustrated in figure 1. For year one, five tasks were outlined. All tasks have been completed and we are able to begin the work outlined for year 2 as scheduled. Details of the work conducted in year one are present on the following pages.
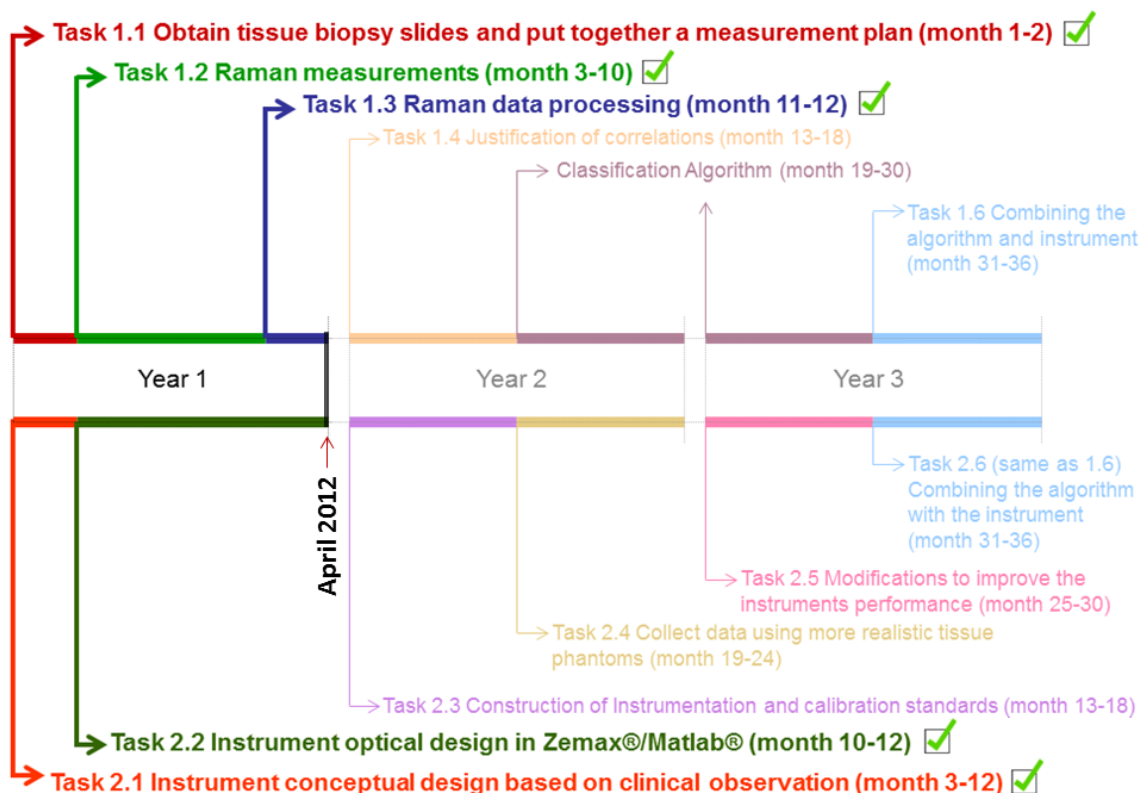

Figure 1) Summary figure and timeline for approved statement of work

Task 1.1 Obtain tissue biopsy slides and put together a measurement plan (month 1-2): This task was successfully completed. Tissue samples were obtained from Provena covenant medical center and US Biomax, Inc (IRB approved sources). 101 breast tissue biopsies cores (1mm) were obtained. Diagnosis were hyperplasia (n=20), Dysplasia (n=20), Melignant Tumor (n=40), Normal (n=11). Serial sections of these biopsies were stained and imaged to establish a database of micrographs that could be used to identify cell types and regions of interest in the tissue. The stains used for identifying tissue histology were carefully chosen upon consultation with two pathologists. The histological stains used were as follows:

No Stain For Raman –Serial Section 261
P53–Serial Section 262
Ki67–Serial Section 263
CD31–Serial Section 264
P63–Serial Section 265
No Stain For IR–Serial Section 266
H&E–Serial Section 267
Calponin –Serial Section 268

Masson's Trichrome–Serial Section 269
Vimentin–Serial Section 270
Smooth Muscle Actin–Serial Section 271
HMW Cytokeratin–Serial Section 272
No Stain For IR–Serial Section 273
Her2/neu–Serial Section 274
Estrogen Receptor–Serial Section 275
Progesterone Receptor–Serial Section 276

For each biopsy we built a database of micrographs that can be zoomed to a 20x magnification. A set low magnification serial sections are depicted in figure2 showing the different staining results.
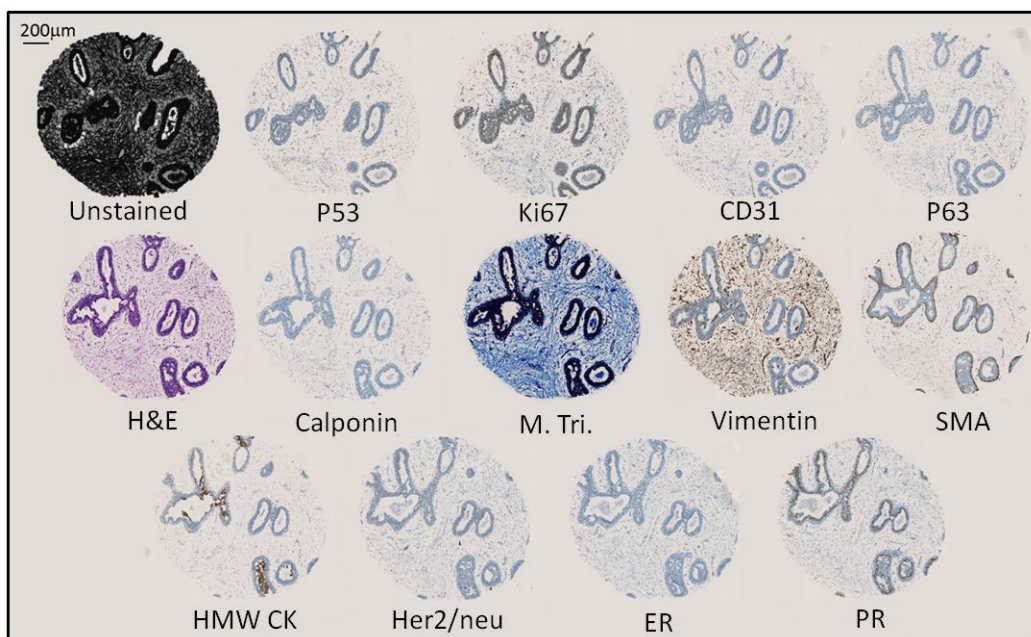

Figure 2) Serial sections and staining obtained for each breast tissue biopsy

In addition to stained serial sections we also acquired mid-infrared images from each of these biopsies. Some of our mid infrared results is reported in the manuscript 'High Definition Spectroscopic Imaging' attached in the appendix of this report. An example of an infrared spectral image is depicted in figure 3. These images are useful in working with pathologists in order to evaluate histology and pathology. We used this electronic database of infrared and white light micrographs to identified regions of interest for Raman measurements. Regions of interest were selected by correlating the tissues chemistry with the observed tissue staining to select different tissue types i.e.) distinguishing epithelial cells from myoepithelial cells.
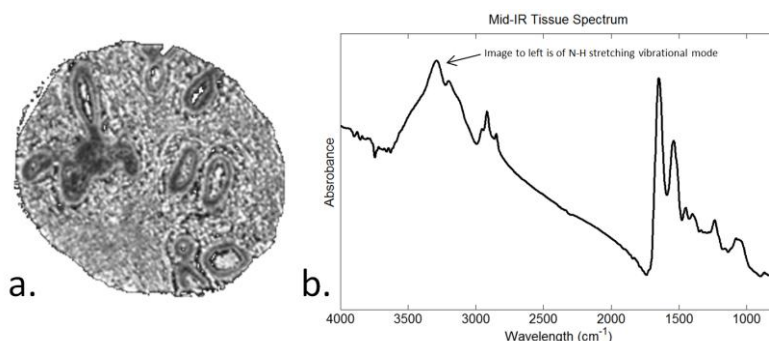

Figure 3) a) Infrared image of using the Amide A band for contrast b) representative mid IR spectrum illustrating the information available for contrast at each pixel in this image.

Task 1.2 Raman measurements (month 3-10): We have successfully completed this task. Raman spectra were acquired on a Horiba LabRam microscope using a video reference to mark the position of each measurement. Spectra were obtained using 785nm excitation with a 100x 0.90NA microscope objective. Acquisitions range from 15 to 60 seconds per measurement point depending on signal to noise. Spectra were acquired at a spectral resolution between 5 and 10 cm^{-1}.
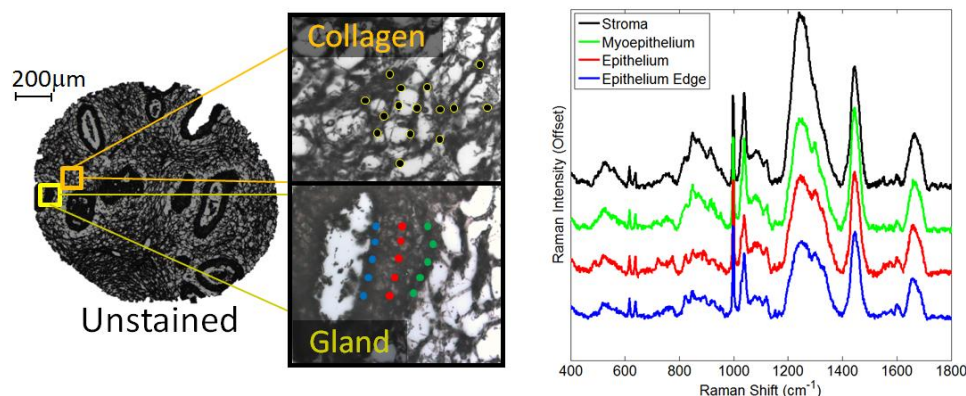

Figure 4) Raman spectra were collected from select regions within each biopsy core and compared based on tissue type.

Raman Band (cm^{-1})	Major Assignments	Weighted towards
622	C-C twisting mode phenylalanine	Epithelium
643	C-C twisting mode tyrosine	Epithelium
781	Cytosine/Uracil ring breathing	Epithelium
828	Ring breathing tyrosine/O-P-O stretch	Epithelium
854	Tyrosine ring breathing	Stroma
936	C-C stretch Proline, Valine, and protein backbone (a-helix)	Epithelium
1003	Symmetric ring breathing mode phenylalanine	Epithelium
1032	C-H in plane bending mode phenylalanine	Epithelium
1085	C-N stretch	Stroma
1126	C-N stretch	Epithelium
1156	C-C & C-N stretching	Epithelium
1205	Tryptophan & Phenylalanine n(C-C$_6$H$_5$)	Epithelium
1240-1265	Amide III	Stroma
1310	CH$_3$CH$_2$ twisting mode	Epithelium
1333	CH$_3$CH$_2$ wagging mode	Epithelium
1450	CH$_2$ bending mode	Stroma

We acquired Raman spectra from strategic locations on all biopsy cores that were available on serial section 261 (see page 5). We also acquired Raman measurements from surgical resections that were provided through Provena medical center. The primary focus of our measurements was in distinguishing different tissue types in anticipation of developing an algorithm classifier. Figure 4 illustrates an example of point measurements collected on regions of interest within a biopsy section. A representative example of the data collected for each biopsy core is depicted in figure 4. All spectra in figure 4 were baselined and normalized to the phenylalanine band at 1003 cm^{-1}.

Figure 4 illustrates very clearly that different tissue types can be identified by observing the differences in Raman bands. For example, the black spectrum, collected over stromal tissue, has a much larger amide III Raman band (1244 cm^{-1} and 1274 cm^{-1}) than epithelial or myoepithelial tissue. This band is correlated with a C-N and N-H vibrational modes and can be used for contrast to distinguish epithelial tissue from stromal tissue. Additionally the band at 1045 cm^{-1} also has a larger

relative contribution in the stromal and myoepithelium tissue over epithelium. Some specific spectral band weightings are listed in the table below figure 4. Validating the exact position of a measurement was difficult as the tissue structure changed slightly in sequential serial sections and as a result this contrast is some-what difficult to visualize by point measurements.

To overcome this difficulty, we have also begun acquiring Raman spectral images that allow us to more reliably identify where a Raman spectrum originates from relative to the surrounding tissue. Using the Raman spectrum for contrast and having the positional correspondence of many Raman spectra, we are able to visualize the tissue structure and pull out average differences in tissue types. While we have begun work on a tissue classifier, we anticipate continued effort in the Raman imaging approach to be useful in both building and validating our classification algorithms.

An example of a Raman spectral image is illustrated in figure 5. The top right image illustrates a Raman spectral image over-laid on an unstained biopsy micrograph. The primary contrast in this image is achieved using the band at 1045 cm^{-1}. By correlating the position of the image with stained biopsy serial sections in our database, it is clear that we can distinguish epithelium, stroma, and myoepithelial cells without dyes or label. This is a significant finding because myoepithelial cells makeup the basal layer of normal mammary epithelial tissue. Their identification has particular diagnostic value as they are lost in malignancy but retained in most benign lesions. Quantification of these cells *in vivo* could play a key role in identifying invasive carcinomas.
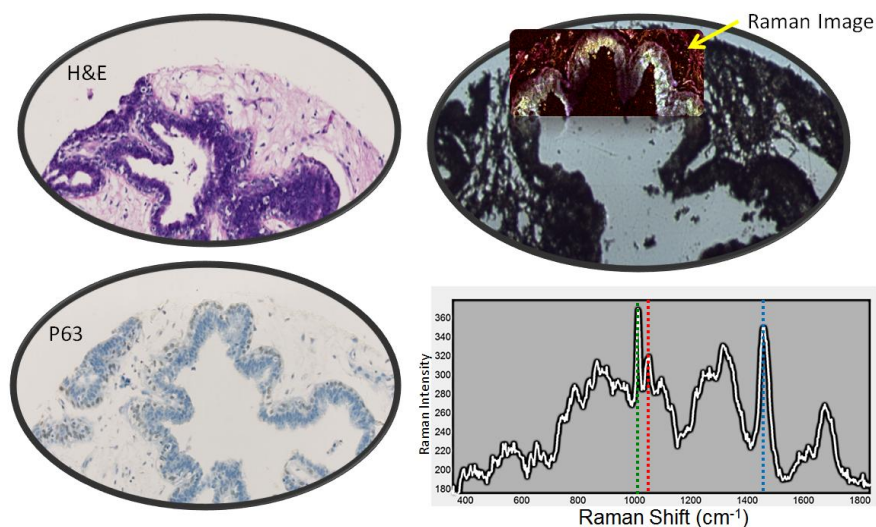

Figure 5) Raman spectral image compared to stained biopsy sections

Task 1.3 Raman data processing (month 11-12): Spectral processing involved calibrating the wavelength axis against a neon atomic emission lamp and using a NIST traceable white light source to correct for the instruments wavelength response. The Raman spectra were then imported into Matlab® and examined for cosmic rays (spikes). If spikes were found they were removed by using a median filter on adjacent points to determine an interpolating reference. The spike were then deleted and replaced by interpolating data points from both sides of the spike to fill in the gap. Baseline points on the data were identified and used for all spectra analyzed. Using these same baseline points a multi-linear baseline was then fit to the data and subtracted to provide baselined Raman spectra. The spectra were then normalized either by overall area or to specific band areas.

Several algorithms and visualization approaches were developed for this work and have been reported in the manuscript ''Designing Transfer Functions for Interactive Data Mining of Hyperspectral Images'' which is attached in the appendix of this report.

Task 2.1 Instrument conceptual design based on clinical observation (month 1-2):

Dr. Krishna Tangella M.D. who is Teaching Faulty at the University of Illinois at Urbana-Champaign College of Medicine has spent the year with me in a one-on-one course in Breast Cancer pathology. Over this year I have built-up my fundamental understanding of breast cancer. I've worked closely with the pathology team at Provena Covenant medical Center in Urbana, IL. In working with this team I've been fortunate to observe many aspects of clinical practice associated with breast cancer. I've observed screening with MRI and mammography as well as ultrasound guided biopsies. I've seen the processing that occurs when a biopsy is section and prepared for histological staining. Additionally, I've observed grossing procedure conducted on tissue from mastectomies. I was also fortunate to attend a week long intensive Breast Imaging course covering clinical breast imaging that was provided by the International Institute of Continuing Medical education (iiCME). This course was extremely useful in understanding current radiology practices and was very motivating as spectroscopy was brought-up as a future technology of interest!

Based on these observations and experiences, we developed conceptual design for a Raman based screening instrument as depicted in figure 6.
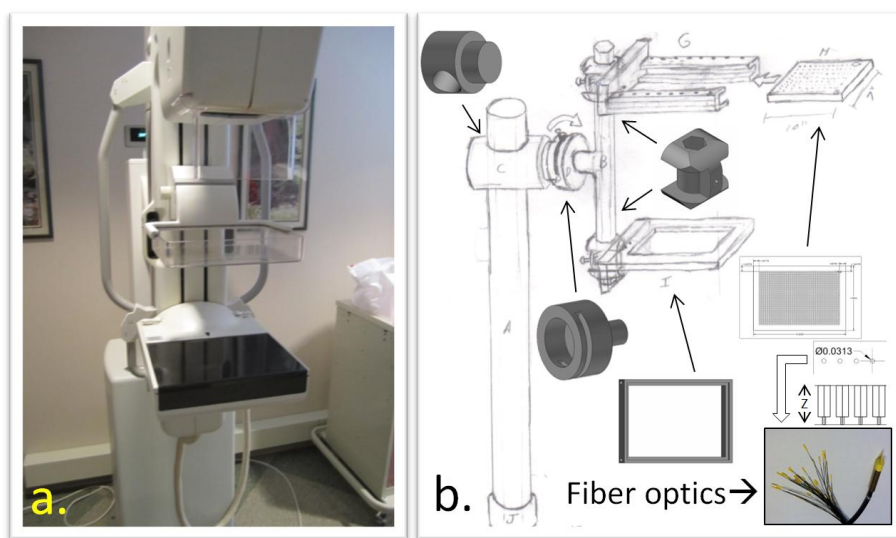

Figure 6) a) Photo taken at Provena Covenant Medical Center of a mammogram instrument b) Conceptual Design and AutoCAD files for a Breast Cancer Screening Raman Instrument

The instrument design is comprised of a stand that couples two breast paddles to an optical table. The stand has vertical and rotational motion to adjust to patient height and allow for multiple projections through the breast tissue. Both breast paddles are removable and can be made compatible with existing mammogram instruments. The bottom breast paddle has a transparent glass plate that is used to compress the breast tissue and will allow the Raman excitation source to illuminate the bottom of the breast. The light transmitted through the breast is collected by fiber optics on the top paddle and is then relayed to an imaging Raman spectrometer. This data is then

used reconstruct the size, shape, and position of features using the innate chemical contrast in the breast tissue. For this training program years 2 and 3, we will build and test this instrument using tissue phantoms (physical breast models that have similar optical properties to breast tissue).

Task 2.2 Instrument optical design (month 3-12):

A transmission approach to illumination and collection has proven to be the most robust approach to diffuse optical tomography where as other methods, a back scattered configuration for example, are known to have reconstruction artifacts like higher surface weightings of reconstructed targets[1]. To explore and understand the use of transmission Raman measurements in tomographic reconstructions we conducted a series of experiments and modeling to aid in instrument design. We compared two forward-modeling methods, radiative transport calculation (via Nirfast, an open-source diffuse optical tomography modeling package) and Monte Carlo simulation (written in-house), for the modeling of light fluence in the phantom. Reconstruction of the size and position of buried targets was attempted via an iterative modified-Tikhonov minimization algorithm without the use of spatial priors. The results are validated against computed tomography (CT) images of the same samples.

Phantom Specimens and Fabrication
Tissue phantoms were fabricated by dissolving 1 gram of agar (Sigma-Aldrich) in 50 ml of water at 95°C. Different volumes of 20% Intralipid (Sigma), an oil emulsion that is commonly used to mimic the scattering properties of fatty tissue,[2, 3, 4] were added to increase the scattering potential. 0.25ml or 1.25ml per 50ml of water were added to produce phantoms of total Intralipid concentration 0.1% or 0.5% by volume. A 0.1% concentration of Intralipid represents the lower limit of what is opaque to the naked eye, while a 0.5% solution close to the scattering level exhibited by epithelial tissue.[5, 6] The solution was poured the wells of a cell culture plate. One PTFE sphere of 1/8" diameter or two spheres of 1/16" diameter were suspended in each well by thin histology needles, and the plate was allowed to cool in a refrigerator for approximately one hour. The resulting phantoms were cylindrical, 1 cm in diameter and approximately 2 cm tall. Each sphere was positioned such that its middle sat approximately 1.2 cm above the base of the phantom. The radial position of the spheres, as well as the distance between two spheres embedded in the same phantom, were experiment-dependent.

Raman Instrumentation
The instrument comprised of a 785 nm excitation laser (barrowed for these experiments) and CCD-coupled spectrometer with a pre-stage notch filter, a fiber-optic bundle detector and a motorized rotation stage, as shown in Figure 7. In all cases, the laser and detector were held at a constant height at the level of the PTFE target while the cylindrical phantom was rotated about its vertical (symmetrical) axis. This allowed for a single source/detector combination to sample the phantom from multiple angles, a requirement of optical tomography. [7]

The 400mW CW laser at 785nm (Invictus, Kaiser) was fiber-launched and passed through a collimator to produce a 1.25 mm diameter beam. In all cases, this beam was centered on the waist of the phantom at the height of the target. Collection was performed via two achromatic doublets which focused the photons exiting from the phantom onto a 50-fiber bundle (100 um diameter each, in an approximately 5x10 array) (Fibertech Optica, Kitchener, Ontario, Canada). The focal lengths of these achromats were 60mm (focusing) and either 75mm or 200mm (collection) depending on the experiment. The output of the fiber bundle was imaged onto a spectral CCD (iDUS, Andor

Technology, Belfast, Northern Ireland). The motorized rotation stage (NR360S, ThorLabs, Newton, New Jersey), controlled by LabView (National Instruments, Austin, Texas), was stepped clockwise in 4.5 degree increments in all experiments for a total of 80 discrete sampling angles.
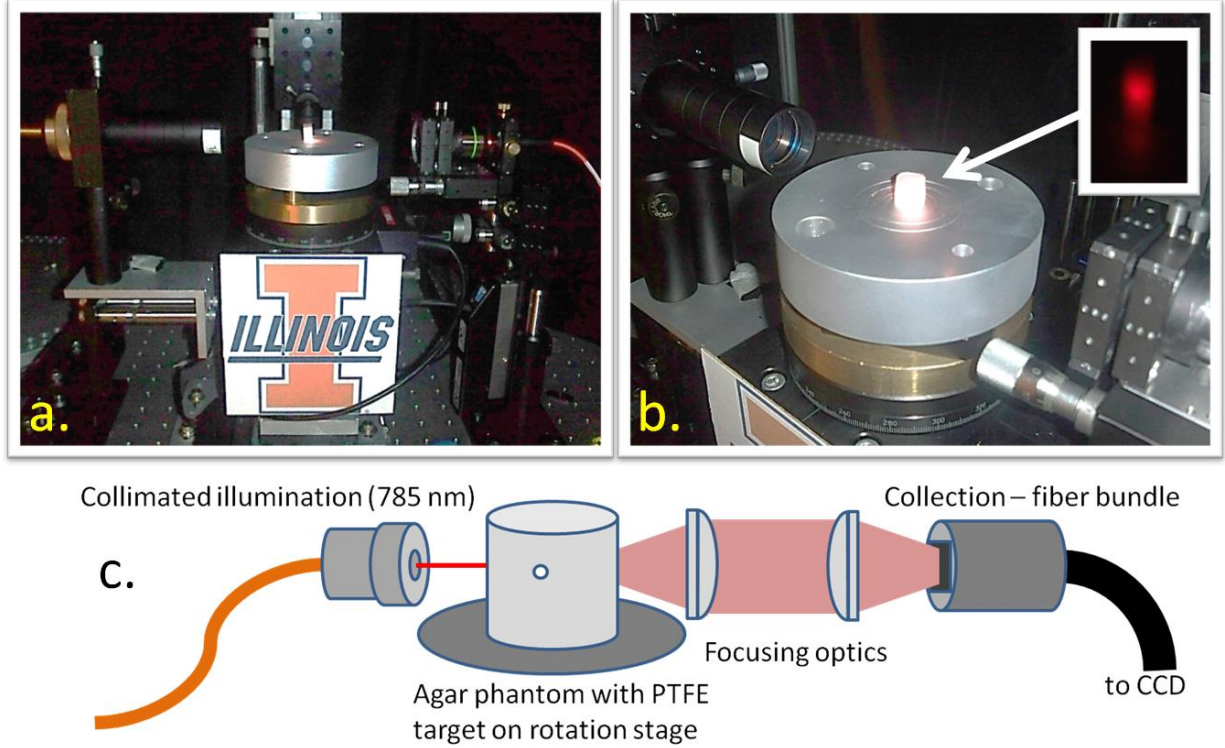

Figure 7) a.) and b.) Photos and c.) schematic of Raman tomography instrumentation. Both the illumination and collection fibers are centered on the phantom at the height of the PTFE sphere target.

Experiments

For phantoms containing a single target, three separate instrumentation configurations (as shown in Figure 7 were considered. In the first, shown in Figure 8a, the source and detector were kept at a 180° angle while the phantom was rotated through 80 positions to demonstrate the insufficiency of using a single source-detector angle. Acquisition time was three minutes per step (two frames of 90 seconds each to aid in data processing). The second experiment involved varying the angle between the source and detector, shown in Figure 8b. In addition to 180 degrees, the source was moved relative to the detector to form angles of 135, 90, and 45 degrees. This setup mimics the "circular fan-beam" geometry which is commonly used in diffuse optical tomography experiments.[1] For each source position, the stage was rotated through the full 80 steps and two spectra of 30 seconds each (as opposed to 90 seconds) were acquired at each step. In the final configuration, the source/detector angle was returned to 180 degrees, but the achromatic collection lens nearest to the phantom was replaced with one of focal length 200mm as shown in Figure 8c. The entire detector setup was moved an appropriate distance away from the phantom to keep the fibers in focus. This expanded the collection region from an area of approximately 0.97 mm x 1.3 mm to 2.9 mm x 3.8 mm with the intent of being able to collect spatial information from each individual fiber. This fan-like
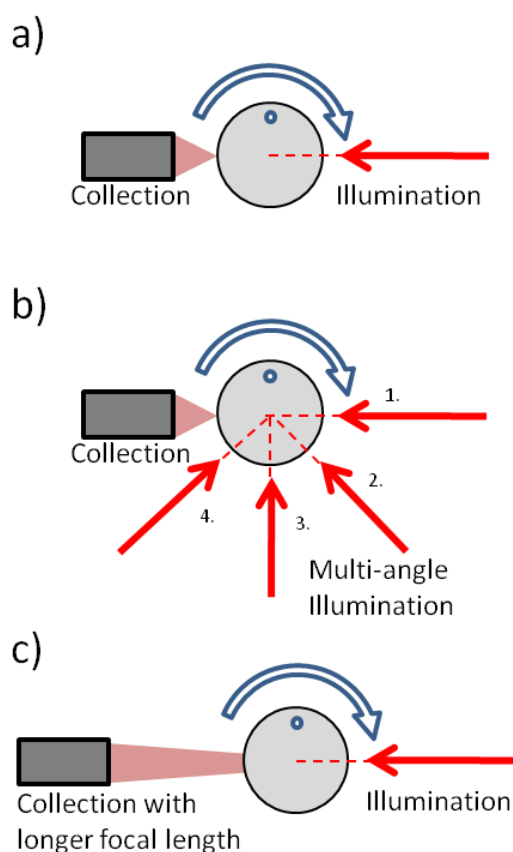
Figure 8) Three instrumentation configurations corresponding to the three experiments performed. a) Illumination and collection are fixed at a 180 degree angle. Measurements are taken as the phantom is rotated in 80 steps of 4.5° each. The fiber bundle is treated as a point detector for 80 total measurements. b) Multiple scans are taken with the source forming four positions with the detector (180°, 135°, 90° and 45°). The total number of measurements taken is 320 (4 x 80). c) Illumination and collection are fixed at a 180° angle as in setup a), but the focal length of the collection has been increased from 75 mm to 200 mm. As a result, the total area of collection is larger and the fiber bundle can no longer be treated as a point detector – the signals from (ten) individual fibers were evaluated for 800 total data points.

geometry was chosen to mimic the cone-beam transmission computed tomography (CT) source-detector configuration.[8]

A series of experiments involving phantoms with two PTFE spheres were also performed. Using the instrument setup with the longer focal length collection (experiment seen in figure 8c) and an additional 30 mm focal length lens to focus the collimated illumination beam in an approximation of a point source (see later discussion), the response from two spheres was investigated. Additionally, a third series of experiments in which the Intralipid content of the two-sphere phantoms was increased to 0.5%, was performed in the same manner with two spheres and a longer focal length. The quality of the reconstructions was evaluated by comparison to micro-CT images showing absolute sphere positions.

Data Processing

Zemax was used to model some of the optical configurartions, while matlab was found to be more useful in the tomographic reconstructions. All data processing was done in Matlab R2009b (The MathWorks, Nantucket MA). A median filter was applied to all collected data to correct for the cosmic ray 'spikes' which appear on the CCD. The two Raman bands of interest are PTFE (732 cm^{-1}) and Intralipid (~800-820 cm^{-1}). As with the biopsy Raman measurements, a multilinear "rubber band" baselining procedure was used to remove the background, and the area under each band was calculated. During reconstructions, both the absolute intensity of the PTFE signal and that of the Intralipid signal are utilized. The intensity of the Intralipid band is directly proportional to the number of photons reaching the detector for that measurement, and can be considered an internal standard which accounts for any discrepancies in the distance between source and detector or in the amount of light collected. In high-scattering samples where the Intralipid band is obscured by noise,

the band's value is approximated as being proportional to the average intensity of the entire CCD chip.

Computerized Tomography Reconstruction
Nirfast [www.dartmouth.edu/~nir/nirfast], is an open-source software package for simulation of DOT experiments and for DOT reconstructions from real or simulated data.[9] Based on a finite-element method for calculating photon fluence though specified geometries, the two processes that can be modeled (NIR absorbance and fluorescence emission) can be seen as analogous to Raman scattering events (conversion of Rayleigh scattered to Stokes scattered light). While the physical processes behind these two are not the same, they are similar enough to warrant the use of Nirfast as a first approximation for 2D reconstructions from experimental Raman data. For reconstructing experimental data, a circular finite element mesh was generated within the program. Source and detector locations were added to match each experimental setup, and the experimental data were ordered and normalized to match the range of the signal from a forward simulation of a 'blank' mesh with no absorbing target.

Also evaluated was a Monte Carlo simulation written in-house for modeling photon fluence. Using a 2D pixel mesh, the reconstruction mathematics and assumptions conserved between the two methods. Although more computationally intensive, Monte Carlo simulations allow the user to overcome certain assumptions made by the radiative transport equation (including the use of a non-idealized point source, implementation of geometrically-accurate detectors, and photon migration that does not follow the diffusion regime) which may not be appropriate for certain Raman experiments. Monte Carlo studies which simulate the generation and propagation of Raman photons through turbid media have been performed recently.[10, 11, 12] In a similar manner, we compare the results of Monte Carlo simulations to those of Nirfast to show that the physical processes that govern Raman tomography experiments differ significantly from DOT experiments and that these two modalities need to be treated as separate entities.

Results from these experiments

A: Radiative transport calculations (NIRFAST)
Figure 9a illustrates the simplest configuration and the recorded Raman signal of a PTFE sphere relative to Intralipid as a function of rotation (Figure 9b). Two maxima are observed: one when the target passes the source and another when the target passes the detector. These two maxima are spaced by approximately 180º, which is explained by uniform rotation of the target through 360º. In-between the two maxima, no Raman signal is observed; the collected photon count at these points is below the spectrograph's limit of detection.

Each of the 50 fibers from the detector is mapped onto a different region of the CCD camera, and the response from each fiber can be individually determined. The behavior of individual fibers (detectors) set along the waist of the phantom would be similar to the results seen in Figure 9b: the PTFE target will pass by each fiber and the source during rotation, resulting in two maxima with slight position shifts as a result of fiber position. If the fibers are all packed closely together, we expect this difference to be minimal; if the fibers are spaced at larger intervals, this difference will be much more pronounced. Figure 9c plots each fiber's (48 total) center of gravity for the second maximum (when the target is closest to the detector) as a function of phantom rotation. The fibers show a standard deviation of 3.1 degrees, indicating that the majority of the fibers 'see' the target
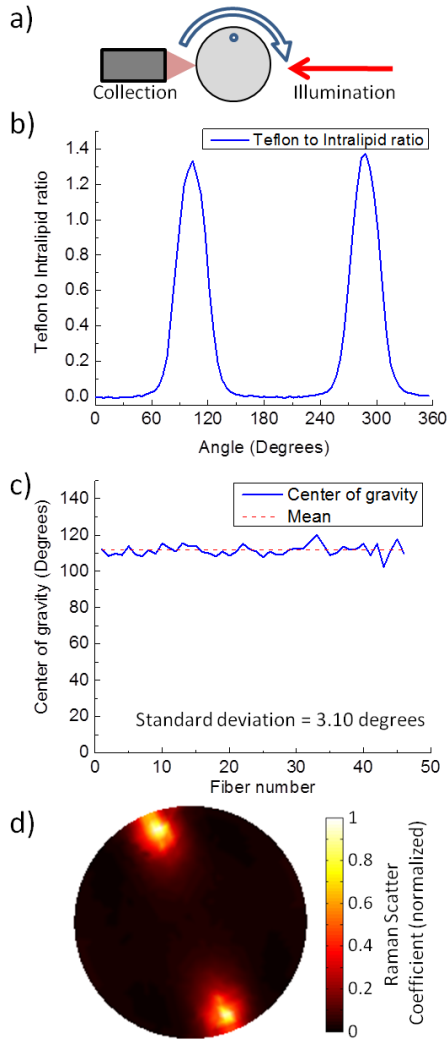
Figure 9) a) Schematic of 180° setup, including the direction of rotation and the approximate starting position of the PTFE target relative to the source and detector. b) PTFE to Intralipid Raman photon ratio as a function of phantom rotation, average of all fibers. Distinct increases in signal occur when the target passes the source or the detector. c) Center of gravity measurements for each fiber-optic in the detector bundle. Due to the small spacing of fibers, little variation is seen in the position of the second peak as seen by each individual fiber. d) Reconstruction from Nirfast. Data predicts two targets at opposite ends of the phantom.
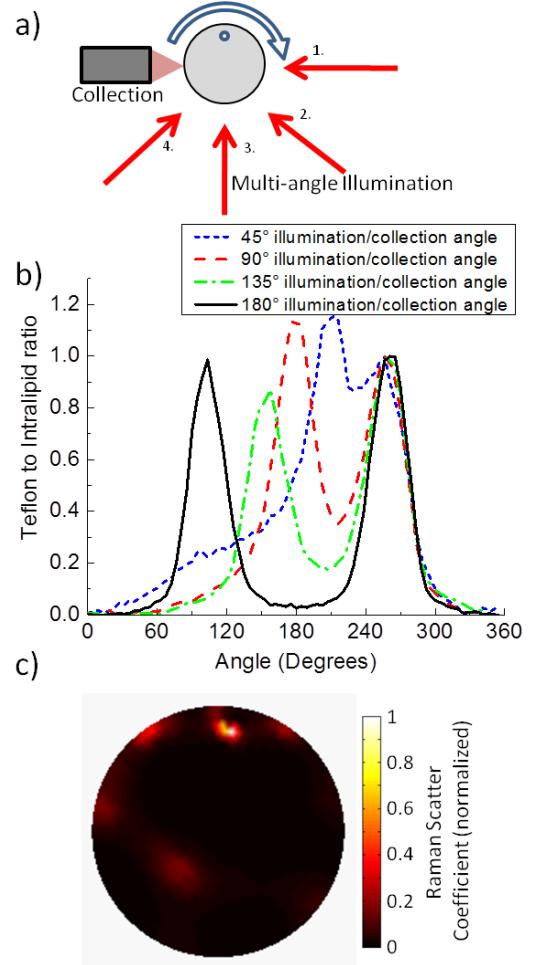
Figure 10) a) Schematic for the multi-angle setup, including the direction of rotation and the approximate starting position of the PTFE target relative to the sources and detector. b) PTFE to Intralipid Raman photon ratio as a function of both phantom rotation and source/detector angle. Signal maxima occur when the target passes near the source or the detector. As expected, the four peaks representing the target passing the detector are separated by about 45 degrees each. c) Reconstruction from Nirfast. Even though there are shadows, the data correctly predicts the location of the target. These shadows are due to normalization errors and deviations from point source illumination.

pass by within six degrees of rotation. This small variation is to be expected because the assembly's collection area spans one square millimeter, contributing a very small angular response of less than three degrees. The two maxima (target near source and target near detector) are similar in height, width, and shape. Without angular information it is not obvious how to distinguish one from the

14

other. Performing a 2D reconstruction on the data with Nirfast, as shown in Figure 9d, confirms this observation: the program predicts two targets separated by 180 degrees. This result reinforces the well-accepted notion that multiple collection angles are needed to accurately determine the position of targets buried in scattering analyte.[1]

Figure 10 displays Raman signal versus rotation angle for multiple source locations ("circular fan-beam" geometry). The data have been normalized to the second maxima (when the phantom is nearest to the detector). As in the previous example, each full rotation shows two maxima corresponding to when the target passes the source and the detector. While the 180º configuration shows a separation of roughly 180º, the other angles show corresponding separations close to 135º, 90º and 45º. It is clear that the maxima corresponding to the target passing the detector do not change in position. The Nirfast reconstruction in Figure 10c supports the observation that multiple illumination/collection angles gives greater insight as to the location of the target.
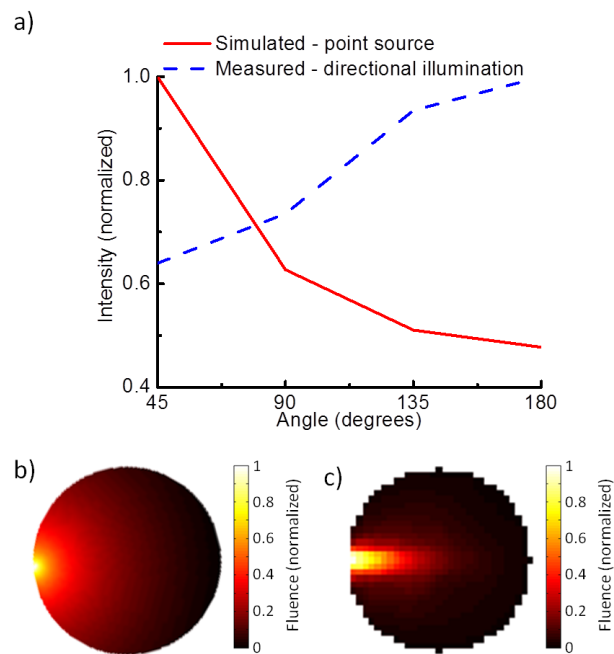

Figure 11) a) Illumination fluence at the phantom border at four different angles relative to the point of illumination. Solid line: calculated fluence from the radiative transport equation. Dashed line: measured fluence using a tissue phantom (0.1% Intralipid, no targets). b) Illumination structure for an idealized point source. c) Ray tracing simulation showing the illumination structure for a directionalized laser source.

Although one target is predicted, 'shadowing' occurs in regions not occupied by the target. The primary cause of this stems from a discrepancy between how illumination is modeled and how the phantom is actually illuminated by our instrument. The radiative transport equation is forced to assume a perfect point source for illumination – for measurements over long distances with samples with high scattering coefficients and fiber-launched illumination in contact with the sample, the effective angle of illumination is very large and, after travel, many scattering events will occur, making a point-source illumination approximation very appropriate. In this experiment, a collimated beam is used as the source, meaning that the illumination is highly directionalized within the sample.

a)

Collection with
longer focal length   Illumination
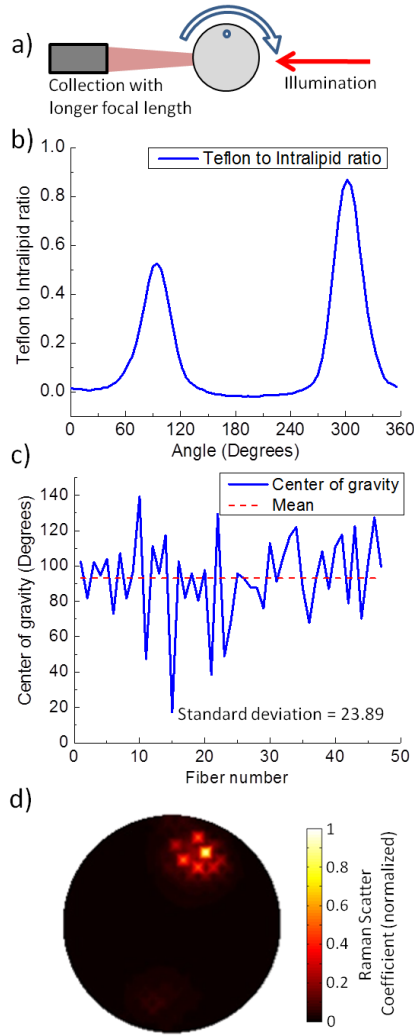
b)

c)

d)

Figure 12) a) Schematic indicating a longer detector focal length and, in turn, a larger collection area by the detector. b) PTFE to Intralipid Raman signal ratio averaged over all fibers. Due to the larger area of collection, the peak corresponding to the target passing the detector is broader than the peak corresponding to the target passing the source. c) Fiber optic center of gravity is much more varied when the area of collection is increased, possibly leading to more angular information during collection. d) Nirfast reconstruction using 10 individual fibers spanning the length of the fiber pattern per rotation angle. One target is predicted with no shadowing.

The difference between these two models is illustrated in Figure 11a, which compares the photon fluence at four points on a homogeneous phantom as simulated in Nirfast and measured using the experimental setup. It is immediately apparent that these two models are not equivalent. With a point source illumination, photon density at any position in the phantom is directly proportional to the distance from the source. Collection at 45o relative to the source is more intense than 90o, etc. In the experimental setup, fluence is greatest at a collection point 180o relative to the source, which is the exact opposite of the simulation. In this particular experimental setup, the source directionality, scattering level, and measurement distance are such that the assumption of photon diffusion behavior does not hold.

This presents an interesting problem when working with measurements where the source and detectors are positioned at multiple sets of angles. The structure of illumination within the specimen is fundamentally different between simulation and experiment to the point where the radiative transport equation fails to describe the system when a wide range of source-detector angles are utilized. Figure 11b shows the illumination structure for a point source as determined by the radiative transport equation and Figure 11c shows an example of a collimated laser source as determined by a ray tracing simulation. While the fluence in regions between the source and detectors at angles smaller than 180° is highly dependent on the choice of model, the fluence at detector positions with angles very close to 180° are very similar to one another in both models. As such, it can be argued that, for detector positions close to and centered around 180° relative to the source, a point source approximation may be suitable for the experimental setup's collimated beam illumination.

In order to collect at a number of angles near to 180° from the source, the fiber pattern was focused with a lens of length 200 mm, significantly increasing the size of the fiber pattern as projected onto the phantom (as illustrated in Figure 12a) to nearly 4 mm across. In this manner, the angles formed between the source and detectors ranged from 0-10.4 degrees. Upon measuring the phantom with this setup and summing the responses of all 48 active fibers, the resulting response shown in Figure 12b is significantly different from that in Figure 9a. While two peaks separated by approximately 180° are observed, one peak (corresponding to the target passing the detector array) is significantly shorter and wider, resulting from the increased spacing of the detectors. This reasoning is confirmed in Figure 12c, in which the standard deviation of the peak position for all fibers is increased to 23.9. The wider spacing of the fibers implies that more angular information is collected. Upon performing a Nirfast reconstruction using 10 individual fibers spaced across the width of the fiber pattern (and, as a result, tenfold the number of data points as compared to a single detector at 180° from the source), the image in Figure 12d is generated. A single target is predicted with minimal 'shadowing' artifacts seen from collecting at angles smaller than 180° from the source, indicating that errors resulting from an incorrectly predicted illumination structure are reduced when source-detector angles are large and span a small range.

While it has been demonstrated that the correct number of targets (and an approximation of target position) can be recovered using this large fiber pattern setup, the validity of this technique cannot be determined unless a) the separation of two closely-spaced targets and b) the accurate determination of the positions of these targets can be demonstrated. In order to do this, three changes were made to the experiment summarized in Figures 8c and 12a: two 1/16" diameter spheres (instead of one 1/8" diameter sphere) were embedded in the phantom with close spacing (<= sphere diameter), 'fluorescence' Nirfast reconstructions were used (as to separate PTFE and Intralipid responses and normalize each to a simulated blank), and micro-CT was performed on each phantom in order to determine the exact target positions.
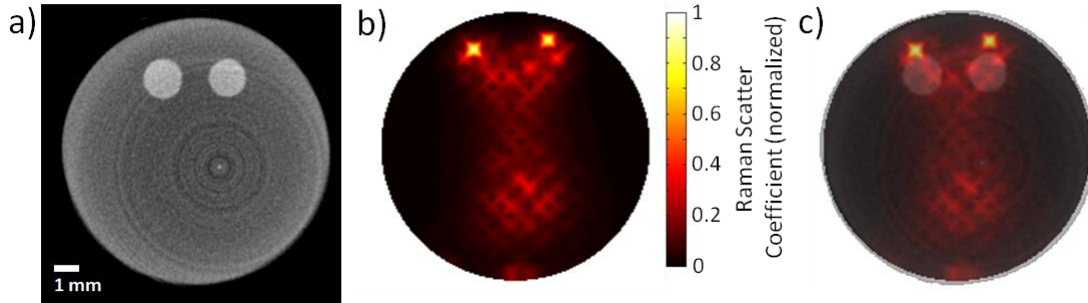

Figure 13) a) Micro-CT reconstruction of the phantom with two PTFE spheres. b) Nirfast reconstruction. c) Micro-CT and Nirfast reconstruction overlay.

Figure 13a shows the micro-CT reconstruction of a phantom with two small embedded PTFE spheres, illustrating their small separation relative to target size. Figure 13b shows the Nirfast reconstruction using data from the Raman tomography experiment. Two closely-spaced targets are predicted with some shadowing seen in the center of the reconstruction. In order to determine how accurate the positions and spacing of these predicted targets are, Figure 13c shows an overlay of the micro-CT reconstruction atop the Nirfast reconstruction. We see that the error in the position of each target is less than 1mm.
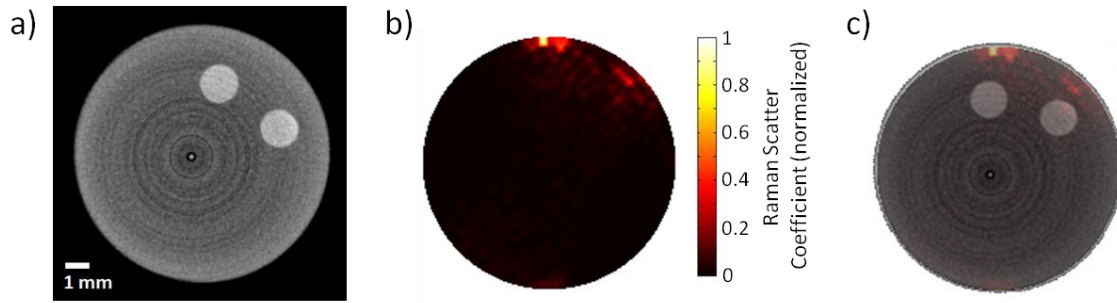
Figure 14) a) Micro-CT reconstruction of phantom with two targets and an increased (0.5%) Intralipid content. b) Nirfast reconstruction. c) Micro-CT and Nirfast reconstruction overlay.

The 0.1% Intralipid phantoms are opaque to the eye, but have only about 1/5 the scattering power of some epithelial tissues.[9] The next step towards translating this method to tissue measurements is to increase the scattering level of the phantoms fivefold to 0.5% Intralipid. The same experiment as shown in Figure 13 was performed on a phantom consisting of 0.5% Intralipid. Figure 14a shows the micro-CT reconstruction of the phantom, Figure 14b shows the Nirfast reconstruction, and Figure 14c shows the overlay of the two. It is immediately noticeable that the positions of the targets are not correct. Although the angular spacing between the targets is correctly reconstructed, their positions are 'projected' onto the edge of the phantom. While the width of these projections are similar to the widths of the PTFE spheres, the 'depths' of these targets cannot be resolved at this level of scattering using the current instrumentation and reconstruction methods.

B: Monte Carlo simulations

Thus far it has been shown that Raman tomography reconstructions with Nirfast can provide reasonable size and position information for buried spheres. As experimental parameters become more 'extreme,' such as a fivefold increase in the scattering power of the medium, reconstruction accuracy is rapidly degraded. Consideration on the improvement of reconstruction accuracy begins with an exploration of factors which limit reconstruction quality. Three general causes for poor reconstructions that will be discussed here include not acquiring enough total data (absolute undersampling), not acquiring enough unique data (spatial undersampling), and misinterpreting acquired data (incorrect modeling of system response).

Iterative image reconstruction of this sort often falls under the regime of ill-posed inverse problems, meaning that the number of unknown variables to be solved (the number of pixels in the resulting mesh) is larger than the number of known variables (data points collected). When the number of measurements performed meets or exceeds the number of pixels in the resulting mesh, a direct solution is theoretically possible. In any case, increasing the number of measurements increases the maximum potential reconstruction quality. At the same time, care must be taken to ensure that each of these measurements contributes an amount of unique or orthogonal information to the resulting data set. An increase in the absolute number of measurements cannot improve reconstruction quality if these new data points do not add new information to the resulting data set. With the end goal of determining accurate spatial distributions, the combination of source and detector sizes and positions needs to be intelligently chosen such that no region of the specimen is poorly probed or under-sampled as compared to the specimen as a whole.

These first two issues, both related to under-sampling, can be addressed to a certain degree without the use of computer modeling or an exact knowledge of the system response. The total number of measurements to acquire can be chosen based on the desired number of pixels in the reconstruction mesh (or vice-versa), whereas choosing a wide range of different source-detector configurations lends itself to probing a number of different regions of the specimen. Neither of these approaches is sufficient. Without a strong knowledge of both which regions of a specimen are probed in a given source-detector configuration and the collection efficiency of each configuration, it is not possible to determine the effectiveness of a given instrument setup. With such knowledge, an ideal instrument configuration can be determined and the maximum reconstruction quality can be predicted.

Knowledge of source-detector responses with regards to a given specimen (system-analyte response) can be determined through the computer modeling of photon fluence. This is precisely what happens during a reconstruction using Nirfast: photon fluence from each source and the spatial collection efficiency of each detector is determined through radiative transport calculations in order to quantify the sampled region of each source-detector pairing. As mentioned previously, the use of radiative transport equations in the diffusion regime requires several assumptions about both the instrument and the specimen. One such assumption is that all sources are perfect point sources and all detectors have a numerical aperture of one (equal collection efficiency over all angles, the detector equivalent of a point source). Additionally, specimens are assumed to be heavily isotropically light scattering to the point that the movement of photons is governed by the diffusion regime.

While these assumptions sufficiently describe DOT instrumentation, instruments that are simply similar to DOT will deviate from these assumptions by some amount, and this is exemplified by the instrument described in this report. The illumination is not a point source directly in contact with the specimen, but is instead a collimated beam. Detectors are also not in contact with the specimen such that each detector's response changes as a function of the angle it makes with the specimen surface. Because of the strong directionalization of the incoming light, the scattering power of the analyte, and the small distances over which measurements are taken, the diffusion approximation does not hold (as shown in Figure 11).

Significant deviations from the idealized diffusion regime have two main impacts on Raman tomography imaging and instrument design: optimal instrumentation configuration and measurement parameters cannot be determined if accurate specimen illumination and light collection cannot be modeled, and correct reconstructions cannot be obtained if reconstruction algorithms are misinterpreting the experimental data due to the inability to accurately determine the specimen region probed for each source-detector pairing. Correcting for these differences requires abandoning the diffusion regime and its required assumptions in favor of a modeling technique that allows for more accurate descriptions of instrument sources, detectors, and light-specimen interactions.

Ray tracing through an iterative Monte Carlo script represents a solution for light modeling that accommodates a full description of an instrument's sources, detectors, and specimens without operating under the previously discussed assumptions of diffusion-regime radiative transport calculations. Such a simulation models the travel of individual photons as they are generated at a source, enter a specimen, travel through the specimen, and eventually exit the specimen or become absorbed. The path traveled is a 'random walk' governed by statistical distributions determined by user-input properties of the instrument and specimen (source placement, width, and angular distribution; specimen refractive index, mean scattering length, and mean absorbance length;

detector placement, width, and numerical aperture). By simulating and recording the paths of thousands of such photons, a detailed description of how the specimen is illuminated and the distribution of collected photons is generated. The power of this approach is that it is relatively simple and straightforward to ray trace individual photons and predict their behaviors during interaction with the specimen via Beer's Law, Snell's Law, Fresnel Principle, etc. Modeling thousands of these photons does not require additional mathematics, only additional computing power. As there is no analytical solution for the radiative transport equation outside of the diffusion regime, such a photon modeling approach represents a reasonable solution to more accurate modeling of a range of instruments and specimens.

Monte Carlo approaches are not without drawbacks. Modeling a single photon is a mildly computationally intensive iterative process; modeling thousands of photons for each source and detector can increase this computational burden by several orders of magnitude. While there have been solutions in the literature to increase computational efficiency, including modeling 'big' photons which undergo multiple absorbance events[13] and the use of graphics processing units (GPUs) for code speedup,[14] at the present time Monte Carlo methods take strictly more computing power than radiative transport calculations. Additionally, simulations driven by underlying random processes do not converge on an exact solution. Just as the measurement of a signal containing white noise approaches the true value as acquisition time is increased, Monte Carlo simulations approach an ideal solution as more photons are modeled, but there will always be variability in the result. Reducing this variability to an acceptable level through increased runtimes is another consideration when employing these methods. If these computational difficulties can be handled, these methods can provide a straightforward and fully customizable means of modeling specimen illumination and performing reconstructions from experimental data.

Feature	Radiative Transport + Diffusion	Monte Carlo
Photon migration	Diffusion behavior	No diffusion assumption
Source	Point sources	Directionalized (laser) illumination
Detectors	NA of 1	NA < 1

Table 1. Comparison of the three main differences between radiative transport (Nirfast) and Monte Carlo simulations. The lack of an analytical solution to radiative transport equation outside of the diffusion regime requires that photons migration mimics diffusion and that all point sources and detectors are idealized. Monte Carlo simulations do not require these assumptions, as photons can migrate outside of the diffusion regime and sources and detectors can be modeled to have small numerical apertures.

To demonstrate some of these advantages, a Monte Carlo photon ray tracing code was written in-house with Matlab. The cylindrical specimen was represented by a circular mesh (similar to that used in the Nirfast reconstructions) comprised of 709 square pixels (as compared to ~1750 triangular elements in the Nirfast reconstructions), each with a defined mean scattering length, mean absorbance length, refractive index, etc. For the following discussion, fluence modeling was performed on a simulated homogeneous circular tissue phantom with 16 equally-spaced sources and detectors spread equally over the surface. This is often referred to as a standard 'fan' geometry in DOT literature.[1] For the Nirfast simulations, all sources were treated as point sources, all detectors

had an effective numerical aperture of one, and photon migration occurred under the assumption of the diffusion regime. These three characteristics are required for Nirfast simulations and diffusion-regime radiative transport calculations in general. In contrast, the Monte Carlo simulations utilized directionalized laser sources, small numerical aperture detectors, and a Poissonian distribution to model scattering such that diffusion behavior was not assumed. While the assumptions required by radiative transport calculations have worked well in the DOT field, the small specimen size and directionalized laser illumination utilized in these Raman tomography experiments are not well described by these assumptions. These differences are summarized in Table 1. The images from the Monte Carlo simulation shown below look significantly more 'pixelated' than their Nirfast counterparts because the data are not heavily interpolated before being presented to the user.
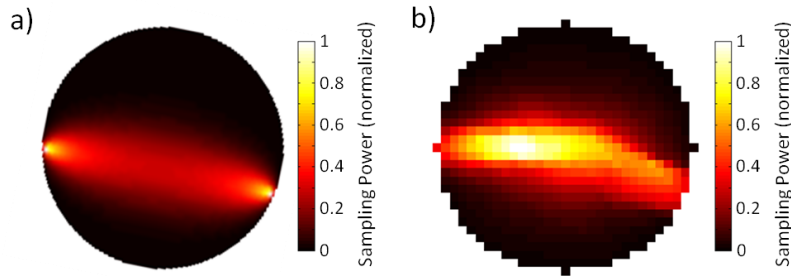

Figure 14. Simulated sampling regions of a homogeneous tissue phantom for two detectors separated by 157.5 degrees. a) Nirfast simulation with a point source, idealized detector, and diffusion-regime photon migration. b) Monte Carlo simulation modeling a directionalized laser source, a small numerical aperture detector, and non-diffusion photon migration.

Visualizing the sampling region of a single source-detector pair using the adjoint source approximation illustrates the differences between point and directionalized sources and detectors. The adjoint source approximation, employed by both Nirfast and the Monte Carlo simulation, states that if a source and a detector switch positions the detected power will remain the same as the detected photons must travel through the same region. Simulating the fluence from a source and the fluence from a detector (as though it were a source) and multiplying these two regions together shows the mutual 'sampling' region of the two. This approximation holds true as long as scattering is assumed to be isotropic or if the optical process bridging the two regions (spontaneous Raman scattering) is isotropic. Figure 14 depicts a homogeneous circular mesh with a source-detector pair at an angle of 157.5°. Using the adjoint source approximation, the effective sampling region for both a point source with a 'point' detector and a directionalized laser source with a less-than-unity numerical aperture detector are shown. The Monte Carlo simulation shows that the majority of the collected signal originates from the bulk, while in the diffusion regime the most intense signal originates from the phantom's surface. Quantitatively, the sampling power distribution of these two regions differs by approximately 23%. These differences in sampling region are more pronounced when all source-detector combinations are taken into account, representing the sampling region for
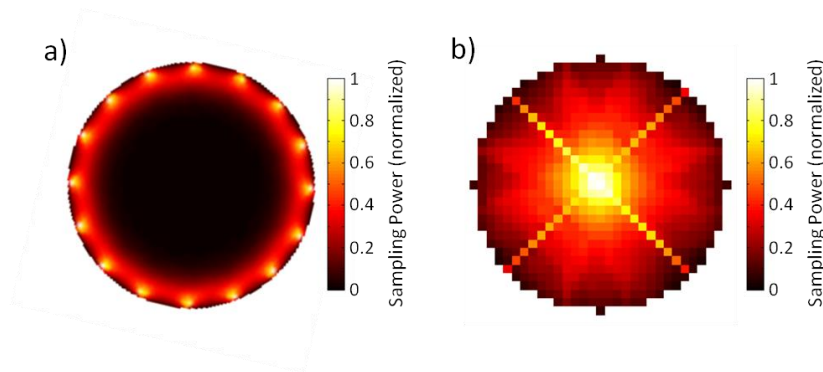
Figure 15) Simulated sampling regions from all 240 source-detector pairs for a homogeneous circular tissue phantom. A) In the diffusion regime (very high scattering, large sampling distances), the majority of the collected signal originates from near the phantom's surface. B) In a lower-scattering regime with directionalized illumination, there is a strong preference for signal originating from the bulk. An X-shaped artifact is present due to the coarse pixel mesh.

an entire experiment. The results from summing the sampling regions for all 240 source-detector combinations are shown in Figure 15. For the Monte Carlo simulation representing our Raman tomography setup, the majority of the collected signal originates from the phantom's bulk, while a diffusion regime behavior results in a collection preference for the phantom's surface. A strong preference for bulk signal agrees with previous Monte Carlo simulations regarding to transmission Raman measurements.[11]
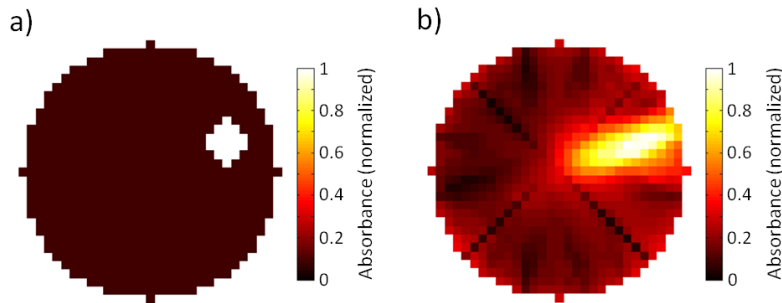

Figure 16) Monte Carlo simulations can be used for the fluence-modeling 'forward' step in an attenuation-based reconstruction. a) A homogeneous mesh with an anomalous region of absorbance that is 10x higher than the bulk. b) After five iterations, a Monte Carlo-based reconstruction algorithm can identify the region of the anomaly, albeit with artifacts.

Fluence modeling simulations through Monte Carlo methods can also be used for reconstruction purposes. Using the same mesh, a region of anomalous absorbance was added (Figure 16), simulated experimental data was generated by Monte Carlo fluence modeling, and the data was supplied to a reconstruction algorithm utilizing the same Monte Carlo method and homogeneous absorbance properties for a starting guess. It should be noted that this reconstruction type is fundamentally different from those discussed in the rest of this report, as Raman/fluorescence reconstructions investigate a photon generation process and require measured values for both the Raman signal and the fundamental frequency, while an 'absorbance' reconstruction is attenuation based and only utilizes one data point per source-detector pair. Even so, this demonstrates that Monte Carlo fluence

simulations have sufficient repeatability to be useful in reconstruction algorithms. In order to maximize this utility, processing times need to be decreased significantly through the use of graphics processing units (GPUs).

These simulation comparisons suggest that while diffuse optical tomography and Raman tomography are similar in form and function, they can differ drastically in analyte response. Radiative transport calculations have been an invaluable tool in the DOT field, as the results are highly reproducible and accurately model those experiments. Upon moving to lower scattering levels, smaller sample sizes, and the use of laser sources and small-NA detectors, the diffusion-regime radiative transport equation becomes a less accurate model. In order to develop the field of transmission Raman tomography, elegant fluence modeling simulations allowing for the accurate modeling of arbitrary sources, detectors, and sample geometries will need to be realized. Monte Carlo simulations bolstered by the processing speed of graphics processing units represent one possible means to this development.

Work aimed at Raman tomographic reconstruction is now underway using the Monte Carlo approach towards aim 2.3 for year 2 of this research.

An additional point worth adding to this report is in our collection scheme. Through the research conducted in the above experiments and through modeling we determined a fiber placed in contact with the tissue surface should provide the highest collection efficiency. The maximum collection efficiency occurs with the fiber in contact with the breast tissue. The collection efficiency of a fiber optic probe (the absolute number of photons that reach the CCD camera) increases when the fiber is in direct contact with the tissue as opposed to collection through a distance of air via a focusing lens. The two phenomena that govern this effect, Fresnel reflection and numerical aperture, are primarily functions of the refractive indices of tissue (n ~= 1.3-1.5) [15], silica glass (n ~= 1.5-1.6), and air (n = 1). The magnitude of Fresnel reflections at the boundary of two materials decreases as the difference between the materials' refractive indices (Δn) approaches zero. First, eliminating a 'layer' of air between tissue and the fiber probe reduces the number of interfaces at which reflections occur. Furthermore, the difference in refractive index for a tissue-fiber boundary (Δn ~= 0 to 0.3) is smaller than either a tissue-air boundary (Δn ~= 0.3-0.5) or an air-fiber boundary (Δn ~= 0.6). In addition, the effective numerical aperture (or collection angle) of a fiber optic or lens increases as the refractive index interfacing with the specimen increases. Just as an oil-immersion microscope objective has a larger numerical aperture than a standard objective that operates in air[16], 'immersing' the tissue in a refractive index n~=1.5-1.6 medium by directly interfacing the fiber and the tissue increases both the collection angle and the total number of photons coupled into the fiber. Therefore in our instrument's design we have included breast paddles with slots for positioning fibers so that we are able place individual fiberoptics in direct contact with the skin's surface.

KEY RESEARCH ACCOMPLISHMENTS:
- We have become familiar with clinical practices associated with breast cancer screening, breast cancer histology, how breast tissue is sampled and biopsied for diagnosis, and breast cancer pathology.
- We have built-up a comprehensive database consisting of micrographs and IR spectral images for identifying breast tissue histology and tissue chemistry. This database contains tissue cases diagnosed as hyperplasia, dysplasia, malignant carcinomas, and normal tissue.
- Using this database we have identified several locations on each biopsy to acquire Raman measurements
- We have acquired Raman measurements on all biopsy sections as well as several surgical resections.
- We have identified Raman spectral bands that can be used for distinguishing between different tissue types.
- We have used the information obtained from the point Raman measurements to achieve cell-level contrast in Raman spectral images
- We have used clinical observations and interaction with clinicians to develop a conceptual design for a Raman Tomography instrument aimed at breast cancer screening.
- We have put together autoCad files and have begun construction on the instrument
- We have evaluated existing diffuse optical tomography algorithms for Raman tomography and have adapted a Monte Carlo framework for Raman tomographic reconstruction
- We have investigated through modeling and experimentation different instrument configurations and have implemented the transmission fan style configuration into our instrument design
- We have determined that a fiber in-contact with tissue should give us the maximum collection efficiency

REPORTABLE OUTCOMES:
- A manuscript detailing high resolution IR images is included in the appendix of this report. This manuscript is indirectly a result of this work in that we were trying to obtain high resolution IR images for identifying the tissue chemistry of biopsies. This information was employed in determining regions for Raman point measurements. This manuscript has been accepted for publication in the Journal of Applied Spectroscopy.
- A manuscript detailing 'data mining' and visualization of hyperspectral data is included in the appendix of this report. This manuscript was the result of looking for spectral correlations in different tissue types and reports an approach for efficient visualization of such a data set. The manuscript is currently under review at the Journal of Transactions on Visualization and Computer Graphics.
- We are working on a manuscript reporting cell type classification through Raman spectroscopy which will detail the spectral bands correlated with the different cell types. From the year one work we have identified Raman bands such as the 1045 cm^{-1} Raman shift, the 828cm^{-1} O-P-O stretch, and the amide III bands which can be used as chemical contrast for distinguishing different cell types.
- We are working on a manuscript reporting a comparison in diffuse optical tomography reconstruction for Raman spectroscopy
- Oct. 2011- Poster Presentation 46th Midwest Regional ACS Meeting, Saint Louis MO
- Feb. 2012- Oral Presentation at the University of Michigan, Ann Arbor
- March 2012 – Poster presentation at the University of Illinois Chicago Cancer Center Forum

CONCLUSION: We have successfully completed the work described in the approved statement of work for year 1 of this research program. The results from this first year have forged a nice foundation for the work we have planned in year 2. We now have a working relationship with local clinicians and have become familiar with clinical practices associated with breast cancer screening, breast cancer histology, how breast tissue is sampled and biopsied for diagnosis, and breast cancer pathology. We have built-up a comprehensive database consisting of micrographs and IR spectral images with identified breast tissue histology and tissue chemistry. This database has tissue showing cases diagnosed as hyperplasia, dysplasia, malignant carcinomas, and normal tissue. Using this database we have identify several locations on each biopsy to acquire Raman measurements and have acquired Raman measurements on biopsy sections as well as several surgical resections. Through careful analysis we have identified Raman spectral bands that can be used for distinguishing between different tissue types and have applied those Raman spectral bands to achieve cell-level contrast in Raman spectral images. Additionally, we have used clinical observations and interaction with clinicians to develop a conceptual design for a Raman Tomography instrument aimed at breast cancer screening. From this conceptual design we put together autoCad files and have begun construction on a prototype instrument for conducting Raman tomography on breast tissue. For Raman tomographic reconstruction, we have evaluated existing diffuse optical tomography algorithms for specifically for Raman measurements and have adapted a Monte Carlo framework for our Raman tomographic reconstruction. Through modeling and experimentation we characterized different instrument configurations and have implemented the transmission fan style configuration into our prototype instrument design which uses fiber-optics in-contact with tissue to give the maximum collection efficiency. With these accomplishments we are closer to achieving prototype instrument capable of Raman tomography in breast tissue. We are excited to continue this work in year 2.

REFERENCES

1   Pogue, B. W.; McBride, T. O.; Osterberg, U. L.; Paulsen, K. D. *Optics Express.* **1999**, *4*, 270-286.

2   Flock, S. T.; Jacques, S. L.; Wilson, B. C.; Star, W. M.; Van Gemert, M. J. C. *Lasers Surg.Med.* **1992**, *12*, 510-519.

3   Mourant, J. R.; Fuselier, T.; Boyer, J.; Johnson, T. M.; Bigio, I. J. *Appl.Opt.* **1997**, *36*, 949-957.

4   Cubeddu, R.; Pifferi, A.; Taroni, P.; Torricelli, A.; Valentini, G. *Phys.Med.Biol.* **1997**, *42*, 1971-1979.

5   Collier, T.; Arifler, D.; Malpica, A.; Follen, M.; Richards-Kortum, R. *IEEE Journal on Selected Topics in Quantum Electronics.* **2003**, *9*, 307-313.

6   Durduran, T.; Choe, R.; Culver, J. P.; Zubkov, L.; Holboke, M. J.; Giammarco, J.; Chance, B.; Yodh, A. G. *Phys.Med.Biol.* **2002**, *47*, 2847-2861.

7   Gibson, A. P.; Hebden, J. C.; Arridge, S. R. *Phys.Med.Biol.* **2005**, *50*, R1-R43.

8   Siewerdsen, J. H.; Jaffray, D. A. *Med.Phys.* **2000**, *27*, 1903-1914.

9   Dehghani, H.; Eames, M. E.; Yalavarthy, P. K.; Davis, S. C.; Srinivasan, S.; Carpenter, C. M.; Pogue, B. W.; Paulsen, K. D. *Communications in Numerical Methods in Engineering.* **2009**, *25*, 711-732.

10   Everall, N.; Matousek, P.; Macleod, N.; Ronayne, K. L.; Clark, I. P. *Appl.Spectrosc.* **2010**, *64*, 52-60.

11   Everall, N.; Priestnall, I. A. N.; Dallin, P.; Andrews, J.; Lewis, I. A. N.; Davis, K.; Owen, H.; George, M. W. *Appl.Spectrosc.* **2010**, *64*, 476-484.

12   Matousek, P.; Everall, N.; Littlejohn, D.; Nordon, A.; Bloomfield, M. *Appl.Spectrosc.* **2011**, *65*, 724-733.

13   Wang, L.; Jacques, S. L.; Zheng, L. *Comput.Methods Programs Biomed.* **1995**, *47*, 131-146.

14   Alerstam, E.; Svensson, T.; Andersson-Engels, S. *J.Biomed.Opt.* **2008**, *13*

15   Parrish, J. A. *J.Invest.Dermatol.* **1981**, *77*, 45-50.

16   Hell, S.; Reiner, G.; Cremer, C.; Stelzer, E. H. K. *J.Microsc.* **1993**, *169*, 391-405.

APPENDICES:

Manuscript 1: "Designing Transfer Functions for Interactive Data Mining of Hyperspectral Images "

Manuscript 2: "High Definition Infrared Spectroscopic Imaging"

Designing Transfer Functions for Interactive Data Mining of Hyperspectral Images

Designing Transfer Functions for Interactive Data Mining of Hyperspectral Images

David Mayerich, *Member, IEEE,* Michael Walsh, Matthew Schulmerich, Rohit Bhargava

Abstract—Spectroscopy is used in several fields to acquire chemical information about a substance for identification or analysis. Recent advances allow the acquisition of hyperspectral imagery for biomedical data. This has promising implications in the fields of biotechnology and medicine, where quantitative analysis of tissue can be performed by directly measuring spatially-resolved chemical information. At present, however, these data sets require a significant amount of human intervention to identify spectral features for use in classification. We propose a method for designing transfer functions for hyperspectral images. This method allows researchers to interactively adjust parameters used to systematically change the input spectra in order to find metrics that can be used to classify features in the images.

Index Terms—microscopy, spectroscopy, transfer functions, rendering.

✦

1 INTRODUCTION

Hyperspectral data is composed of a series of measurements, taken across many wavelengths in the electromagnetic spectrum. Typically, materials exhibit a characteristic spectral signature, that is specifically indicative of their molecular composition. While the optical spectrum is commonly used for molecular studies, other forms of analysis of a wide "spectrum" of properties has led to the development of a class of techniques for molecular analysis. Some of the most common examples include (a) vibrational spectroscopy, which is used to identify chemical species based on the electromagnetic recording of oscillations of molecular bonds present in the sample, (b) mass spectrometry, which is used to identify compounds based on the mass-to-charge ratio of their constituent particles, and (c) nuclear magnetic resonance spectroscopy, which allows the characterization of nuclei based on their behavior within a magnetic field. These techniques are often used in the fields of biomedicine and forensics to determine the identity of chemical compounds. While each has its advantages and specific areas of applicability, optical techniques are most useful for label-free microscopy with micron-scale resolution and significant molecular detail. Here, we use data from these techniques as a demonstrative example for our developed methods.

Recent advances in optical detector technology allow the rapid acquisition of spectral signals that are spatially specific, producing multidimensional images

that can be extensive in size (several tens of gigabytes). These techniques have shown promise in biomedicine for cell type classification [14] and cancer analysis [21]. However, the interpretation of a spectral signature is a complex task, requiring a significant amount of pre-processing before identifying spectral features that correspond to structural and chemical information.

While the acquisition of data is relatively rapid, there are limited options at present to assist the practitioner in analyzing data. In this paper, we demonstrate techniques for designing transfer functions that allow a user to interactively explore hyperspectral images. We demonstrate these techniques on data sets imaged using vibrational spectroscopy techniques, with a particular focus on mid-infrared spectroscopic imaging, where structural and chemical information are particularly difficult to separate.

2 VIBRATIONAL SPECTROSCOPY

Vibrational spectroscopy is used to identify a chemical compound based on molecular bond vibration. Atoms that compose a molecular bond, for example the one between carbon and hydrogen (C-H), are not static but oscillate at specific frequencies. Any chemical compound and its molecular organization can be identified by determining the type and number of resonant bonds. This information can be determined by examining the interaction of electromagnetic radiation with the specimen. Two common methods for molecular spectroscopy are mid-infrared spectroscopy and Raman spectroscopy (Figure 1).

2.1 Mid-Infrared Spectroscopy

Mid-infrared spectroscopy is used to identify molecular bonds by determining the fraction of incident

- All authors are with the Beckman Institute for Advanced Science and Technology, University of Illinois at Urbana-Champaign.
- M. Walsh is also with Carle Foundation Hospital.
- R. Bhargava is also with the Departments of Bioengineering, Mechanical Science & Engineering, Electrical & Computer Engineering, and the Micro and Nanotechnology Laboratory at the University of Illinois at Urbana-Champaign, and the University of Illinois Cancer Center.
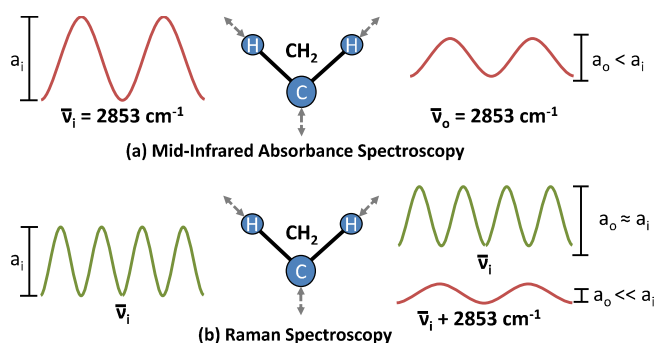
Fig. 1. Mid-infrared and Raman spectroscopy. (a) Mid-infrared spectroscopy measures the light absorbed due to resonance with specific vibrational modes in a molecule. When transmitted through a material containing a CH_2 functional group, as shown in this example, the output signal is lower intensity than the incident light when $\bar{\nu}_i = 2853 cm^{-1}$. (b) Raman spectroscopy measures the same vibrational modes by applying an input wavelength $\bar{\nu}_i$. A very small fraction of the incident light is inelastically scattered, resulting in a shift from the incident wavelength by $\pm 2853 cm^{-1}$ for CH_2.

light absorbed. Broadband mid-infrared electromagnetic radiation is transmitted through the sample and the absorbed radiation at each wavelength is quantified (Fig. 1a). The most common instrumentation for measuring absorption spectra is Fourier Transform Infrared (FT-IR) Spectroscopy [16]. In this instrumentation, and uses an interferometer is employed to encode optical frequencies in time and the recorded data are decoded using a a Fourier transform. The resulting data consist of the light transmitted as a function of frequency. By measuring the spectrum with and without a sample, hence, the absorbance of the sample can be calculated. Molecular bonds are therefore identified by finding peaks in the resulting absorbance spectrum with the frequency domain being generally recorded in units of *wavenumber* (cm^{-1}). This technique has been used extensively in forensics [3], chemistry, and biology.

Recent advances in FT-IR imaging instrumentation allow the use of focal plane arrays (FPAs) for acquiring spatially-resolved mid-infrared absorbance spectra at high speeds [23]. This allows the facile collection of hyperspectral images, where each pixel provides the corresponding spatially resolved absorption as a function of wavenumber.

2.2 Raman Spectroscopy

Raman spectroscopy provides a method for measuring the vibration of molecular bonds using monochromatic light [24]. Conventional Raman spectroscopy has applications in fields including pharmaceuticals [12], biomedicine [6], art restoration [1], and forensics

[28]. Raman spectroscopy is conventionally performed by focusing narrow-band (laser) light onto a sample. The vast majority of photons are elastically scattered, maintaining the frequency of the incident light. A small number of photons (1 in 10 million) loose energy equal to the frequency of the molecular vibrations present in the sample and therefore are a way of probing the molecules that are present (Fig. 1). Raman images are conventionally acquired using a microscope in point measurement mode. A notch filter is used to reject the incident wavelength while scattered light is dispersed onto a CCD array using a grating.

3 DATA MINING

Traditional methods for determining the chemical composition of a specimen rely on collecting a single spectrum from a homogeneous sample. This technique, known as *point spectroscopy*, was the standard in vibrational spectroscopy due to both the cost of infrared (IR) detector arrays and the large time needed to acquire Raman spectra. The increasing availability of imaging systems now permit the analyses of non-homogeneous samples, where structural changes accompany changes in chemical composition. Chemical density and sample thickness play a role in light absorption. These structural changes also result in elastic scattering, which induces wavelength-dependent changes in the measured spectra [5], [9], [10]. In addition, the extraction of chemical information from an absorption spectrum is a complex task, often requiring prior knowledge about the specimen type and possible composition [11]. In this section, we briefly describe how sample structure affects a spectrum as well as techniques for de-coupling structural and chemical information.

3.1 Refractive Index

The refractive index of a material can be expressed as the complex function

$$n(\bar{\nu}) = \eta(\bar{\nu}) + i\kappa(\bar{\nu}) \tag{1}$$

where the index of refraction n is the sum of the real component η, referred to as the phase speed, and the imaginary component κ, referred to as the extinction coefficient. Both of these components change as a function of wavelength. The real component η helps to describe the change in light direction as it crosses boundaries of different materials, and is a key component in ray-tracing algorithms that incorporate light refraction [15], [37]. Light absorption due to the resonant vibration of molecular bonds is integrated into κ. However, both of these expressions provide important information about the structure and composition of a specimen. The measurements performed using mid-infrared spectroscopic imaging provide indirect measurements of both $\kappa(\bar{\nu})$ and $\eta(\bar{\nu})$ through the measured absorbance $A(\bar{\nu})$.
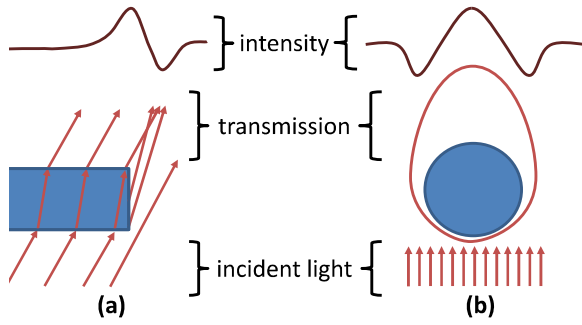
Fig. 2. Scattering of incident light through non-homogeneous samples. Two prominent contributions to scattering are (a) edge effects and (b) scattering due to morphologic features in the sample. Scattering causes spatially varying and wavelength-dependent fluctuations in transmission intensity.

These measurements are tightly coupled and must be separated in order to determine useful information about the sample. However, the separation of these components is a difficult problem that requires manual exploration of large hyperspectral images as well as some prior knowledge about the content of these images. The researcher must first separate spectral features caused by light scattering via micro-scale interactions with cells, membranes, and other edges in a biological tissue sample. These features can then be removed from the spectrum, leaving only components of absorption.

3.2 Elastic Scattering

Light that is transmitted through non-homogeneous samples is subject to scattering at boundaries between materials exhibiting different phase speeds η. These effects are prominent in mid-infrared spectroscopy, where the re-direction of light out of the collection optics of the microscope can appear as absorbance. In addition, scattering effects vary based on wavenumber due to the wavelength-dependent phase speed $\eta(\bar{\nu})$ (Sec. 3.1).

These effects are particularly prominent at edges and through structures at scales near the wavelength of the incident light (Fig. 2). The latter has been modeled using the formalism of resonant Mie scattering, which describes light scattering through a sphere. This form of scattering appears as a low-frequency oscillation in the absorbance spectrum. This oscillation is visible when imaging cells and cell nuclei. Methods have been proposed for adjusting spectra based on Mie theory [2], however these techniques are time consuming and would not provide interactive feedback. In addition, Mie theory is not generally applicable to scattering effects and the prior information required for these estimations is not always available. Finally, these models do not account for microscopy optics.

The removal of scattering effects can be accomplished through other models and is termed baseline correction. For example, a second model is more commonly used in simply subtracting a piecewise-linear function. We have found that this first-order approximation for baseline correction is effective for visualization. We allow the user to specify points where chemical absorption is assumed to be zero. We then dynamically adjust a histogram of the spectra to reflect these parameters. This allows the user to leverage prior knowledge about the chemical composition of the specimen, while providing interactive feedback that allows them to refine their selection.

3.3 Beer-Lambert Law

After contributions due to scattering are identified and removed, the remaining spectral features correspond to the absorbance A of the specimen. These features identify light absorbance due to resonant molecular vibrations in the sample as a function of wavelength. However, physical characteristics of the sample still affect the value of A in the form of tissue thickness and density. In the case of transmitted light, these relations are expressed using the Beer-Lambert law:

$$T = e^{-\kappa \ell N} \tag{2}$$

where ℓ is the path length through the specimen (thickness), N is the density of a chemical compound, and κ is the extinction coefficient. By applying this technique to absorbance spectra and specifying the extinction coefficient as a function of wavelength, the Beer-Lambert law can be represented as:

$$A(\bar{\nu}) = \kappa(\bar{\nu})\ell N \tag{3}$$

Note that there are no methods for separating the path length ℓ and density N in the general case. However, in many cases the function $\kappa(\bar{\nu})$ can be estimated using a reference band $\bar{\nu}_r$ within the spectrum. One example of a useful reference is the Amide I absorption peak often found in biological tissue samples at $\bar{\nu}_r \approx 1650 cm^{-1}$. By normalizing Amide I absorption to be uniform across chemical species ($\kappa(\bar{\nu}_r) = 1.0$), the combined contributions of path length and density can be estimated in terms of the relative protein composition using $A(\bar{\nu}_r) = \ell N$ and the extinction coefficient as:

$$\kappa(\bar{\nu}) = \frac{A(\bar{\nu})}{A(\bar{\nu}_r)} \tag{4}$$

A simple example of using a reference wavelength to separate chemical components is shown in Figure 3. While a single reference feature is useful, it is not generally applicable to most samples, therefore several references are often used for classifying multiple chemical species.
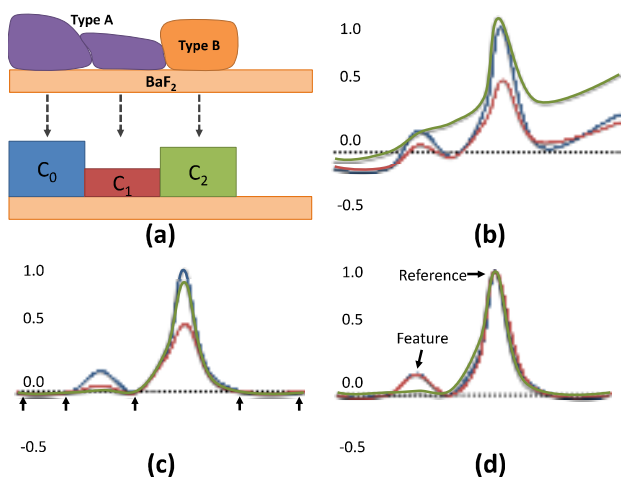
4

Fig. 3. Structure and chemical features of an absorbance spectrum. (a) A specimen is represented as a collection of two tissue types of varying density/thickness placed on a barium fluoride substrate (top) with the corresponding density (bottom). (b) The IR spectra from regions C_0, C_1, and C_2 are dominated by stattering. (c) The spectra are shown after specifying baseline points (arrows). Thickness can be determined at the reference peak. (d) Normalizing the spectra using a reference allows separation of the chemical compounds with a single feature.

4 TRANSFER FUNCTION DESIGN

Transfer functions are commonly used in volume visualization [13], [32] to assign color and opacity values to pixels based on features defined in a separate domain. These techniques have been successfully applied to large gigabyte-scale data sets [8], [31]. Creating useful transfer functions for visualizing three-dimensional scalar fields is understood to be a difficult problem. In these cases, the primary goal is to visualize particular structures in the data while minimizing occlusion from surrounding structures. The most common technique is to assign color and opacity values based on the intensity value of each pixel. However, complex volumetric data sets represented using a scalar field, such as magnetic resonance imaging (MRI) and computed tomography (CT), often contain multiple tissue types at similar intensity values. In these cases, voxel intensity is insufficient for distinguishing between tissue types. Previous work by Kniss et al. [19] demonstrate the use of spatial characteristics for building multi-dimensional transfer functions. The transfer function domain is defined using local features, such as pixel intensity, gradient magnitude, and curvature [18]. Later techniques demonstrate the use of transfer functions to visualize volumetric structures based on large-scale features, such as a scale-space representation of the image [7]. Techniques have also been developed to automate the creation of transfer functions for 3D images based on

occlusion and the spatial distribution of data [26], [33].

However, these techniques are difficult to generalize to spectroscopic images since each pixel represents a spatially-resolved absorbance function. Very few techniques currently exist for visualizing spectroscopic images. Li et al. [25] propose a technique for visualizing astrophysical data imaged at various wavelengths. They propose the use of transfer functions for defining opacity when rendering the image stack volumetrically. However, the number of bands in a single image is small and the samples are discontinuous, which limits the amount of chemical information in the data set. More recent work demonstrates a visualization framework for near-infrared spectroscopic images of historical documents sampled regularly in the spectral domain [17]. This technique allows relighting of images, interactive selection of individual bands, and metrics for evaluating similarity between user-specified spectra. However, similarity is difficult to measure for vibrational spectra because of the coupled structural and chemical contributions to the spectrum. Unsupervised techniques, such as principal component analysis (PCA) and vertex component analysis (VCA) [29], have also been proposed to perform spectral unmixing. However, these techniques assume homogeneous samples and also make specific assumptions about the data, such as the existence of orthogonal chemical signatures, which are not generally applicable.

Finally, no automated techniques have been proposed that compensate for spectral features introduced by elastic scattering, which accounts for a large amount of variance in mid-infrared spectroscopic images [22]. The methods that we propose are independent per-pixel (per-spectrum) operations that allow interactive exploration of spectroscopic images. We use two-dimensional transfer functions based on absorbance and wavelength, combined with interactive processing techniques, to identify and visualize structural and chemical information.

4.1 Metrics

We first identify useful measurements for quantifying spectral features. The user specifies parameters for these measurements in the TF domain using a simple user interface. A color map is then applied to these metric results in order to produce a transfer function.

4.1.1 Absorbance at a Wavenumber (Peak)

The absorbance at a specified wavenumber is the most basic spectral measurement and is given by $A(x, y, \bar{\nu})$, where (x, y) is the spatial position, and $\bar{\nu}$ is the wavenumber. This metric is extremely fast to compute and is useful when the chemistry associated with a spectral feature is well understood. It is also highly sensitive to peak shifts. This is particularly noticeable for the Amide I peak at 1650cm^{-1}, which is narrow
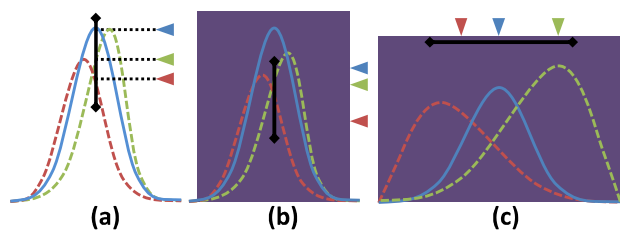
Fig. 4. Metrics for selecting spectral features. Useful measurements include (a) peak height, (b) average peak height (integral), (c) centroid (center of gravity). Colored arrows indicate the projection of the metric value on the widget (black line). Shaded regions indicate the integral intervals.

and composed of multiple chemical contributions that make it prone to shift.

Absorbance is particularly useful for detecting low-frequency components, like scattering and broad peaks, as well as detecting shifts in narrow components. However, multiple absorbance values must be used to determine the direction of a peak shift. It is also particularly sensitive to noise.

4.1.2 Area Under the Peak

While the peak absorbance in indicative of the presence of species, the total area under the peak is actually indicative of the total concentration. Hence, another useful metric is the definite integral of the spectrum on a user-specified interval $[\bar{\nu}_0, \bar{\nu}_1]$ that provides the area under the peak:

$$M_i(x, y, \bar{\nu}_0, \bar{\nu}_1) = \int_{\bar{\nu}_0}^{\bar{\nu}_1} I(x, y, \bar{\nu}) d\bar{\nu} \qquad (5)$$

This metric provides a robust measure of absorbance within a spectral region and is relatively insensitive to noise and peak shifts. This robustness makes it an ideal candidate for use as a spectral reference. It is insensitive, however, to subtle spectral changes that are often found in biological tissue samples. For color mapping (Sec. 4.3), the average peak height is used instead of the total value of the definite integral.

4.1.3 Centroid

The centroid of a bounded region of the spectrum is computed using:

$$M_c(x, y, \bar{\nu}_0, \bar{\nu}_1) = \frac{\int_{\bar{\nu}_0}^{\bar{\nu}_1} \bar{\nu} I(x, y, \bar{\nu}) d\bar{\nu}}{\int_{\bar{\nu}_0}^{\bar{\nu}_1} I(x, y, \bar{\nu}) d\bar{\nu}} \qquad (6)$$

The resulting value is the wavenumber for the center of mass in the specified region. This metric is useful for measuring shifts in single peak positions as well as the distribution of absorption among multiple neighboring peaks. This metric is dependent on the distribution of absorption and therefore does not require a reference. However, it is incapable of detecting the height or existence of peaks that do not shift as a function of spatial position.

4.2 Dynamic Processing

Our proposed TF is specified in a space defined by absorbance and wavenumber. The data set is projected into this domain and visualized using a joint histogram. The user can then select features in this domain that correspond to the structural and chemical components of the data set to be visualized. However, the data processing required to separate coupled structural and chemical features significantly affects the projection of the data into the TF domain. We implement a dynamic projection, which allows the user to explore the data set via interactive feedback in both the spatial and spectral domains, which facilitates meaningful feature selection. Our framework allows the user to interactively adjust points for baseline correction and select reference features. Data processing is performed dynamically on the GPU using CUDA [30] and provides interactive feedback for multi-gigabyte data sets. The unprocessed data set is stored on the GPU as a three-dimensional texture map represented as 32-bit floating point values. The user manipulates the data in two ways: (a) the insertion of baseline points and (b) the selection of a reference metric.

4.2.1 Histogram

The joint histogram is computed by assigning a separate block of threads per band (wavenumber). We specify a 2D block size of $\sqrt{w}$x$\sqrt{w}$ threads, where w is the maximum warp size supported by the GPU. Therefore, each block consists of one warp that executes data in a single-instruction multiple-data (SIMD) fashion. Each block is responsible for computing the complete one-dimensional histogram for a single band. The threads within each block are responsible for evaluating a spatially coherent square of pixels, initially positioned at the upper left-hand corner of the image. Each thread then iterates across the image to the lower-right corner at intervals of $\sqrt{w}$. Note that all threads within the block are part of the same (SIMD) warp, therefore they will be spatially coherent at each iteration across the spatial domain of the image.

The processed spectrum is computed dynamically as the user changes parameters for the baseline and reference. Evaluation of the processed spectrum requires (a) the current spatial coordinates and band, (b) the bands for the two neighboring baseline points, and (c) the reference value. The band is provided through the block identifier (`blockIdx.x`), while the current spatial position depends on the 2D thread identifier $[x_0, y_0] = [\texttt{threadIdx.x, threadIdx.y}]$ and iteration i, where $[x_0, y_0]$ is the initial thread position at $i = 0$. The baseline bands are stored in constant memory as a list. Determining the two neighboring baseline bands $\bar{\nu}_0$ and $\bar{\nu}_1$ requires a binary search, however this is only necessary upon block initialization and the bands are stored in a local registers for
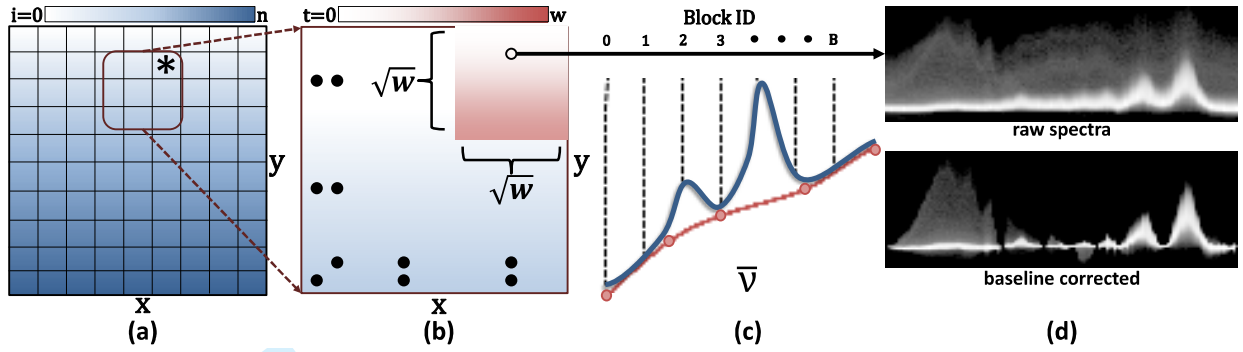
6

Fig. 5. Parallel implementation for projecting the data set into the TF space. Each band is evaluated by a block of $\sqrt{w}$x$\sqrt{w}$ threads. (a) Each block iterates across the spatial dimensions of the image from $i = 0$ to $i = n$, where $n = \frac{S_x S_y}{w}$ and S_x and S_y are the spatial extents. The threads for $i = 14$ (*) are shown. (b) The threads are evaluated using SIMD and kept spatially coherent to take advantage of 2D texture caching. (c) Each band is evaluated by an independent thread block and thread performs a maximum of 3 texture fetches per iteration (1 data point and 2 baseline points). (d) Resulting histogram.

all iterations. The spectral reference is pre-computed as a metric (described below) and stored on the GPU as a 2D image.

Computing the processed spectrum at each spatial location within a band requires a maximum of four memory fetches: (1) the raw data value at $I(x, y, \bar{\nu})$, (2) the raw values at the baseline points $I(x, y, \bar{\nu}_0)$ and $I(x, y, \bar{\nu}_1)$, and (3) the reference value $r(x, y)$. This proposed method of parallelization provides several advantages. First of all, the use of independent SIMD execution for each band allows us to compute the histogram by writing only to shared memory. The histogram is then copied to the output image in global memory upon termination of all threads in the block. By using only one warp per block, we also force all threads to perform spatially coherent memory fetches for all iterations. This allows us to take advantage of spatially coherent 2D texture caching for fetches into both the raw data I and the reference image r. This is an efficient use of GPU resources, provided that the number of bands exceeds the number of available GPU cores. This is often the case, however idle threads can be loaded for smaller data sets by subdividing the spatial domain and assigning coherent regions to different blocks. This will require performing an atomic merge to combine the resulting histograms in global memory.

Finally, note that accurate computation of the histogram requires the use of atomic adds in shared memory in order to prevent conflicts between threads in the same block. However, since the histogram is used for display purposes only, we found that the use of atomic operations was unnecessary for two reasons: (1) the histogram is displayed as an intensity map and the display device only has an 8-bit dynamic range, (2) intensity values where conflicts are likely to occur are dense, making them less noticeable (Fig. 6). Therefore, we found that atomic writes to shared
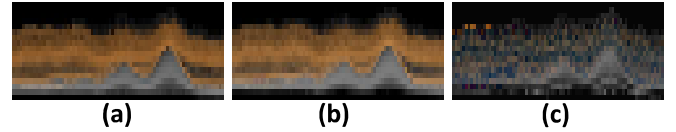

Fig. 6. Comparison of histogram rendering (a) with and (b) without atomic operations. (c) The difference image is shown (amplified by 10X). The full histogram is shown along with several selected spectra (orange).

memory provided little improvement in quality for large data sets and eliminating them gave an $\approx$4X increase in performance (Sec. 5).

4.2.2 Computing Metrics

Metrics are computed independently per pixel (per spectra), therefore spatial partitioning of the data set does not introduce the need for atomic operations. The spectra are still processed dynamically, requiring baseline points and reference bands. The data set is partitioned spatially into $\sqrt{w}$x$\sqrt{w}$ blocks, where each thread is assigned an independent spectrum. The baseline bands and reference are applied as described previously (Sec. 4.2.1). If the metric requires integration, summation occurs along the spectral axis. Note that a binary search for the neighboring baseline bands is only necessary when a thread is created. If a baseline band is crossed within an interval of integration, the new baseline bands are determined by acquiring the next band $\bar{\nu}_n$ in the list and shifting ($\bar{\nu}_0 \leftarrow \bar{\nu}_1 \leftarrow \bar{\nu}_n$). The metric result is written to an image, which is either used as a source for color-mapping to produce the final display image (Sec. 4.3) or as a reference for additional metrics.

4.3 Color Mapping

The user assigns color values to spectra based on measurements using a simple widget. Color mapping
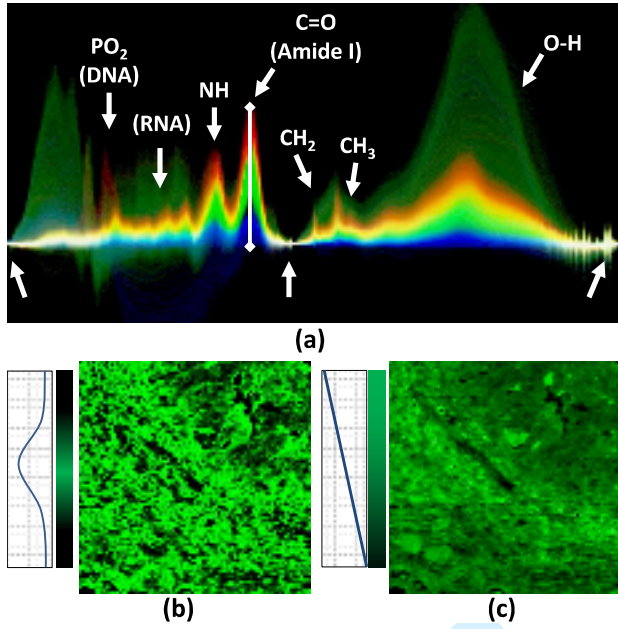
Fig. 7. Color mapping of spectral features in a baseline-corrected image. Labels indicate peaks representing prominent chemical features. (a) The spectral histogram shows three intervals of constant color (RGB) applied at the widget position at Amide I (vertical white line). Note how the colors mix as individual spectra cross and overlap with changes in density and chemistry. Spatial images show the result of a (b) Gaussian and (c) linear ramp applied to the widget.

is incorporated into the selection of metric parameters. The user places the widget at the desired metric position in the histogram. For all three metrics, the widget position is indicated by a line segment. For metrics that are computed across a specified wavenumber interval, a shaded region indicating these bounds is also displayed (Fig. 4).

When the result of a spectral measurement intersects this line segment, a color value is assigned based on the point of intersection using a ramp shader. Our framework allows the user to assign colors using a constant, linear, and Gaussian ramp (Fig. 7). In order to make selection intuitive for the integration metric M_i, color is assigned based on the average peak height:

$$\tilde{M}_i = \frac{M_i}{\bar{\nu}_1 - \bar{\nu}_0} \qquad (7)$$

This allows the widget to be placed in the vicinity of the selected spectra.

5 RESULTS

Rendering time is dominated by the dynamic computation of the histogram as the user changes processing and visualization parameters. However, the frame rate is interactive for our largest sample image (700x700x491, $\approx$1GB), requiring < 32ms for complete
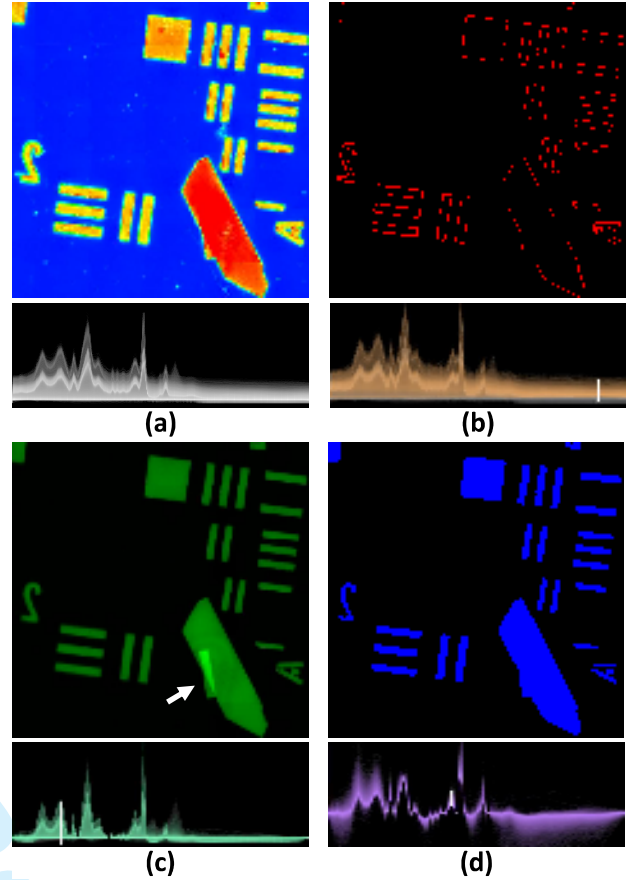

Fig. 8. Basic demonstration of the proposed processing and visualization methods on a USAF test target constructed from SU-8 photoresist on a BaF_2 substrate. (a) Magnitude of the absorbance vector and the full histogram (logarithmic intensity scaled). (b) Scattered spectra selected and displayed. (c) Baseline corrected spectra showing polymer thickness using a linear map. Note the region of dual-layered polymer (arrow). (d) Normalized spectra using the metric from (b) as a reference. Features associated with SU-8 are selected.

evaluation of the histogram (< 147ms with atomic writes to shared memory). Testing was performed on a GeForce GTX 580 with 1.5GB.

In this section, we use the proposed techniques to develop transfer functions for for both mid-infrared and Raman spectroscopic imaging data. We first demonstrate the visualization of structural and chemical components from images of well-characterized polymer targets that are often used to assess image quality. We then show how these techniques can be used to extract similar information from mid-infrared images of tissue biopsies, including the visualization of chemical components useful for breast cancer diagnosis. Finally, we show how the proposed techniques can be used on Raman images to visualize the distribution of proteins and sugars in soybean images.
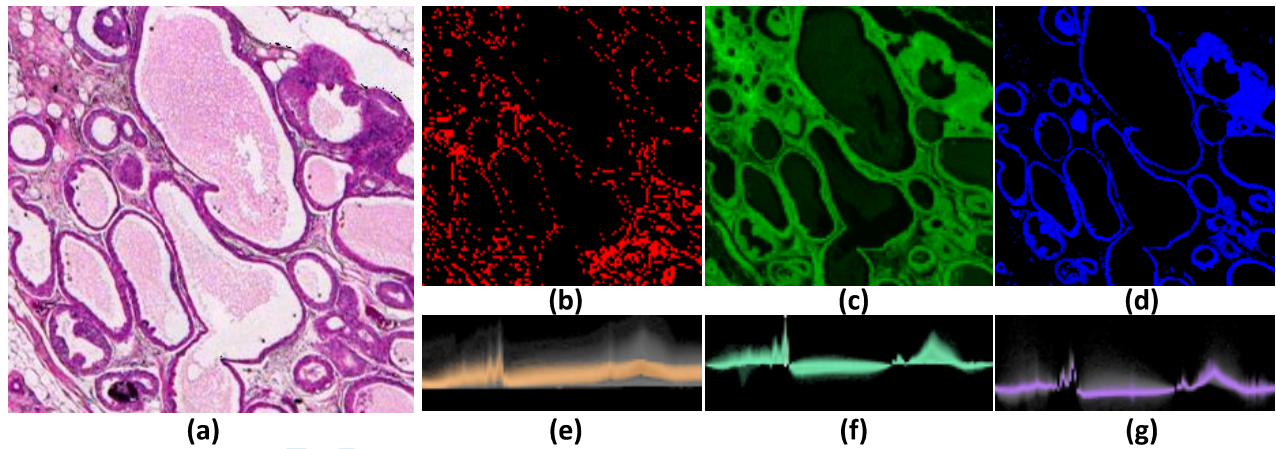
Fig. 9. Using transfer functions to visualize features seen in standard histology. A surgical resection of a breast biopsy was imaged using IR spectroscopy and then stained and imaged with a standard optical microscope. (a) A section of the hematoxylin and eosin (H&E) stained tissue sample is shown. The proposed techniques can be used to selectively visualize various structural and chemical features using only the IR hyperspectral image. (b) Scattering effects are highlighted, indicating regions containing highly scattering structures (edges and collagen fibers). (c) Removal of scattering features allows the selection of tissue thickness based on the absorbance of Amide I ($1650cm^{-1}$). (d) Using Amide I as a reference, chemical compounds corresponding to epithelial cells can then be visualized. (e-f) The corresponding joint histograms are shown, with selected pixels highlighted.

5.1 Multi-Component Air Force Target

We demonstrate the basic principles behind the proposed transfer functions using an image of a known sample. We constructed a 1951 USAF resolution test chart using an SU-8 photoresistive polymer on a barium flouride (BaF_2) substrate. The target is acquired using a commercial mid-infrared spectroscopic imaging system (Perkin-Elmer Spotlight 300) and visualized using a colormap based on vector magnitude and compared to images constructed using the proposed transfer functions (Fig. 8). We are able to cleanly extract pixels associated with edges from the raw data due to enhanced scattering in their spectra. After baseline correction, we can then estimate polymer thickness if the absorption coefficients are known or use a normalization peak to examine relative absorbance for the general case. Note that the absorbance of pixels at the edges decreases as expected, while the a double-layered region exhibits approximately twice the absorbance. We then select a reference peak at $1120cm^{-1}$ (a component of SU-8) for normalization and select another SU-8 feature in order to extract the pixels that compose the target image. All spectral histograms are shown using log-scale intensity.

5.2 Infrared Images of Tissue

Biological tissue samples pose a unique problem in spectroscopic imaging, since each pixel contains a complex combination of chemical species. Spectral features that correspond to different tissue types are subtle and difficult to identify, making interactive exploration a valuable tool. We demonstrate the use of

the proposed methods for the identification of tissue types in mid-infrared images.

We first demonstrate the structural and chemical characteristics that can be visualized using this technique. We obtain a tissue sample and place it on an IR-reflective glass substrate for imaging. The same sample is then stained using a commonly-used clinical dye, Hematoxylin and Eosin (H&E), in order to identify structural and chemical features (Figure 9a).

The proposed method is used to mine similar features from the hyperspectral image data. Since the unprocessed spectra are dominated by scattering in the high-wavenumber regions, we are able to visualize pixels containing edges and boundaries, where scattering is more prominent (Fig. 9b and e). We then select baseline points and use a linear gradient to visualize the tissue thickness and density based on Amide I absorption (Fig. 9c and f), in which over 97% of cancers of the breast arise. The facile delineation of epithelial cells is a desirable, but unmet need, as reported in recent studies using automated computerized analysis of pathologic images [4].

Finally, we demonstrate the ability to identify epithelial cells in the sample, which exhibit unique chemical characteristics. By using Amide I as a reference, features in the spectra are now dominated by chemical differences between cell types in the tissue. This allows the user to visualize the distribution of tissue types, such as epithelial cells (Fig. 9d and g).

We further demonstrate the possible use of the presented transfer functions for tissue pathology. Several breast cancer biopsies were commercially obtained and stained using H&E. Adjacent tissue samples were
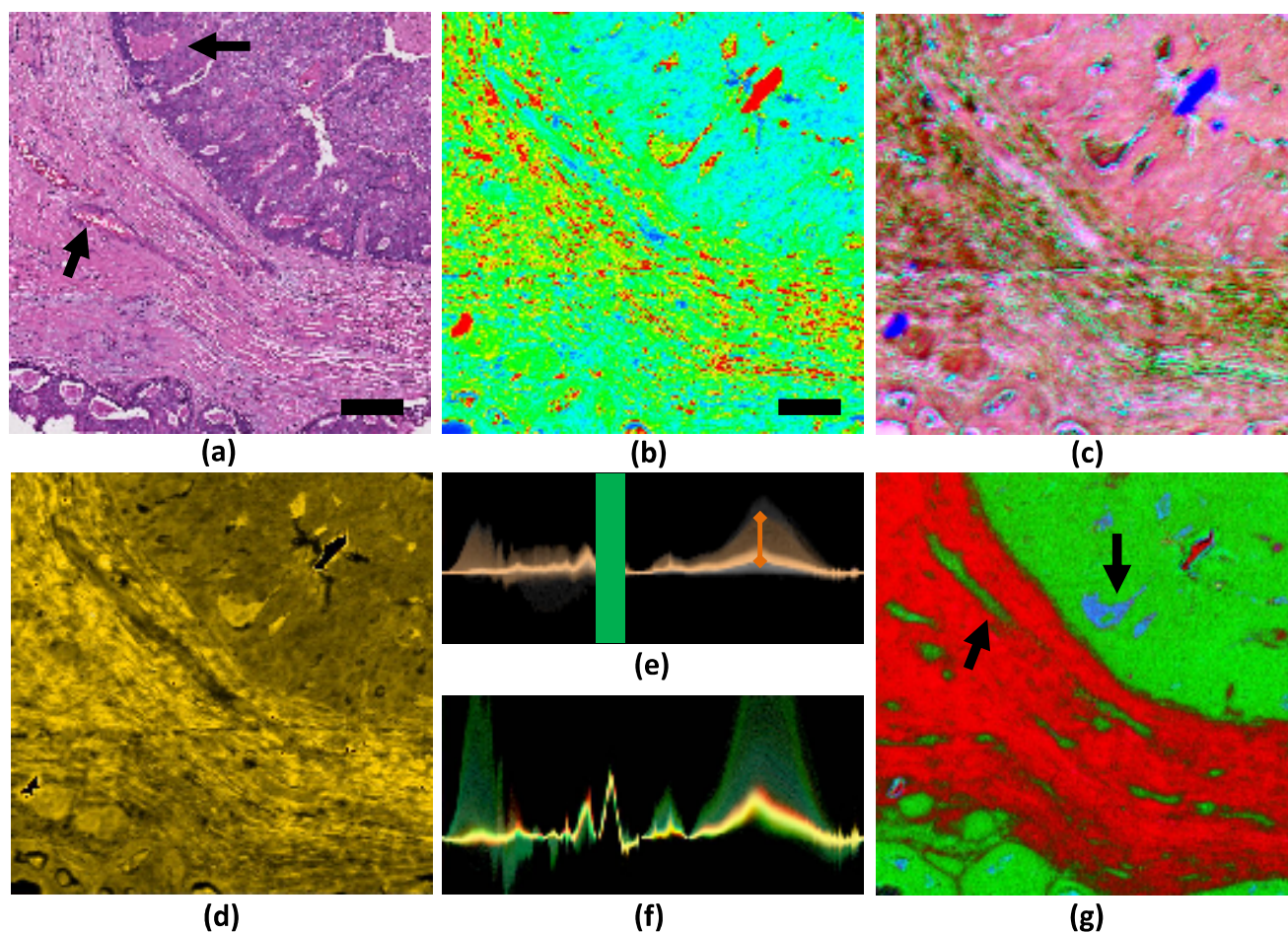
Fig. 10. Comparison of tissue visualization techniques. (a) Standard histology slide stained with H&E. Epithelial cells are purple, connective and necrotic tissue is stained pink. (b) Spectral magnitude indicated using a rainbow color map. (c) The first three principle components displayed embedded in the RGB color channels. (d) Chemical composition and density using spectral TFs, and (e) the corresponding spectral histogram. Widget position indicates the source of (d), and the shaded region is used as a reference. (f) Referenced histogram and corresponding (g) chemical visualization of the tissue sample. Features correspond to collagen (red), epithelium (green), and necrosis (blue). Arrows indicate corresponding features in the histology. Scale bar represents 100μm. The IR data set is 700x700 pixels with 490 spectral samples per pixel.

imaged using mid-infrared spectroscopy. We then design transfer functions to identify tissue characteristics that are useful for cancer diagnosis. This includes structural features, such as tissue density, as well as labeling of various tissue types. These tissue types include epithelial cells, connective tissue (stroma), and necrotic (dead and dying) cells. The spatial distribution of these features are commonly used in pathology to identify the presence of a tumor. Finally, we compare our proposed methods to those commonly used for spectroscopic image analysis, including unsupervised techniques such as PCA (Fig. 10).

The ability to identify tissue types by interactively exploring the hyperspectral data set provides several advantages over existing techniques. Unlike chemically staining the tissue to extract knowledge of constituent histology, mid-infrared imaging does not perturb the tissue sample in any way. In addition,

the effects of elastic scattering on tissue samples are not well understood, and previous methods for classification of tissue types require extensive preprocessing and the application of machine learning [14], [27]. Though an extensive comparison between the more complex machine learning methods and the method reported here must be undertaken to quantify advantages, the results seem to be comparable and significantly faster for our method by facilitating interactive analysis. In contrast, an experienced user was able to separate, visualize, and evaluate the utility of the extracted tissue characteristics useful for tumor diagnosis in a few minutes, given interactive feedback.

5.3 Raman Spectroscopy

Some advantages of Raman spectroscopy include the ability to choose the excitation frequency, easy cou-
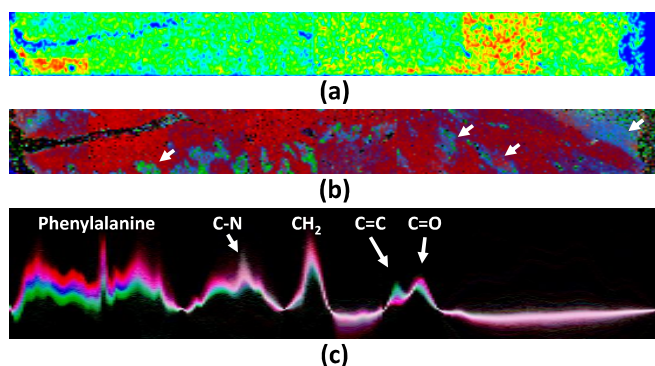
Fig. 11. Raman spectroscopy of a soybean. (a) A standard rainbow colormap of spectral magnitude. (b) Visualization showing the distribution of protein (red), carbohydrates and unsaturated fats (green) and lipids (blue). (c) The Raman histogram is shown with prominent peaks labeled.

pling to fiber-optic probes, and little to no interference by the existenc of water in a sample. These features make it useful for taking *in vivo* measurements [36], [35], [34]. However, the Raman spectral signal is extremely weak and requires long acquisition times that effectively limit the signal-to-noise ratio (SNR) and the size of image that can be obtained in a reasonable amount of time. In this section, we demonstrate that transfer functions can be created to effectively visualize the distribution of chemical compounds in Raman images. We collected spectra from a cross-section of a soybean and visualized the distribution of spectral bands correlated with sugars, proteins, and oils (Fig. 11).

6 CONCLUSIONS AND FUTURE WORK

The ability to acquire spatially resolved information using hyperspectral imaging is strongly emerging as a promising avenue across a variety of areas, especially biomedical analyses. Vibrational spectroscopy has the potential to provide quantitative histology for disease diagnosis, without the use of chemical stains in an objective and automated manner. However, computational methods must be developed to visualize the data quickly and reliably. The size and complexity of the data contained in hyperspectral images makes this a difficult problem, requiring the separation of physical and chemical characteristics from underlying spectra. In this paper, we demonstrate an interactive method for building transfer functions for visualizing hyperspectral images. Our method allows users to dynamically assimilate large collections of spectra using algorithms designed to separate structural and chemical features in real time. These features are then selected using transfer functions which allow the visualization of these characteristics in a spatial image of the sample. To our knowledge, the reported methods are the first to allow interactive processing

and visualization of hyperspectral images at this level of spectral and structural detail, and we have demonstrated their usefulness in biological samples.

Future directions include applying these techniques to three-dimensional samples, which can be acquired using Raman spectroscopy in combination with a confocal microscope. However, acquiring these images is currently extremely time consuming due to the weak signal obtained using Raman imaging methods.

Our proposed technique also has several advantages over unsupervised methods, such as PCA and VCA. In particular, the metrics that we use for visualization have finite support, requiring only a narrow band of information within the spectrum. Once useful metrics are identified, the number of collected bands can then be reduced, allowing faster imaging, for example using narrow-band filters for IR [20]. Finally, since the separation of structural and chemical characteristics from an IR image is so difficult, many algorithms for the classification of hyperspectral images rely on the use of user-defined metrics [14]. Our method may provide an efficient method for selecting features for use in more complex classifiers for IR-based clinical histology.

ACKNOWLEDGMENTS

REFERENCES

[1] T. Aguayo, E. Clavijo, F. Eisner, C. Ossa-Izquierdo, and M. M. Campos-Vallette. Raman spectroscopy in the diagnosis of the wall painting History of Concepcion, chile. *Journal of Raman Spectroscopy*.

[2] P. Bassan, A. Kohler, H. Martens, J. Lee, E. Jackson, N. Lockyer, P. Dumas, M. Brown, N. Clarke, and P. Gardner. RMieS-EMSC correction for infrared spectra of biological cells: Extension using full mie theory and GPU computing. *Journal of Biophotonics*, 3(8-9):609–620, 2010.

[3] J. P. Beauchaine, J. W. Peterman, and R. J. Rosenthal. Applications of FT-IR/microscopy in forensic analysis. *Mikrochimica Acta*, 94(1-6):133–138, Jan. 1988.

[4] A. H. Beck, A. R. Sangoi, S. Leung, R. J. Marinelli, T. O. Nielsen, M. J. van de Vijver, R. B. West, M. van de Rijn, and D. Koller. Systematic analysis of breast cancer morphology uncovers stromal features associated with survival. *Science Translational Medicine*, 3(108):108–113, Nov. 2011.

[5] R. Bhargava, S. Wang, and J. L. Koenig. FT-IR imaging of the interface in multicomponent systems using optical effects induced by differences in refractive index. *Applied Spectroscopy*, 52(3):323–328, Mar. 1998.

[6] B. Bodanese, J. Silveira, Landulfo, R. Albertini, R. A. Zngaro, and M. T. T. Pacheco. Differentiating normal and basal cell carcinoma human skin tissues in vitro using dispersive raman spectroscopy: a comparison between principal components analysis and simplified biochemical models. *Photomedicine and Laser Surgery*, 28 Suppl 1:S119–127, Aug. 2010. PMID: 20649423.

[7] C. Correa and K. Ma. Size-based transfer functions: A new volume exploration technique. *IEEE Transactions on Visualization and Computer Graphics*, 14(6):1380–1387, 2008.

[8] C. Crassin, F. Neyret, S. Lefebvre, and E. Eisemann. GigaVoxels : Ray-Guided streaming for efficient and detailed voxel rendering. In *ACM SIGGRAPH Symposium on Interactive 3D Graphics and Games (I3D)*. Feb. 2009.

[9] B. J. Davis, P. S. Carney, and R. Bhargava. Theory of mid-infrared absorption microspectroscopy I: homogeneous samples. *Analytical Chemistry*, 82(9):3474–3486, 2010.

[10] B. J. Davis, P. S. Carney, and R. Bhargava. Theory of mid-infrared absorption microspectroscopy II: heterogeneous samples. *Analytical Chemistry*, 82(9):3487–3499, 2010.

[11] B. J. Davis, P. Scott Carney, and R. Bhargava. Theory of infrared microspectroscopy for intact fibers. *Analytical Chemistry*, 83(2):525–532, 2010.

[12] T. R. M. De Beer, C. Bodson, B. Dejaegher, B. Walczak, P. Vercruysse, A. Burggraeve, A. Lemos, L. Delattre, Y. V. Heyden, J. P. Remon, C. Vervaet, and W. R. G. Baeyens. Raman spectroscopy as a process analytical technology (PAT) tool for the in-line monitoring and understanding of a powder blending process. *Journal of Pharmaceutical and Biomedical Analysis*, 48(3):772–779, Nov. 2008. PMID: 18799281.

[13] R. A. Drebin, L. Carpenter, and P. Hanrahan. Volume rendering. In *Proceedings of the 15th Annual Conference on Computer Graphics and Interactive Techniques*, volume 22, pages 65–74, 1988.

[14] D. C. Fernandez, R. Bhargava, S. M. Hewitt, and I. W. Levin. Infrared spectroscopic imaging for histopathologic recognition. *Nature Biotechnology*, 23(4):469–474, Apr. 2005.

[15] A. Glassner. *An introduction to ray tracing*. Morgan Kaufmann, 1989.

[16] P. R. Griffiths and J. A. De Haseth. *Fourier transform infrared spectrometry*. Wiley-Interscience, 2007.

[17] S. Kim, S. Zhuo, F. Deng, C. Fu, and M. Brown. Interactive visualization of hyperspectral images of historical documents. *IEEE Transactions on Visualization and Computer Graphics*, 16(6):1441–1448, 2010.

[18] G. Kindlmann, R. Whitaker, T. Tasdizen, and T. Moller. Curvature-based transfer functions for direct volume rendering: methods and applications. In *IEEE Visualization, 2003. VIS 2003*, pages 513–520. IEEE, Oct. 2003.

[19] J. Kniss, G. Kindlmann, and C. Hansen. Interactive volume rendering using multi-dimensional transfer functions and direct manipulation widgets. *Proceedings of Visualization'01*, pages 255–562, 2001.

[20] A. K. Kodali, M. Schulmerich, J. Ip, G. Yen, B. T. Cunningham, and R. Bhargava. Narrowband midinfrared reflectance filters using guided mode resonance. *Analytical Chemistry*, 82(13):5697–5706, 2010.

[21] J. T. Kwak, S. M. Hewitt, S. Sinha, and R. Bhargava. Multimodal microscopy for automated histologic analysis of prostate cancer. *BMC Cancer*, 11(1):62, Feb. 2011.

[22] J. T. Kwak, R. Reddy, S. Sinha, and R. Bhargava. Analysis of variance in spectroscopic imaging data from human tissues. *Analytical Chemistry*, 2011.

[23] E. N. Lewis, P. J. Treado, R. C. Reeder, G. M. Story, A. E. Dowrey, C. Marcott, and I. W. Levin. Fourier transform spectroscopic imaging using an infrared Focal-Plane array detector. *Analytical Chemistry*, 67(19):3377–3381, 1995.

[24] I. Lewis and H. Edwards. *Handbook of Raman spectroscopy: from the research laboratory to the process line*, volume 28. CRC, 2001.

[25] H. Li, C. Fu, and A. Hanson. Visualizing multiwavelength astrophysical data. *IEEE Transactions on Visualization and Computer Graphics*, 14(6):1555–1562, 2008.

[26] Y. Liu, C. Lisle, and J. Collins. Quick2Insight: a user-friendly framework for interactive rendering of biological image volumes. In *2011 IEEE Symposium on Biological Data Visualization (BioVis)*, pages 1–8. IEEE, Oct. 2011.

[27] X. Llor, A. Priya, and R. Bhargava. Observer-invariant histopathology using genetics-based machine learning. *Natural Computing*, 8(1):101–120, 2009.

[28] D. S. Moore and R. J. Scharff. Portable raman explosives detection. *Analytical and Bioanalytical Chemistry*, 393(6-7):1571–1578, Nov. 2008.

[29] J. Nascimento and J. Dias. Vertex component analysis: a fast algorithm to unmix hyperspectral data. *IEEE Transactions on Geoscience and Remote Sensing*, 43(4):898–910, Apr. 2005.

[30] C. Nvidia. Compute unified device architecture programming guide. *NVIDIA: Santa Clara, CA*, 83:129, 2007.

[31] H. Peng, Z. Ruan, F. Long, J. H. Simpson, and E. W. Myers. V3D enables real-time 3D visualization and quantitative analysis of large-scale biological image data sets. *Nat Biotech*, 28(4):348–353, Apr. 2010.

[32] H. Pfister, B. Lorensen, C. Bajaj, G. Kindlmann, W. Schroeder, L. S. Avila, K. M. Raghu, R. Machiraju, and J. Lee. The transfer function bake-off. *IEEE Computer Graphics and Applications*, 21(3):16–22, June 2001.

[33] M. Ruiz, A. Bardera, I. Boada, I. Viola, M. Feixas, and M. Sbert. Automatic transfer functions based on informational divergence. *IEEE Transactions on Visualization and Computer Graphics*, 17(12):1932–1941, Dec. 2011.

[34] M. V. Schulmerich, J. H. Cole, J. M. Kreider, F. Esmonde-White, K. A. Dooley, S. A. Goldstein, and M. D. Morris. Transcutaneous raman spectroscopy of murine bone in vivo. *Applied Spectroscopy*, 63(3):286–295, Mar. 2009.

[35] M. V. Schulmerich, K. A. Dooley, M. D. Morris, T. M. Vanasse, and S. A. Goldstein. Transcutaneous fiber optic raman spectroscopy of bone using annular illumination and a circular array of collection fibers. *Journal of Biomedical Optics*, 11(6):060502, 2006.

[36] M. V. Schulmerich, W. F. Finney, R. A. Fredricks, and M. D. Morris. Subsurface raman spectroscopy and mapping using a globally illuminated Non-Confocal Fiber-Optic array probe in the presence of raman photon migration. *Applied Spectroscopy*, 60(2):109–114, Feb. 2006.

[37] A. Watt and M. Watt. *Advanced animation and rendering techniques: theory and practice*. ACM press, 1992.

Dear Editor,

We are submitting our manuscript titled "Designing Transfer Functions for Interactive Data Mining of Hyperspectral Images" for consideration for publication in IEEE Transactions on Visualization and Computer Graphics.

This work describes an interactive method for exploring hyperspectral images, which are emerging in several fields including astronomy, chemistry, and biomedicine. We place a particular emphasis on immediate applications for cancer diagnosis in biomedical images.

Please note that a version of this work was accepted as a poster presentation at IEEE VisWeek 2011. We have attached the corresponding 2-page paper. All of the text and images have been updated, and the paper provides significantly more background information. We have included necessary implementation details as well as a thorough description of our technique and applications on several additional data sets.

Thank you for your consideration,

David Mayerich, Michael Walsh, Matt Schulmerich, Rohit Bhargava

Designing Transfer Functions for Exploring Hyperspectral Images

David Mayerich   Michael Walsh   Rohit Bhargava

Beckman Institute for Advanced Science and Technology, University of Illinois at Urbana-Champaign

Abstract—Spectroscopy is used in several fields to acquire chemical information about a substance for identification or analysis. Recent advances allow the acquisition of hyperspectral imagery for biomedical data. This has promising implications in the fields of biotechnology and medicine, where quantitative analysis of tissue can be performed by directly measuring spatially-resolved chemical information. However, this requires a significant amount of human intervention to identify spectral features for use in classification. We propose a method for designing transfer functions for hyperspectral images. This method allows researchers to interactively adjust parameters used to manipulate the input spectra in order to find metrics that can be used to classify features in the images.

Index Terms—biomedical imaging, medical imaging, spectroscopy, transfer functions

---◆---

1 INTRODUCTION

Hyperspectral data is composed of a series of samples, generally taken across the electromagnetic spectrum. Different compounds exhibit a characteristic signature in the spectral vector, which can be used to determine the chemical properties of a sample. This technique is often used in the fields of biomedicine and forensics to determine the identity of chemical compounds.

Recent advances in detector technology allow hyperspectral signals to be resolved spatially, producing multidimensional images with an additional spectral component. These techniques have shown promise in biomedicine where sections of tissue can be classified by cell type based on the spatially resolved spectra from a mid-infrared image [2]. However, the interpretation of a spectral signature is a complex task that currently requires human intervention to identify spectral features for use in classification. In addition, a significant amount of pre-processing must be applied before identifying spectral components that correspond to structural and chemical information. This is because chemical and structural features of the tissue are not represented as independent spectral components. Therefore, determining chemical features often requires the removal of structural properties, such as cell density and scattering characteristics.

The goal of this work is to create a tool to aid spectroscopists in selecting features for tissue classification. Current automated methods, such as principle component analysis (PCA) and vertex component analysis (VCA) [5] operate on variance and are prone to capturing noisy features, such as spectra distorted through scattering. In addition, the components produced using PCA and VCA have broad support across the entire spectrum. Since IR imaging can be time-consuming, finding localized metrics is important for clinical applications, since they allow classification with fewer spectral samples. Accurate classification methods combined with fast and non-destructive chemical imaging can play an important role in clinical research, particularly for the diagnosis of cancer biopsies.

We present a method that allows interactive exploration of hyperspectral data sets by building transfer functions similar to those used for volume rendering. We demonstrate preliminary results using biological data acquired from mid-infrared spectroscopic imaging. We first define a transfer function showing the distribution of spectra in the data set. We then allow the user to specify color values in this domain.

- *David Mayerich is with the Beckman Institute, University of Illinois at Urbana-Champaign, mayerich@illinois.edu.*
- *Michael Walsh is with the Beckman Institute, University of Illinois at Urbana-Champaign and Carle Foundation Hospital.*
- *Rohit Bhargava is with the Department of Bioengineering and the Beckman Institute, University of Illinois at Urbana-Champaign.*
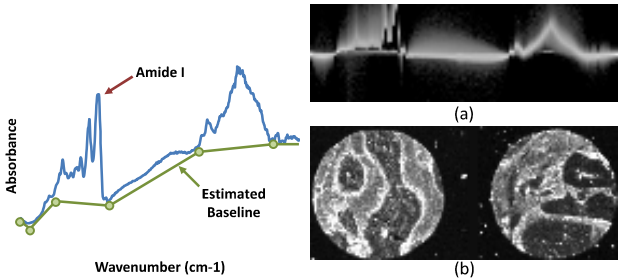
Fig. 1. Transformations applied to hyperspectral data in order to extract chemical information. (left) Baseline estimation (green) removes artifacts due to light scattering. Normalization to known peaks, such as Amide-I (red) compensates for tissue density and thickness. (a) Distribution of spectra that have been baseline corrected and normalized to Amide-I and (b) the 2D image of the Amide-I peak before normalization (after baseline correction). A threshold value is specified at the normalization wavelength in order to prevent the introduction of artifacts from division by small numbers.

This technique is similar to those published previously using spatial characteristics [4]. However, we also allow the user to dynamically adjust preprocessing parameters, thereby changing the distribution of features in the spectral domain.

1.1 Mid-Infrared Spectroscopy

Mid-infrared (IR) spectroscopic imaging is performed by measuring the amount of light absorbed by a tissue sample at wavelengths in the mid-IR region, generally between $2\mu m$ and $12\mu m$. The characteristic signature of a chemical compound is caused by the absorption of photons by molecular bonds found in organic molecules. The level of absorption at any point in the spectrum can be correlated with the existence of certain atomic bonds. These correlations can be used to identify the compound being analyzed. Other features, such as the scattering properties of the tissue sample and the cell density at a given spatial location, also affect the spectrum and may provide additional features useful for visualization.

1.2 Image Analysis

The absorbance spectrum measured at a particular spatial location in a tissue sample is affected by three major factors: (a) scattering of light through the tissue sample, (b) the tissue thickness and density, and (c) the chemical composition of the material. Scattering effects are caused by the tissue sample acting as an imperfect lens, distorting the light as it passes through the specimen. Since scattering is based on the wavelength of transmitted light, this distortion differs along the spectrum. In general, this results in a shift in the baseline and peak
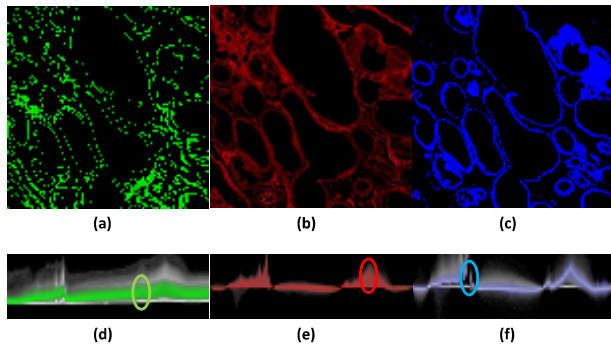
(a) (b) (c)

(d) (e) (f)

Fig. 2. Regions highlighted in a log-scale joint histogram of the spectral domain with various preprocessing steps applied. (a, d) Scattering effects allow edges to be highlighted by selecting spectra in the raw data in a region known to contain no chemical information. (b, e) After a baseline is applied, cell density is highlighted by setting a gradient along the O-H bonding region. (c, f) Normalization of the spectra to the Amide I peak allows selection of more complex chemical features, such as DNA-rich epithelial cells.

positions. While mathematical models have been proposed to compensate for scattering effects [1], they rely on an understanding of the expected output spectrum. For unknown tissue samples, a piecewise linear baseline correction is generally applied (Figure 1).

Tissue density and thickness cause scaling of the absorbance according to Beer's Law:

$$A_\lambda = b \sum_i \varepsilon_{i,\lambda} c_i \qquad (1)$$

where A is the absorbance measured at a spatial location, b is the path length (tissue thickness), c_i is the concentration of compound i and $\varepsilon_{i,\lambda}$ is the absorbance of compound i at wavenumber λ per unit of concentration [3]. Since Amide I (found at $\approx 1650 cm^{-1}$) is a protein present in most tissue samples, spectra are often normalized to the value at this wavenumber for initial analysis. However, peak height ratios are often useful metrics, therefore normalization to other peaks for exploration is important.

2 TRANSFER FUNCTION DESIGN

We display the projection of the data set into the transfer function domain using a two-dimensional joint histogram of spectral distribution as a function of spectral component λ and signal amplitude. The histogram for each slice is computed on the graphics processor using CUDA. Each value from the raw data set is transformed based on user-specified parameters for baseline correction and normalization. The projection of the data set into the transfer function domain is computed interactively, allowing the user to dynamically change preprocessing parameters and view the corresponding changes in the distribution of spectra. This allows the user to segregate chemical and structural features of the tissue into localized regions in the spectral domain. The user can then select these features, which are rendered in a two-dimensional orthographic projection of the data set in the spatial domain (Figure 2 a-c). The distribution of selected spectra are also shown as an overlay in the spectral-domain image (Figure 2 d-f).

A typical search for classification metrics involves labeling known compounds in the spatial domain. This can be done using histology slides of neighboring sections as a reference. The user then tunes the baseline and normalization criteria to find parameters that localize the selected spectra at some point in the spectral domain. The user tests this region as a metric by highlighting it using a series of widgets [4] and validating the results in the 2D spatial-domain projection.

3 RESULTS

We demonstrate preliminary results of this technique by using dynamic hyperspectral transfer functions to segment physical and chem-
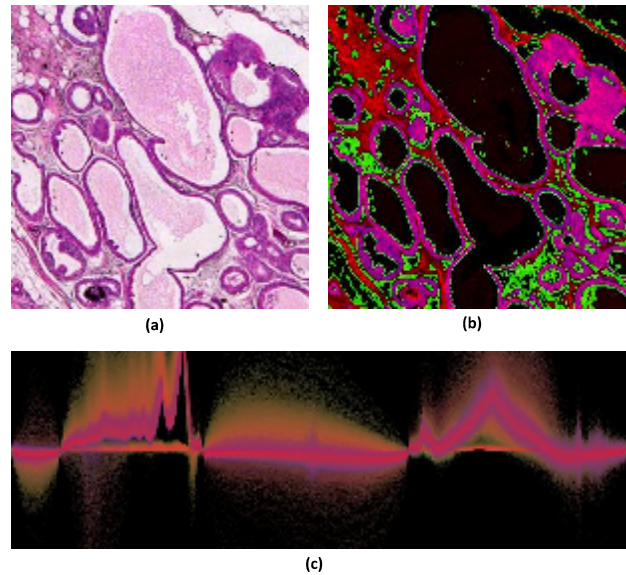

(a) (b)

(c)

Fig. 3. (a) A tissue sample imaged using IR and stained with hematoxylin and eosin (H&E) for histology. The H&E section is compared to the same region visualized with a transfer function specified using the proposed method. Tissue features such as cell density (red), edge effects (green) and epithelium (blue) are selected independently and combined into a 2D visualization (b) and in the spectral domain (c). While the selection of cell types, such as epithelium, require baseline correction and normalization, these preprocessing steps eliminate other features from the spectra as shown by the overlapping regions in the transfer function (c).

ical characteristics of data from a breast biopsy. We show edge pixels prone to scattering artifacts by selecting them from the unprocessed spectra. By applying baseline correction, we determine tissue density based on IR absorption at the Amide I band. By normalizing to Amide I, we then locate a spectral region unique to epithelial cells that line lumen in the tissue sample. The segmented cells and corresponding spectral regions are shown in Figure 2 and the final classified image and spectral overlays are shown in Figure 3. As seen in the full spectral overlay (Figure 2b), independent selection of these components would be impossible without manipulating the preprocessing parameters.

Because of the size and complexity of these data sets, the ability to interactively search multiple parameter spaces provides a much more efficient method of metric selection. For future work, we will test metrics selected using this technique against those computed using other methods, such as PCA, VCA, and purely manual selection. In addition to providing metrics localized to small regions of the spectrum, we expect that the number of required metrics can be reduced, improving classification by limiting over-fitting.

REFERENCES

[1] P. Bassan, A. Kohler, H. Martens, J. Lee, E. Jackson, N. Lockyer, P. Dumas, M. Brown, N. Clarke, and P. Gardner. RMieS-EMSC correction for infrared spectra of biological cells: Extension using full mie theory and GPU computing. *Journal of Biophotonics*, 3(8-9):609620, 2010.
[2] D. C. Fernandez, R. Bhargava, S. M. Hewitt, and I. W. Levin. Infrared spectroscopic imaging for histopathologic recognition. *Nature Biotechnology*, 23(4):469–474, Apr. 2005.
[3] P. R. Griffiths and J. A. De Haseth. *Fourier transform infrared spectrometry.* Wiley-Interscience, 2007.
[4] J. Kniss, G. Kindlmann, and C. Hansen. Interactive volume rendering using multi-dimensional transfer functions and direct manipulation widgets. *Proceedings of Visualization'01*, pages 255–562, 2001.
[5] J. Nascimento and J. Dias. Vertex component analysis: a fast algorithm to unmix hyperspectral data. *IEEE Transactions on Geoscience and Remote Sensing*, 43(4):898–910, Apr. 2005.

High-definition Infrared Spectroscopic Imaging

Rohith K. Reddy,[1,2] Michael J. Walsh,[2] Matthew V. Schulmerich,[1,2] P. Scott Carney,[2,3] and Rohit Bhargava[1,2,3,4,*]

[1]*Department of Bioengineering*

[2]*Beckman Institute for Advanced Science and Technology*

[3]*Department of Electrical and Computer Engineering*

[4]*Department of Mechanical Science and Engineering, Micro and Nanotechnology Laboratory and University of Illinois Cancer Center*

University of Illinois at Urbana-Champaign, Urbana, IL 61801, USA

[*]*Corresponding author: rxb@illinois.edu*

Abstract

Image quality from an infrared microscope has traditionally been limited by considerations of throughput and signal to noise ratio (SNR). A first principles understanding of the achievable quality as a function of instrument parameters, however, is needed for improved instrument design. Here, we first present a model for light propagation through an infrared (IR) spectroscopic imaging system based on scalar wave theory. The model analytically describes the propagation of light along the entire beam path between the source and the detector. The effect of various optical elements and the sample in the microscope is understood in terms of the accessible spatial frequencies using a Fourier optics approach and simulations are conducted to gain insights into spectroscopic image formation. The optimal pixel size at the sample plane is calculated and shown to be much smaller than that in current mid-infrared microscopy systems. A commercial imaging system is modified and experimental data are presented to demonstrate the validity of the developed model. Building on this validated theoretical foundation, an optimal sampling configuration is set up. Acquired data were of high spatial quality but, as expected, of poorer SNR. Signal processing approaches are implemented to improve the spectral SNR and resulting data demonstrate the ability to perform high-definition IR imaging in the laboratory using minimally-modified commercial instruments.

1 Introduction

Instrumentation for Fourier transform infrared (FT-IR) microspectroscopic imaging typically consists of an interferometer for multiplexed spectral encoding, microscope optics for condensing light and image formation as well as a focal plane array (FPA) detector for multichannel data recording.[1] The instrumentation has benefited from nearly 60 years of development with its genesis in point-by-point mapping,[2,3] and FT-IR microscopy developed in the 1980s.[4] The first instruments contained a single-element detector that collected all light transmitted by the microscope while apertures were used to define the spatial resolution. The use of far-field apertures to localize the region illuminated at the focal plane of the microscope implied that the smallest spot size attained was primarily determined by the wavelength of light. Most studies, however, involved larger spot sizes to achieve higher throughput and, consequently, higher signal to noise ratio (SNR) of acquired data. Two dogmatic ideas then emerged to dominate IR imaging technology. The first was that significant information could not be derived from areas smaller in dimension than the wavelength of light. While this was indeed true due to a lack of throughput for the point microscopy case, the elimination of apertures in IR imaging meant that there would still be significant throughput at smaller pixels sizes. The second misconception was that there was no benefit to increasing pixel density beyond the optical diffraction limit imposed by the wavelength as it would not result in more spatial details being accessible. Evidence to the contrary was available with the use of sub-wavelength apertures along with the higher throughput of a synchrotron source, making the approach feasible and providing excellent quality data.[5]

In other studies, there was also evidence of improved image quality by sub-pixel stepping[6] in mapping experiments that did not gain much favor on two grounds. The first objection was a practical consideration. Long acquisition time became even longer. The second objection arose due to lack of an appropriate theory, leading to a mixing of the concepts of the resolution of optical microscopy with the quality of images arising from IR absorption. Often, the two are used interchangeably, which we emphasize in this manuscript, is not the case. Though it is correct that a resolution higher than determined by the optical configuration and wavelength cannot be attained, there is also no denying the improvement in image quality by recording far-field data from areas of dimensions smaller than wavelength. For example,[7–9] aperture sizes as small as $3\mu m \times 3\mu m$ provided for excellent data using a synchrotron source at wavelengths much longer than 3 μm. Spectral quality was retained in this study while maps were sharper. More recent studies[10] have shown improved image quality by combining sub-pixel images. However, the data themselves have not been collected at the optimal pixel sizes. Coupling of an FPA to synchrotron-based

microscope systems[6,11,12] has recently provided stunning improvements in image quality.[13] Spectra of reasonable quality could be acquired in minutes by using multiple beams and the multichannel advantages of FPAs allowed for large area coverage. In these advances, the brightness of a synchrotron has been a key factor and it is unclear if the same benefits may be achievable in conventional instruments using a globar source. While there have been considerable advances in instrumentation, few theoretical analyses and validation of resolution and imaging properties have been undertaken.[14,15] These analyses, however, did not provide for a rigorous model of the IR microscope and did not examine the case of pixel sampling beyond the conventional wavelength-limited designs. The lack of an appropriate theory to optimize image quality, hence, remains as a gap in our understanding. This gap is also a barrier to design of table-top instruments of optimal quality as it is difficult, at present, to make design trade-offs in a quantitative manner.

In this manuscript, we first undertake a theoretical analysis of the image formation in IR microspectroscopic imaging. In particular, we focus on determining the best configuration for optimal image quality. We emphasize that attainable resolution and image quality, though related by wavelength and parameters of the optical setup, may not be determined by the same rules. Once the optimal image quality is determined, only then can an examination of the resolution attainable be undertaken. Hence, a detailed discussion of resolution is not undertaken here and we focus instead on criteria for obtaining images of the highest possible quality. Using the developed theory, we first determine the pixel size for highest image quality that is permitted by the optical components. While we focus here only on the capabilities of the microscope, there are other theoretical approaches dealing comprehensively with the effects of optical properties of the sample, size and shape of domains,[16] geometry of acquisition and microscopy optics on both spectral distortions[17,18] and image formation.[19] The approach here, hence, is a more general model that neglects sample detail in the interests of understanding microscope performance. Second, we implement the recommendations from theory by modifying a commercial system. Finally, we present an integration with previously described noise-reduction strategies to provide improved data quality.

2 A Model for FT-IR Spectroscopic Imaging

A theoretical analysis is presented here for the system shown in Fig. 1. Models based on ray (geometric) optics have been especially popular for IR microscopy, but are inadequate for analysis of wavelength associated effects. Full-scale electromagnetic models, at the other extreme, capture all of the physics of

image formation including polarization effects, but also involve increased complexity. It is prudent to choose the simplest model that incorporates all the phenomena of interest. Hence, we forgo the full electromagnetic treatment in favor of using the simpler scalar wave theory framework.

Our analysis is based on explicitly calculating the electric field at every plane in the microscope system. To simplify the analysis, we consider a monochromatic component of the field with a wavenumber $\bar{\nu}$ and complex amplitude U. Dependence on $\bar{\nu}$ is implied throughout unless otherwise stated. The field may be expressed as a superposition of plane waves described by functions of the form $U(\mathbf{f}) \exp\{i2\pi [\mathbf{f} \cdot \mathbf{r} + f_z(\mathbf{f})z]\}$ where $\mathbf{f}$ is a two-dimensional vector, for instance in Cartesian coordinates $\mathbf{f} = (f_x, f_y)$. The function $f_z(\mathbf{f})$ is defined so that $|\mathbf{f}|^2 + f_z^2(\mathbf{f}) = \bar{\nu}^2$, that is, the plane waves satisfy the Helmholtz equation. For each plane wave constituting the field, its relative contribution, determined by its amplitude, and its relative position, determined by its phase are both necessary for a complete description of the field. The field and all linear transformations of the field can be represented as a linear combination of these plane waves, which travel at various angles. The term "angular spectrum" is often used[20] to describe such a decomposition. We emphasize that the use of the word "spectrum" in this context should not be confused with the absorption spectrum that is commonly encountered in spectroscopy and that "spectrum" without the modifier "angular" is meant to be the usual absorption spectrum. Similarly, the term "spatial frequency" refers to the vector $\mathbf{f}$ used above and should not be confused with spectral "frequency". For the convenience of the reader, we have summarized the notation used in appendix A.2.

2.1 Optical System

The system shown in Fig. 1 can be analyzed using a modular approach. To that end, we describe each component in the optical system with an operator. This approach provides a convenient means of modifying the analysis to accommodate changes in the instrument. Since the system is linear, it is convenient to work in a notation designed for linear algebra, namely the Dirac notation.[21] Vectors describing the field in a plane at constant axial coordinate z are written $|U_z\rangle$ with Hermitian adjoint $\langle U_z|$. The two-dimensional Fourier component of the field at spatial frequency $\mathbf{f}$ is written $\tilde{U}(\mathbf{f}) = \langle \mathbf{f}|U_z\rangle$ and the value of the field at a point $\mathbf{r}$ is given by $U(\mathbf{r}) = \langle \mathbf{r}|U_z\rangle$. The sample is assumed to be thin, as described by a vector $|S\rangle$. The detector plane is taken to be at z_D. Thus the goal of the analysis is to produce an equation of the form

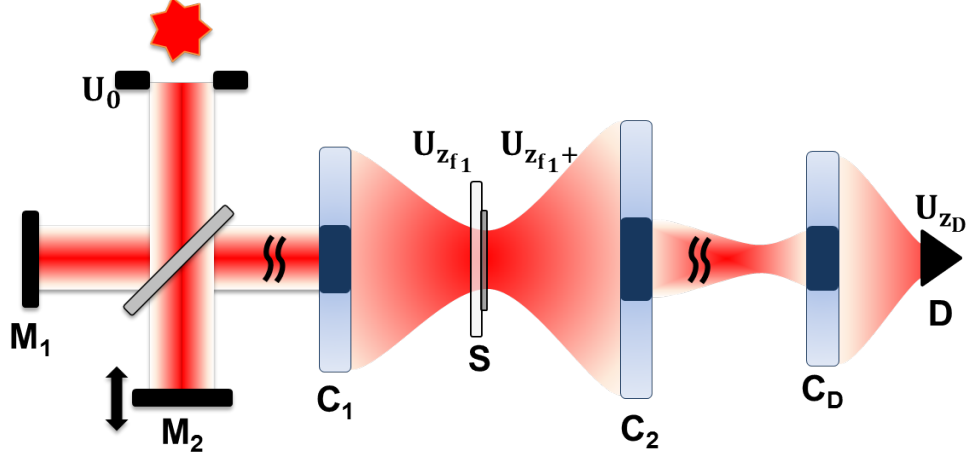$$|U_{z_D}\rangle = \mathbf{A}|S\rangle, \tag{1}$$

4

Fig. 1. Model for a FT-IR imaging system. The system consists of an interferometer coupled to a microscope system. Cassegrain C_1 focus light on to the sample S, C_2 and C_D transmit light from the sample to the detector D. The fields in different planes are also indicated.

where $\mathbf{A}$ describes the optical system.

We first address the operator for propagation through free space between two parallel planes separated by a distance d, denoted $\mathbf{K}_d$. We assume unidirectional propagation along the axis normal to the planes so that propagation is simply the accumulation of phase. The matrix elements of $\mathbf{K}_d$ are given by

$$\langle \mathbf{f}_1 | \, \mathbf{K}_d \, | \mathbf{f}_2 \rangle = \delta(\mathbf{f}_2 - \mathbf{f}_1) e^{i2\pi f_z(\mathbf{f}_1)d}, \tag{2}$$

where δ is the Dirac delta function. Alternatively, the operator may be constructed

$$\mathbf{K}_d = \int \mathrm{d}^2 f \, |\mathbf{f}\rangle \, e^{i2\pi f_z(\mathbf{f})d} \, \langle \mathbf{f}| \,. \tag{3}$$

It is useful to note that $\mathbf{K}_d \mathbf{K}_{d'} = \mathbf{K}_{d+d'}$.

An interferometer may be thought of as a beam splitter followed by propagation of two different axial distances. Given arms of length d_1 and d_2, measured from the beam splitter to each of the mirrors, the

interferometer is represented by an operator

$$\mathbf{I}_{d_1,d_2} = \frac{1}{2}\left(\mathbf{K}_{2d_1} + \mathbf{K}_{2d_2}\right). \tag{4}$$

Next we consider the effect of a Cassegrain. Much like a Fresnel lens, the Cassegrain can be considered to impart onto the field a quadratic phase factor. We represent the Cassegrain C with an operator $\mathbf{G}_C$,

$$\mathbf{G}_C = \int d^2r \, |\mathbf{r}\rangle \, Q_C(\mathbf{r}) \exp\left[-i\frac{\pi\bar{\nu}}{L_f}r^2\right] \langle\mathbf{r}| \tag{5}$$

where L_f is the focal length of the Cassegrain. The quadratic phase factor converts each plane wave incident on the Cassegrain into a spherical wave converging on its focal plane. The phase relation between plane waves incident on the Cassegrain along with the imparted quadratic phase determine the final image position and size. Q_C is the aperture function (described in detail in the appendix). It is often the case that the Cassegrain appears between two propagation steps in the form $\mathbf{K}_{d_2}\mathbf{G}_C\mathbf{K}_{d_1}$. As shown in the appendix, to a good approximation, when $d_1^{-1} + d_2^{-1} = L_f^{-1}$, the Cassegrain focuses light from the first plane into the second with a magnification factor $M_C = d_2/d_1$. Thus, it is convenient to define

$$\mathbf{H}_C = \mathbf{K}_{d_2}\mathbf{G}_C\mathbf{K}_{d_1} \approx \int d^2f \, |\mathbf{f}\rangle \, Q_C(\mathbf{f}) \, \langle -M_C\mathbf{f}|. \tag{6}$$

Clearly $\mathbf{H}_C$ is not uniquely defined unless d_1 and d_2 are specified and some care should be taken in observing the context in which it is placed. When the image plane is out-of-focus by a distance d_0, for example, the propagation operator $\mathbf{K}_{d_0}$ may be used to obtain the out-of-focus image using the operator $\mathbf{K}_{d_0+d_2}\mathbf{G}_C\mathbf{K}_{d_1} = \mathbf{K}_{d_0}\mathbf{H}_C$.

Given a field produced at the source $|U_0\rangle$, at $z = z_0$ then propagated to the interferometer at $z = z_I$, acted on by the interferometer, then propagated to the first Cassegrain, C_1, at $z = z_{C_1}$ and then from the Cassegrain to the focal plane of the Cassegrain, $z = z_{f_1}$, the resultant field is

$$\left|U_{z_{f_1}}\right\rangle = \mathbf{K}_{z_{f_1}-z_{C_1}}\mathbf{G}_{C_1}\mathbf{K}_{z_{C_1}-z_I}\mathbf{I}_{d_1,d_2}\mathbf{K}_{z_I-z_0}|U_0\rangle \tag{7}$$

The sample is modeled as a thin screen. That is, the field on the far side of the sample is assumed to be the product of the sample structure function and the field incident on the sample in the coordinate domain. We

6

formally construct an operator that effects this multiplication. Given a field $|U\rangle$, the operator $\mathbf{U}$ is defined

$$\mathbf{U} = \int \mathrm{d}^2 r \, |\mathbf{r}\rangle \langle \mathbf{r}|U\rangle \langle \mathbf{r}| = \int \mathrm{d}^2 f \, \mathrm{d}^2 f' \, |\mathbf{f}\rangle \langle \mathbf{f} - \mathbf{f}'|U\rangle \langle \mathbf{f}'| . \tag{8}$$

The sample, $|S\rangle$, then interacts with the incident field, $|U_{z_{f_1}}\rangle$, to produce a transmitted field at a plane $z = z_{f_1+}$ just past the sample

$$\left|U_{z_{f_1}+}\right\rangle = \mathbf{U}_{z_{f_1}} |S\rangle = \int \mathrm{d}^2 f \, \mathrm{d}^2 f' \, |\mathbf{f}\rangle \langle \mathbf{f} - \mathbf{f}'|U_{z_{f_1}}\rangle \langle \mathbf{f}'|S\rangle . \tag{9}$$

Substituting from Eq. 7 we find that

$$\left|U_{z_{f_1}+}\right\rangle = \int \mathrm{d}^2 f \, \mathrm{d}^2 f' \, |\mathbf{f}\rangle \langle \mathbf{f} - \mathbf{f}'| \, \mathbf{K}_{z_{f_1}-z_{C_1}} \mathbf{G}_{C_1} \mathbf{K}_{z_{C_1}-z_I} \mathbf{I}_{d_1,d_2} \mathbf{K}_{z_I-z_0} |U_0\rangle \langle \mathbf{f}'|S\rangle . \tag{10}$$

Note that $\mathbf{I}_{d_1,d_2} = \mathbf{K}_{2d_1} \mathbf{I}_{0,d_2-d_1}$. Assuming no misalignment, i.e. when the system is in focus, the propagation operators can be absorbed into the magnification factor of $\mathbf{H}_{C_1}$. Thus

$$\left|U_{z_{f_1}+}\right\rangle = \int \mathrm{d}^2 f \, \mathrm{d}^2 f' \, |\mathbf{f}\rangle \langle \mathbf{f} - \mathbf{f}'| \, \mathbf{H}_{C_1} \mathbf{I}_{0,d_2-d_1} |U_0\rangle \langle \mathbf{f}'|S\rangle \tag{11}$$

where $\mathbf{H}_{C_1} = \mathbf{K}_{z_{f_1}-z_{C_1}} \mathbf{G}_{C_1} \mathbf{K}_{z_{C_1}-z_0+2d_1}$. Evaluating Eq. 11 explicitly, we find that the field just past the sample is given by

$$\left|U_{z_{f_1}+}\right\rangle = \frac{1}{2} \int d^2 f d^2 f' \, |\mathbf{f}\rangle \, Q_{C_1}(\mathbf{f}'/M_{C_1}) \left\{1 + \exp[i2\pi f_z(\mathbf{f}')(2d_2 - 2d_1)]\right\} \langle \mathbf{f}'|U_0\rangle \langle \mathbf{f} + \mathbf{f}'/M_{C_1}|S\rangle \tag{12}$$

where it may be noted that $\langle \mathbf{f}|S\rangle$ is the Fourier component of the sample at spatial frequency $\mathbf{f}$. In the case that the source consists of a point source far from the first Cassegrain, $\langle \mathbf{f}|U_0\rangle \approx A_0$, where inclination factors of the form $1/f_z$ have been neglected. Then the field is given by

$$\left|U_{z_{f_1}+}\right\rangle = \frac{A_0}{2} \int d^2 f d^2 f' \, |\mathbf{f}\rangle \, Q_{C_1}(\mathbf{f}'/M_{C_1}) \left\{1 + \exp[i2\pi f_z(\mathbf{f}')(2d_2 - 2d_1)]\right\} \langle \mathbf{f} + \mathbf{f}'/M_{C_1}|S\rangle . \tag{13}$$

Light propagation from the Cassegrain C_1 to the sample and to the Cassegrain C_2 are illustrated in Fig. 2. The propagation of the field after the sample, $\left|U_{z_{f_1}+}\right\rangle$, to the field at the detector, $|U_{z_D}\rangle$, takes place through two more Cassegrains. The Cassegrain C_2, located effectively at $z = z_{C_2}$, focuses the sample plane to a plane $z = z_{f_2}$ such that $\frac{1}{z_{f_1}-z_{C_2}} + \frac{1}{z_{C_2}-z_{f_2}} = \frac{1}{L_{f_2}}$, where L_{f_2} is the focal length of Cassegrain C_2. Similarly, the
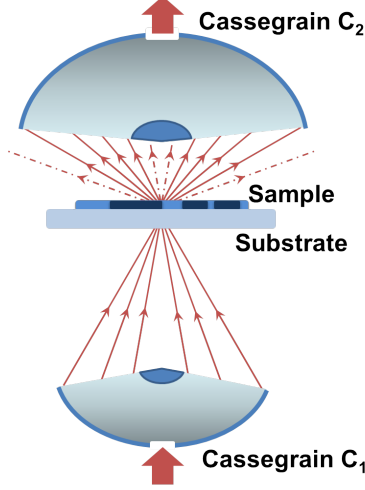
Fig. 2. Cassegrain C_1, which focuses light on to the sample, and C_2, the collection Cassegrain, are shown.

Cassegrain C_D located at $z = z_{C_D}$, focuses light from the plane $z = z_{f_D}$ onto the detector plane at $z = z_D$ such that $\frac{1}{z_{C_D} - z_{f_D}} + \frac{1}{z_D - z_{C_D}} = \frac{1}{L_{f_D}}$. Misalignment of the focal planes such that $z_{f_D} \neq z_{f_2}$ may be taken into account with the propagator $\mathbf{K}_{z_{f_D} - z_{f_2}}$. Thus

$$
\begin{aligned}
|U_{z_D}\rangle &= \mathbf{H}_{C_D}\mathbf{K}_{z_{f_D} - z_{f_2}}\mathbf{H}_{C_2}\left|U_{z_{f_1}+}\right\rangle. \\
&= \int \mathrm{d}^2 f\, \mathrm{d}^2 f'\, \mathbf{H}_{C_D}\mathbf{K}_{z_{f_D} - z_{f_2}}\mathbf{H}_{C_2}\left|\mathbf{f}\right\rangle\left\langle\mathbf{f} - \mathbf{f'}\right|\mathbf{H}_{C_1}\mathbf{I}_{0, d_2 - d_1}\left|U_0\right\rangle\left\langle\mathbf{f'}|S\right\rangle.
\end{aligned}
\tag{14}
$$

This expression is now straight-forward to evaluate. We assume that $z_{f_D} = z_{f_2}$ (the focal planes are aligned). We find explicitly that

$$
\begin{aligned}
|U_{z_D}\rangle = \frac{1}{2}\int d^2 f d^2 f' \left|\mathbf{f}\right\rangle Q_{C_D}(\mathbf{f})Q_{C_2}(-M_{C_D}\mathbf{f})Q_{C_1}(-\mathbf{f'}/M_{C_1}) \\
\times \{1 + \exp[i2\pi f_z(\mathbf{f'})(2d_2 - 2d_1)]\}\left\langle\mathbf{f'}|U_0\right\rangle\left\langle\mathbf{f'}/M_{C_1} + M_{C_2}M_{C_D}\mathbf{f}|S\right\rangle.
\end{aligned}
\tag{15}
$$

Define $M = M_{C_D}M_{C_2}$ and compute

$$
\begin{aligned}
\langle\mathbf{f}|U_{z_D}\rangle = \frac{1}{2}Q_{C_D}(\mathbf{f})Q_{C_2}(-M_{C_D}\mathbf{f})\int d^2 f' Q_{C_1}(-\mathbf{f'}/M_{C_1}) \\
\times \{1 + \exp[i2\pi f_z(\mathbf{f'})(2d_2 - 2d_1)]\}\left\langle\mathbf{f'}|U_0\right\rangle\left\langle\mathbf{f'}/M_{C_1} + M\mathbf{f}|S\right\rangle.
\end{aligned}
\tag{16}
$$

8

The above expression is true for any spatially heterogeneous sample and has no restriction on its constituent spatial frequencies. Note that M is typically larger than 1 (i.e. the detector elements are bigger than the corresponding areas on the sample).

In order to illustrate the significance of Eq. 16 consider a case where the sample is a point object. In this case $\langle \mathbf{f}'/M_{C_1} + M\mathbf{f}|S \rangle = 1$, giving

$$
\begin{aligned}
\langle \mathbf{f}|U_{z_D} \rangle &= \frac{1}{2} Q_{C_D}(\mathbf{f}) Q_{C_2}(-M_{C_D}\mathbf{f}) \int d^2 f' Q_{C_1}(-\mathbf{f}'/M_{C_1}) \\
&\quad \times \{1 + \exp[i2\pi f_z(\mathbf{f}')(2d_2 - 2d_1)]\} \langle \mathbf{f}'|U_0 \rangle \qquad (17) \\
&= \frac{1}{2} Q_{C_D}(\mathbf{f}) Q_{C_2}(-M_{C_D}\mathbf{f}) B_0. \qquad (18)
\end{aligned}
$$

Here, B_0, the integral from Eq. 17 is independent of $\mathbf{f}$. The corresponding detector intensity is

$$
\langle U_{z_D}|\mathbf{f} \rangle \langle \mathbf{f}|U_{z_D} \rangle = \frac{B_0^2}{4} [Q_{C_D}(\mathbf{f}) Q_{C_2}(-M_{C_D}\mathbf{f})] * [Q_{C_D}(\mathbf{f}) Q_{C_2}(-M_{C_D}\mathbf{f})] \qquad (19)
$$

where $*$ represents convolution.

In a case where the source is completely incoherent, i.e. $\left\langle \langle U_{z_0}|\mathbf{r}' \rangle \langle \mathbf{r}|U_{z_0} \rangle \right\rangle_e = I_0(\mathbf{r})\delta(\mathbf{r} - \mathbf{r}')$, the detector intensity is

$$
\left\langle \langle U_{z_D}|\mathbf{r} \rangle \langle \mathbf{r}|U_{z_D} \rangle \right\rangle_e = \int d^2 r I_0(\mathbf{r}')|h(\mathbf{r};\mathbf{r}')|^2 \qquad (20)
$$

where $h(\mathbf{r};\mathbf{r}')$ is the transfer function from the coherent case and $I_0(\mathbf{r})$ is the source intensity. The subscript e above denotes an ensemble average over constituent random processes. Using the equations presented in this section, we proceed to compute the spatial sampling rate and pixel size required to record all the information available from the FT-IR spectroscopic imaging system.

2.2 Pixel Size

An analysis of the equations for the FT-IR imaging system provides insight into optical design and image formation. The explicit form of Q_{C_i} in terms of NA is derived in appendix A.1 (Eqs. 29-31). It may be observed

from Eq. 16 that the spatial frequencies on the detector are always less than $\min(\bar{\nu}\mathrm{NA}_{C_2out}/M, \bar{\nu}\mathrm{NA}_{C_Dout})$ because the support of the data is the intersection of the support of $Q_{C_2}(-M_{C_D}\mathbf{f})$ and $Q_{C_D}(\mathbf{f})$. When the pre-optics to the detector are well designed, then $\bar{\nu}\mathrm{NA}_{C_2out}/M \leq \bar{\nu}\mathrm{NA}_{C_Dout}$ providing the limiting field on the detector to be a spatial frequency of $\bar{\nu}\mathrm{NA}_{C_2out}/M$. Since the detector records intensity and not fields,[20] the intensity $I(\mathbf{r}) = E^*(\mathbf{r})E(\mathbf{r})$ has a spatial frequency bound of $2 \times \bar{\nu}\mathrm{NA}_{C_2out}/M$. In order to faithfully record the entire intensity image without any loss of information, the spatial sampling rate according to Nyquist criterion[20] has to be at least twice this limiting frequency, or $4\bar{\nu}\mathrm{NA}_{C_2out}/M$. The pixel size is inversely related to the sampling rate, i.e. $L_{pixel} = M/(4\bar{\nu}\mathrm{NA}_{C_2out})$. The wavenumber, $\bar{\nu}$, in mid-infrared spectroscopic imaging typically varies between 600 cm^{-1} and 4000 cm^{-1} (0.4 μm^{-1}). Therefore, using Eq. 16, the equivalent pixel size on the sample has to be $1/(4 \times 0.4\ \mathrm{NA}_{C_2out})\ \mu m$. Thus, for a $\mathrm{NA}_{C_2out} = 0.5$, the effective pixel size on the sample is 1.25 μm and for $\mathrm{NA}_{C_2out} = 0.65$, the effective pixel size is 0.96 μm. It must be emphasized that the value of pixel size calculated above is *not* the same as resolution. It is in fact smaller than the resolution as defined by the Rayleigh criterion.[20] However, it reflects the least sampling rate required to utilize all the information passed by the system in FT-IR spectroscopic imaging.

While we have focused on image quality, a number of other insights are also apparent. In some detectors, for example, it may be advantageous to have a concave mirror instead of a Cassegrain and that can be easily be incorporated into the model by making the term corresponding to the central obscuration i.e. inner numerical aperture zero $\mathrm{NA}_{C_Din=0}^{C_Dout}$. The absence of a central obscuration increases light throughput significantly. We suggest that the Cassegrain used in commercial instruments be replaced with this mirror. This modification will result both in better image quality and lower instrument costs. Although the above derivation uses a transmission mode measurement, the same analysis can be performed for transflection mode. In the case of transflection-absorption measurement using a beam-splitter and full Cassegrain illumination, Cassegrains C_1 and C_2 correspond to the same Cassegrain and light travels through the sample twice, once before reflection and once after. However, the sampling rates and pixel sizes are the same in both cases.

3   Experiments and Simulations

Instrumentation. A Varian 7000 Spectrometer coupled to UMA-400 microscope was used to perform two sets of experiments with parameters listed in Table 1. System 1 uses accessories standard to the

Varian microscope. System 2 uses an Edmund Optics NA=0.65, 74× magnification Cassegrain for C_2. The two systems make comparisons easy since parameters other than Cassegrain C_2 are the same. The only difference is in the effective pixel size on the sample and $\text{NA}_{C_2 out}$. The interferometer is operated in the step-scan mode at a stepping rate of 200 Hz. Data were acquired at every other zero-crossing (a undersampling ratio of 2) of a He-Ne laser for a free-scanning spectral range of $7900 - 0 \ cm^{-1}$. A Fourier transform of the recorded data was carried out using the Norton-Beer medium apodization function. Data were truncated and stored as absorbance after a ratio against an appropriate background data set.

Parameter	System 1	System 2
$\text{NA}_{C_1 out}$	0.5	0.5
$\text{NA}_{C_2 out}$	0.5	0.65
$\text{NA}_{C_D out}$	0.5	0.5
M_{C_1}	15×	15×
M_{C_2}	15×	74×
M_{C_D}	3×	3×
Pixel Size (effective)	$5.5\mu m$	$1.115\mu m$
Spectral Resolution	$8cm^{-1}$	$8cm^{-1}$
# Scans per pixel	8	128
# Scans (Background)	128	128
Detector size	128×128	128×128
Undersampling ratio	2	2

Table 1. Experimental Parameters used for data acquisition and modeling.

Data extraction and image processing were performed using a hyper-spectral imaging software package, ENvironment for Visualizing Images (ENVI). In ENVI, the two dimensional Fourier transform routines are in built. Modules for further data processing were written in-house with the use of IDL 7.1 and Matlab 7. The two imaging systems, with parameters shown in table 1 (parameters 1-6) are simulated. The simulations were performed on a quad core computer with a Nvidia GeForce GTX 580 GPU and 12GB RAM. Modules and functions for the simulations were written in house using Matlab 7. The simulations compute the detector field and intensity for incoherent illumination using the system parameters (table 1, parameters 1-6) and object as inputs. The run time for simulations is about $23s$ for each wavenumber.

Prostate and breast tissue microarrays (TMAs) were used as a platform for high throughput sampling.[22] TMAs consist of a large number of small ($\cong 1mm$ diameter) tissue sections arranged in a grid

pattern on an substrate. This technique facilitates and streamlines acquisition of data from several patients and provides diversity to the sample population under observation. Breast and prostate tissue microarrays were obtained from the University of Illinois Chicago (kindly provided by Dr Andre Kajdacsy-Balla) and from Biomax (No. BR1003; US Biomax, Rockville, MD). One 5 μm thick tissue section from each array was placed on a BaF_2 substrate for IR imaging and serial 5 μm thick sections were placed on standard glass slides for hematoxylin and eosin ($H\&E$) staining. IR imaging data were acquired from a normal breast tissue core that contained a region comprising of terminal ductal lobular units as well as from a normal prostate tissue core from the region of a small blood vessel.

4   Results and Discussions

Our first step in analyzing the performance of the imaging systems was to validate simulations with recorded data using a gold standard for comparison. As common in other forms of microscopy, a standard USAF 1951 target, consisting of chrome on glass, was chosen. The chrome provides a large attenuation (absorbance) with negligible thickness. It also provides high contrast for visible-microscope imaging. Hence, it is an ideal sample for simulation and validation. We first recorded visible-light images for a standard USAF microscope target (Edmund optics). The recorded image was binarized to remove any edge blurring or grayscale values in the simulation. An absorbance of unity was assigned to the chrome region and the resulting image was used for simulation. Regions without the chrome were assigned a transmittance of unity (zero absorbance). Simulations were carried out for both the instrument configurations described previously. The light source is assumed to be spatially incoherent as in Eq. 20. Spectroscopic imaging data were also recorded using the target. We analyzed group number 6 and 7, elements 1 through 6, as these represent the highest image quality typically encountered in IR microscopy. Images of the standard sample employed for simulation, absorbance images from simulated data and absorbance images from the recorded data corresponding to the two instrument configurations are shown in Fig. 3. In order to facilitate comparison of simulations, we have used the same pixel size for both optical configurations, although different NA lenses are often associated with different magnifications. The chosen pixel size for simulations of 0.36 μm will not be a limiting factor in the resulting image quality. The USAF target is designed to enable facile calculation of the frequency response of the imaging systems as well as to illustrate

resolution capabilities via images. In simulations, we emphasize again that the sample is assumed to be infinitesimally thin to avoid effects associated with thickness. Comparing the two simulated absorbance images (Fig. 3(b) and (f)) with the same pixel size shows the effects of increasing NA. As expected, an increase in the NA provides for higher quality and higher resolution images. Nevertheless, the enhancement is not especially striking. A more obvious degradation in image quality is evident when the pixel size is increased from 1.1 μm (Fig. 3(f)) to 5.5 μm (Fig. 3(g)) while all other parameters are held constant. This dramatic change in image quality emphasizes the need for carefully choosing the pixel size. The combined effects of choosing a higher NA lens and the appropriate sampling (small pixel size) can result in significantly improved image quality (cf. Fig. 3(b) and Fig. 3(g)). To experimentally validate these predicted improvements in image quality, we set up two optical configurations described in table 1 on the same commercial microscope and obtained data on the same USAF 1951 target used in simulations. Our goal was to minimally modify (by changing one lens) the existing commercial system. Hence, we did not alter the condenser. Matching the throughput via the image formation lens and condenser is likely to result in better SNR but will not materially change the appearance of the images as the image quality depends only on the angular spectral bandwidth of the image formation lens. Experimental results for (c) NA=0.65, pixel size = 1.115 μm and (h) NA=0.50, pixel size = 5.5 μm are presented for comparison. A dramatic improvement in image quality is observed experimentally for the smaller pixel size. Expanding a smaller region for comparison in Figs. 3(d),(e) and 3(i),(j), the three smaller bars are distinguishable only in the higher NA, smaller pixel size setup. This qualitatively demonstrates the gain in image quality and resolution using a higher NA system along with the appropriate pixel spacing. In all cases, as expected, we also note that the recorded data are of somewhat lower quality than the simulations. This is due to edge effects in the sample, finite detector sizes, imperfect optics and experimental noise in the recorded data.

While the images from simulation and recorded data agree well, they do not provide a quantitative understanding of the performance improvement and limits of the two configurations. Therefore, we quantitatively analyzed the performance of the systems as a function of the spatial frequency. The frequency response of the optical system is often characterized by the modulation or contrast transfer function of the system. While optical systems typically employ intensity values to examine the imaging system performance, here we use the spatial frequencies in Fig. 3(a) and the corresponding absorbance values from simulations and recorded data to plot the absorbance contrast. The absorption contrast ratio (ACR) is defined as the difference in maximum and minimum absorbance observed at a specific spatial frequency
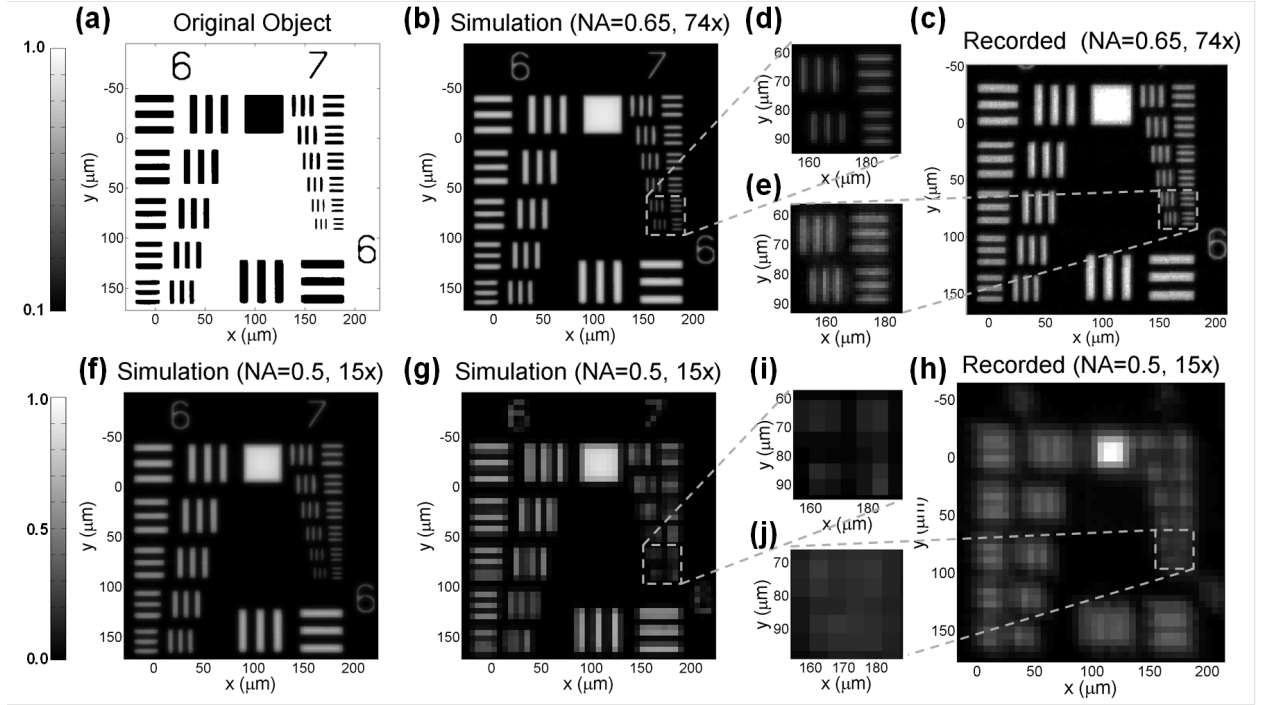
Fig. 3. (a) The original object consists of a set of bars of different sizes with transmittance indicated to the left. Absorbance images from simulations at $\bar{\nu} = 3950\ cm^{-1}$ are shown when Cassegrain C_2 has (b) NA=0.65, (f) NA=0.50, (g) NA=0.50. The pixel size in (b) and (f) are 1.1 μm where as the pixel size in (g) is 5.5 μm. Experimental absorbance images from $\bar{\nu} = 3950\ cm^{-1}$ are shown with configurations (c) NA=0.65, Pixel size = 1.1 μm (h) NA=0.50, Pixel Size = 5.5 μm. (d), (e), (i) and (j) show magnified regions from corresponding images.

14

compared to that observed in the ideal case. The ideal difference between high and low absorbance is obtained by comparing absorbance values from regions on the sample with no absorbance (for example, the region used to collect a background spectrum) and a relatively homogeneous region of high absorbance (for example, on the large square in a USAF 1951 target). Figure 4(a) shows a plot of the absorbance contrast ratio as a function of spatial frequency at 3950 cm^{-1}. As expected, ACR is highest at low spatial frequencies and decreases with increasing spatial frequency until zero (no measurable contrast). ACR for the lower NA system reaches zero at a lower spatial frequency than that for the high NA one as is evident from the polynomial fit (solid lines) to simulation data. It may be seen in the experimental data that the high NA system resolves all bars including the smallest bars (Group #7) available on the USAF 1951 target. The frequency at which ACR reaches zero can be predicted via simulations to be about 0.4 μm^{-1} ($\cong$400 line pairs/mm). Contrast decreases with reduction in pixel size since light intensity per pixel reduces. As a result, the increased imaging capability is partially offset by a decreased spectral SNR in the resulting absorbance images. While predictions from simulations agree well with measured ACR for the high NA system, there is some disagreement for the lower NA setup at high spatial frequencies. This difference is observed at approximately 0.08 μm^{-1} ($\cong$80 line pairs/mm). Experimentally, the lower NA system cannot resolve bars beyond a spatial frequency of 0.115 μm^{-1} ($\cong$115 line pairs/mm). This is lower than the theoretically predicted 0.15 μm^{-1} ($\cong$150 line pairs/mm). This can be attributed to the finite pixel size preventing an accurate recording of the data. This comparison between ACR of the high and low NA systems, enabled by the developed theoretical understanding, provides convincing proof that the designs of present-day instrumentation are not permitting optics-limited performance and can be rapidly and easily reconfigured to provide significantly higher imaging performance.

Though the previous analysis provides the smallest observable features, the relationship of these features to the optimal pixel size needs to be quantified. We examine the pixel size at the sample plane required for optimally sampling the signal as a function of NA and wavelength (Fig. 4(b)). While the optimal pixel size can also be calculated analytically, this plot provides the design parameters for instruments should a practitioner develop an instrument for high performance at any specific wavelength while using a specific lens. As expected, the recommended pixel size decreases with decreasing design wavelength. The dependence on NA is rather striking as well. It is noteworthy that most commercially available systems provide reasonably high NA, but the pixel size is not commensurate with the optical components. Thus,
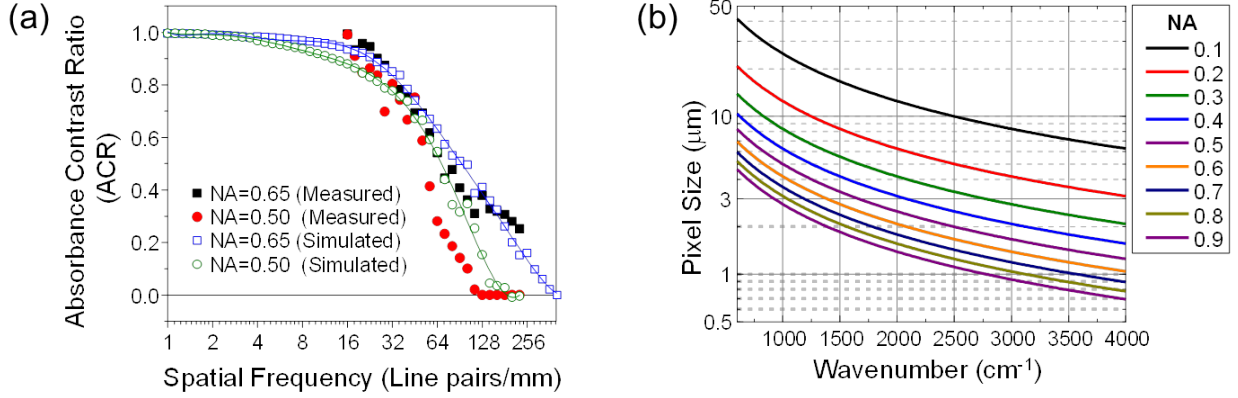
Fig. 4. (a) A plot of absorbance contrast ratio (ACR) measured from both simulation and recorded experimental data as a function of spatial frequency at $\bar{\nu} = 3950$ cm^{-1} for the two systems in table 1. (b) A plot of minimum pixel size required for correctly sampling allowable spatial frequencies as a function of $\bar{\nu}$ and NA is shown. The pixel size corresponds to the effective pixel size at the sample.

an improvement in incorporating a higher NA lens is not likely to be as dramatic as using the optimal pixel size in current commercial systems. We note that this plot is based on the maximum attainable spatial frequencies for thin objects and larger sample thicknesses are likely to achieve poorer contrast for the limiting spatial frequency.

The pixel sizes recommended will provide the highest image quality provided by the microscope, unless limited by the sample. The optimal pixel size and the resolution of an imaging system are also related. According to the Rayleigh criterion, for example, the attainable resolution is $0.61/(\bar{\nu}NA)$. We propose to sample at $0.25/(\bar{\nu}NA)$ in order to convert the analog signal into a digital readout without information loss. We note that the pixel size proposed is significantly smaller than the resolution. This result is contrary to prevailing wisdom in that it is widely believed that no further improvement is possible once a pixel size equal to the resolution has been attained. Indeed, mixing the concepts of resolution and pixel sizes for correct signal sampling has led to significant confusion in IR microscopy. We emphasize that our suggestions for improved data quality are not a contravention of the resolution criterion. Consider the case of pixel spacing resulting in optimal resolution. To resolve two objects, we need more than two measurements when the data are digitized. For example, consider two point objects that are centered on a pixel each. To entirely resolve these objects, appropriate sampling implies that there be a pixel on either side of the object to separate
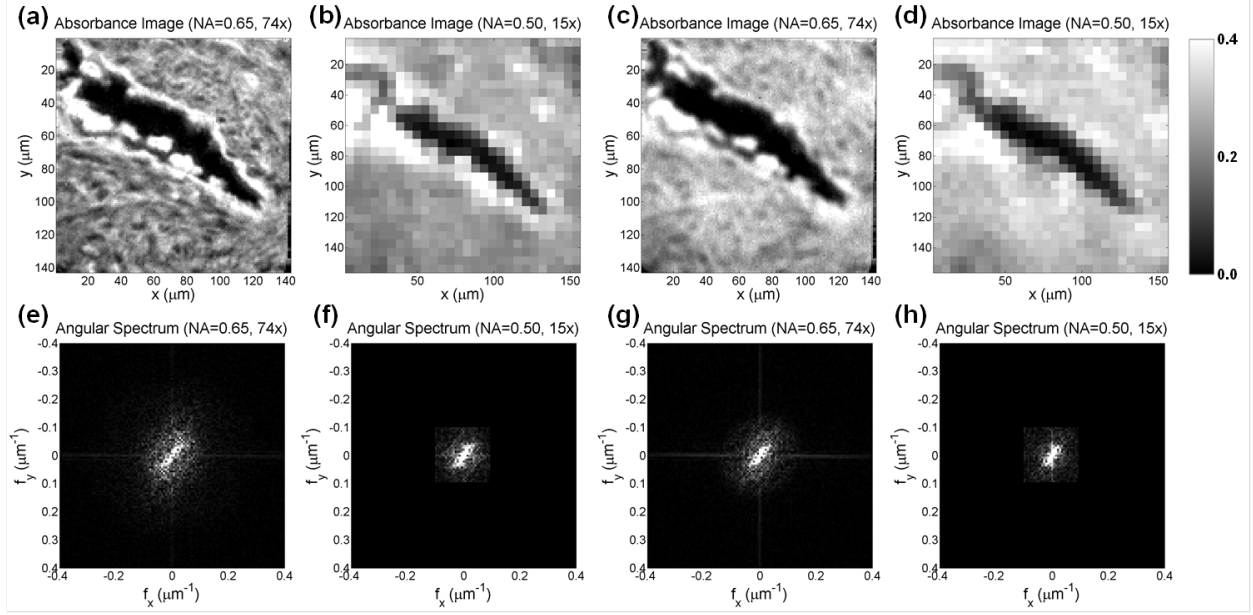
16

Fig. 5. Absorbance images from spectroscopic imaging data obtained from the two configurations (NA=0.65, NA=0.50) are shown on top. The corresponding angular spectra are shown at the bottom. Images for the system with (a) NA=0.65 and (b) NA=0.50 obtained by plotting the absorbance at $\bar{\nu} = 2962 \ cm^{-1}$. Similarly, the absorbance at $\bar{\nu} = 1650 \ cm^{-1}$ is shown for systems with (c) NA=0.65 data and (d) NA=0.50.

them from each other and any other neighboring objects. Therefore, at least 5 pixels are needed to resolve two point objects. A more formal discussion of sampling for optical microscopy[6] and its extension to IR microscopy is provided elsewhere using this signal processing approach. Our approach is distinct from these methods and incorporates light transmission though an entire imaging system and provides calculations based on absorbance. We note that the resolution of an instrument cannot be correctly evaluated unless the pixel size is appropriate (smaller). Even if two objects cannot be resolved into their appropriate shapes using smaller pixels, the detail in higher pixel density images is higher. Two point objects, for example, will appear as dumbbells or ovals. Hence, even for systems or wavelengths in which the pixel size is smaller than required for correctly sampling the spatial frequencies permitted by the optics, an improvement in image quality may be observed. For a detailed discussion, we refer the reader to appendix A.3.

Data from the two optical configurations described in table 1 are shown in Fig. 5. Data are recorded on prostate tissue that is prepared using methods previously reported[23–25] and images are obtained using the
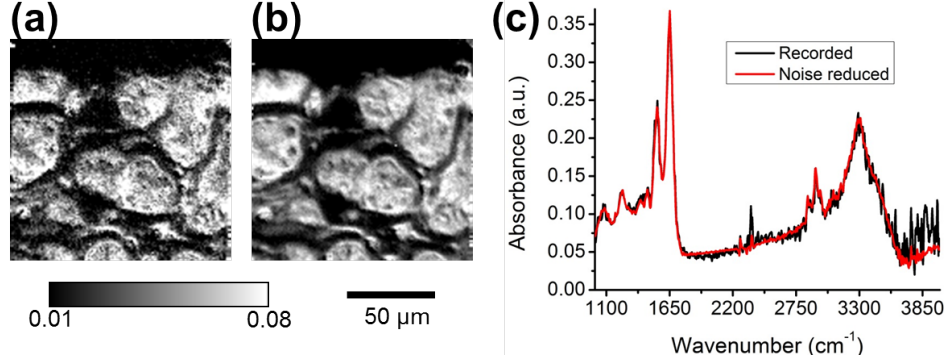
Fig. 6. Infrared spectroscopic imaging data from breast tissue before and after noise reduction. (a) An absorbance image at the asymmetric C-H stretching mode before noise reduction and the corresponding image (b) after noise reduction. (c) Spectra corresponding to recorded data and data after noise reduction from the same pixel.

absorbance of the asymmetric C-H stretching vibrational mode (at 2962 cm^{-1}). The top row demonstrates the improvement in image quality attained using the higher NA lens. There are relatively higher spatial frequencies present in the data acquired with the higher NA lens, signifying that there is information loss in increasing the pixel size from 1.115 μm to 5.5 μm. There is a noticeable set of high spatial frequencies present in the data acquired at the higher NA at the shorter wavelength. Even for longer wavelengths, the information content difference is relatively small, but not zero. To capture the highest image quality across the spectrum, hence, the pixel size should be calculated based on the highest wavenumber measured in the experiment. This statement is both rigorously and intuitively correct. From a practical perspective, however, a small pixel size calculated at the highest wavenumber also reduces the throughput significantly across the rest of the spectrum. To address this trade-off in an optimal manner, we recommend that the highest wavenumber at which pixel size should be calculated should depend on the typical experiments to be performed by the imaging system. This small adjustment from the correct sampling at the highest *recorded* wavenumber to that at the highest *usable* wavenumber for image generation leads to the concept of an optimal pixel size. For most studies in the mid-IR, the $4000 - 400$ cm^{-1} spectral region is most interesting. For He-Ne laser reference-based systems, an undersampling of the reference signal by a factor of 4 typically implies that the allowable free scanning spectral range is $3950 - 0$ cm^{-1}. An optimal pixel size at the high end of this range is 0.974 μm. In most experiments, especially with biological systems, vibrational modes at this high limit are very rarely encountered. A more practical high-wavenumber region is 3400 cm^{-1}, which is in the vicinity of the absorption peak of O-H and N-H stretching-associated vibrational modes.

18

Therefore, we calculate the optimal pixel size at this wavenumber and the predicted pixel size is 1.13 μm on a side. Since we sought to implement the concept of optimal pixel sampling on a commercial imaging system without extensive hardware modifications, the measured pixel size of 1.115 μm can be deemed acceptably close. Our suggested optimal pixel size is approximately 4-fold larger than a similar setup using the synchrotron. It is notable that intensity considerations are secondary for a synchrotron source-based system due to the exceptional flux and a pixel size of 0.54 micrometer on a side was used. Relaxing the very strict condition with a more practical calculation here, we maximize the spectral quality when using a globar source without comprising on the image quality in any appreciable manner. The image quality presented here, is likely of the highest quality that will be observed in commonly analyzed biomedical, materials or forensic samples regardless of the source.

Though image quality is improved with a smaller pixel size, there is a corresponding decrease in throughput if the same source and fore-optics are employed. The approximate 25-fold reduction in pixel area between the two configurations here implies that acquisition time would need to be increased 625-fold (other factors being constant) if the data quality is to be recovered by signal averaging.[26,27] Some of the loss is mitigated by increased throughput, as proposed using a synchrotron,[13] or by increased integration time of the FPA, as in the experiments conducted here. We observed a 6-8 fold decrease in recorded signal when using the higher NA lens, compared to the lower NA system. Hence, the need to signal average is not especially drastic. Further, there are other methods to increase the SNR. We have previously proposed computational noise reduction[28,29] to obtain a significant gain in SNR without the corresponding increase in data collection time. The utility of this idea is presented in Fig. 6. A significant increase in spectral SNR (Fig. 6(c)) without observable loss in image quality (Fig. 6(a) and (b)) can be observed. Thus, a desktop high-definition IR imaging system is indeed feasible and can provide both excellent spectra and spatial image quality.

5 Conclusions

A complete theoretical understanding of the image formation in an IR microscope is provided using a rigorous theoretical model. The model was used to predict the optimal pixel size at the sample plane that would provide the highest image quality. Simulations demonstrated that the effects of the higher NA systems arose from an increased acceptance of angular frequencies and resulted in higher resolution images whereas

optimal pixel sampling demonstrated dramatic improvements in image detail for a specific NA. The results of simulations were validated using measurements on two different configurations. A table-top, high-definition FT-IR spectroscopic imaging system was demonstrated by minimally modifying a commercial system. The resulting data using this high-definition system can be of high spatial and spectral quality using conventional signal averaging and/or emerging signal processing methods. The development of a theoretical understanding and its application to design of microscopes and acquisition of high-definition data should spur improved applications in many fields where IR imaging is applied.
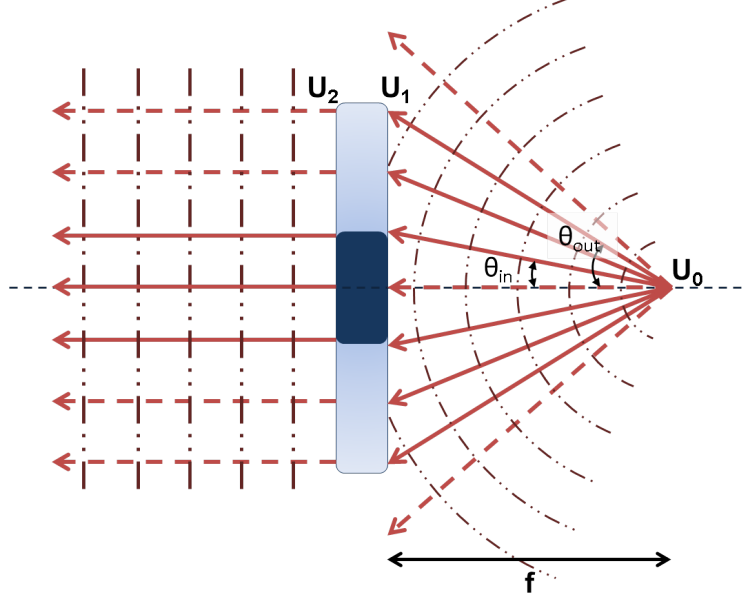
Acknowledgment

Fig. 7. A Cassegrain model. A point source placed at the focus results in a plane wave. The outer and inner numerical aperture limit the angles that enter the Cassegrain.

A Appendix

A.1 Derivation of the transfer function of the Cassegrain

We model the Cassegrain as a focusing system with two concentric apertures, one outer aperture with $NA_{out} = \sin(\theta_{out})$ and a second inner circular obstruction with $NA_{in} = \sin(\theta_{in})$ (see Fig. 7). The focal length, which is the distance between the Cassegrain and the focal point, is assumed to be known.

Consider an object placed a distance d_1 from the Cassegrain as shown in Fig. 8. Let the field in a plane perpendicular to the principal axis at the object be $|U_0\rangle$. The field, $|U_1\rangle$, just before the Cassegrain is given by

$$|U_1\rangle = \mathbf{K}_{d_1} |U_0\rangle. \tag{21}$$

The field immediately after the Cassegrain, $|U_2\rangle$, can be expressed in terms of $|U_1\rangle$ and an operator, $\mathbf{G}_C$,
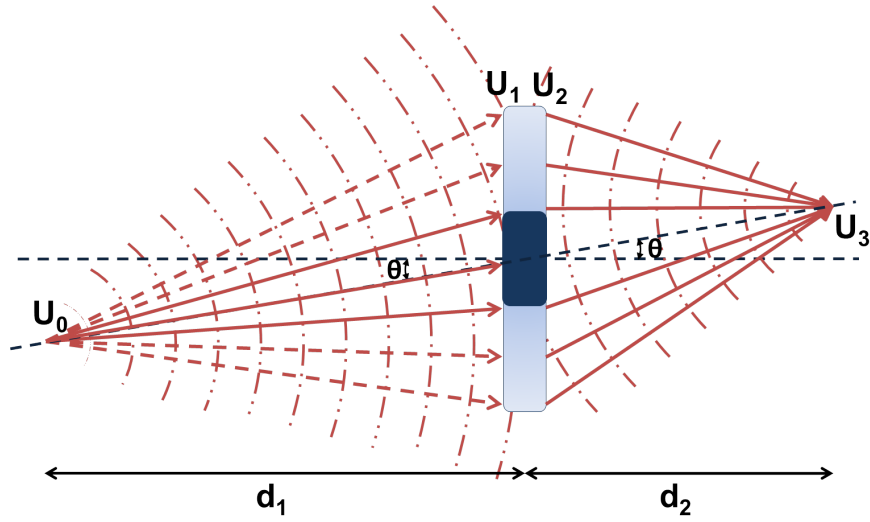
Fig. 8. An object placed at distance d_1 from the Cassegrain produces an image at position d_2 on the other side.
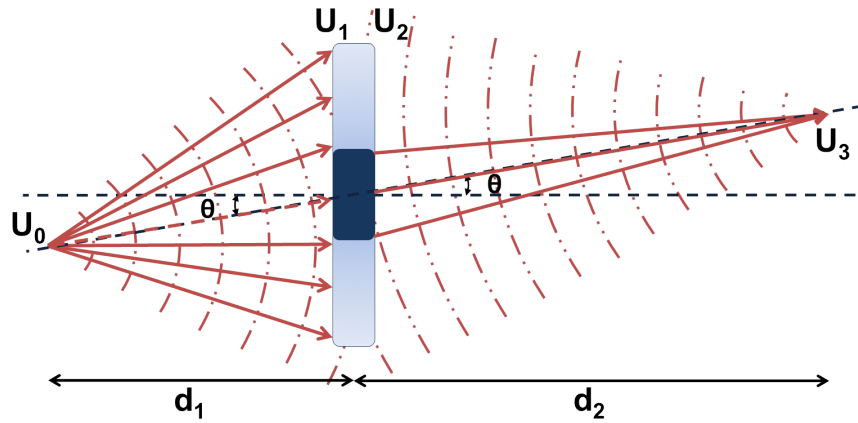

Fig. 9. The Cassegrain is flipped and the object distance d_1 is larger than the image distance d_2 on the other side. Equivalently, a larger range of angles are accepted by the Cassegrain from the object side

corresponding to the transmission function of the Cassegrain as

$$|U_2\rangle \;=\; \mathbf{G}_C\,|U_1\rangle \tag{22}$$

$$\mathbf{G}_C \;=\; \int d^2 r\,|\mathbf{r}\rangle\,Q_C(\mathbf{r})\exp\left[-i\frac{\pi\bar\nu}{L_f}r^2\right]\langle\mathbf{r}| \tag{23}$$

where L_f is the focal length of the Cassegrain. Note that the quadratic phase function in Eq. 23 is present because we have used a thin lens like approximation for the focusing system. $Q_C(\mathbf{r}) = Q_{R_1}^{R_2}(\mathbf{r})$ is defined in Eq. 24 and R_1 and R_2 are the inner and outer aperture radii.

$$Q_a^b(\mathbf{r}) = \begin{cases} 1 & a < r < b \\ 0 & else \end{cases} \tag{24}$$

The field $|U_3\rangle$ in the image plane is

$$|U_3\rangle \;=\; \mathbf{K}_{d_2}\,|U_2\rangle. \tag{25}$$

The term $f_z(\mathbf{f})$ in $\mathbf{K}_d$ can be approximated as $f_z(\mathbf{f}) \approx \nu\left(1 - \frac{f^2}{2\bar\nu^2}\right)$. After substituting Eq. 22 and Eq. 21 in Eq. 25 and simplifying we get

$$
\begin{aligned}
|U_3\rangle \;=\;& \mathbf{K}_{d_2}\mathbf{G}_C\mathbf{K}_{d_1}\,|U_0\rangle \\
=\;& \int d^2 r\, d^2 r'\, d^2 r''\,|\mathbf{r}\rangle\,Q_{R_1}^{R_2}(\mathbf{r}')\,\langle\mathbf{r}'|U_0\rangle \exp\left[i\frac{2\pi\bar\nu}{d_1}\mathbf{r}\cdot\mathbf{r}'\right]\exp\left[i\frac{2\pi\bar\nu}{d_2}\mathbf{r}''\cdot\mathbf{r}\right] \\
& \exp\left[i\frac{2\pi\bar\nu}{2d_2}r''^2\right]\exp\left[i\frac{2\pi\bar\nu}{2d_1}r'^2\right]\exp\left[i\frac{2\pi\bar\nu}{2}\left(\frac{1}{d_1}+\frac{1}{d_2}-\frac{1}{L_f}\right)r^2\right].
\end{aligned}
\tag{26}
$$

This is the relation between the image and the object for a Cassegrain. In most FT-IR imaging systems, we can make a few approximations and simplify Eq. 26. The object size (illuminated area of the sample) is typically much smaller than the size of the Cassegrain. This means that $\exp\left[i\frac{2\pi\bar\nu}{2d_1}r'^2\right] \approx 1$. The image size is also much smaller than the Cassegrain dimensions; therefore, $\exp\left[i\frac{2\pi\bar\nu}{2d_2}r''^2\right] \approx 1$. We know that [30] for a thin lens (or, more generally, for a system which focuses light like a thin lens), the position of the image and object are related by $\frac{1}{d_1}+\frac{1}{d_2}=\frac{1}{L_f}$. Therefore $\exp\left[i\frac{2\pi\bar\nu}{2}\left(\frac{1}{d_1}+\frac{1}{d_2}-\frac{1}{L_f}\right)(x^2+y^2)\right]=1$.

With these approximations, Eq. 26 reduces to

$$|U_3\rangle = \int d^2r d^2r' d^2r'' \, |\mathbf{r}\rangle \, Q_{R_1}^{R_2}(\mathbf{r}') \, \langle \mathbf{r}'|U_0\rangle \exp\left[i\frac{2\pi\bar{\nu}}{d_1}\mathbf{r}\cdot\mathbf{r}'\right] \exp\left[i\frac{2\pi\bar{\nu}}{d_2}\mathbf{r}''\cdot\mathbf{r}\right]. \tag{27}$$

Defining magnification $M = \frac{d_2}{d_1}$ and evaluating this integral after projecting on the Fourier basis yields

$$\langle \mathbf{f}|U_3\rangle = Q_{R_1}^{R_2}\left(-\frac{\mathbf{f}d_2}{\bar{\nu}}\right) \, \langle -M\mathbf{f}|U_0\rangle. \tag{28}$$

It may be noted that the system is linear, but *not* shift invariant (because of the magnification term). With this caveat, we can think of $Q_{R_1}^{R_2}\left(-\frac{\mathbf{f}d_2}{\bar{\nu}}\right)$ as the Cassegrain transfer function. In our model, the exact values of focal lengths are not required provided that the system is in focus. Only the outer and inner numerical apertures of the Cassegrains and the magnification factors are required.

For a Cassegrain with an orientation as in Fig. 8, typically the image is close to the focus. Thus, we can make approximations that $d_2 \approx L_f$ (L_f is focal length), $\text{NA}_{out} \approx \frac{R_2}{d_2}$ and $\text{NA}_{in} \approx \frac{R_1}{d_2}$. Also note that Q is an even function. This gives

$$\langle \mathbf{f}|U_3\rangle = Q_{\bar{\nu}\text{NA}_{in}}^{\bar{\nu}\text{NA}_{out}}(\mathbf{f}) \, \langle -M\mathbf{f}|U_0\rangle. \tag{29}$$

Note that propagation in free space is a spatial frequency bandpass $Q_0^{\bar{\nu}}(\mathbf{f})$ and spatial frequencies beyond $\bar{\nu}$ do not reach the detector. For a Cassegrain with an orientation as in Fig. 9, the object is close to the focus and so we can make the approximations that $d_1 \approx L_f$, $\text{NA}_{out} \approx \frac{R_2}{d_1}$ and $\text{NA}_{in} \approx \frac{R_1}{d_1}$. This gives

$$\langle \mathbf{f}|U_3\rangle = Q_{\bar{\nu}\text{NA}_{in}}^{\bar{\nu}\text{NA}_{out}}(M\mathbf{f}) \, \langle -M\mathbf{f}|U_0\rangle \tag{30}$$

$$\langle -\mathbf{f}/M|U_3\rangle = Q_{\bar{\nu}\text{NA}_{in}}^{\bar{\nu}\text{NA}_{out}}(\mathbf{f}) \, \langle \mathbf{f}|U_0\rangle. \tag{31}$$

A.2 List of Symbols

Symbol	Description
$\bar{\nu}$	Wavenumber
NA	Numerical Aperture
$\mathbf{r} = (x, y)$	Coordinate space variables
$\mathbf{f} = (f_x, f_y)$	Transverse spatial frequency variables
f_z	Longitudinal spatial frequency variable
$|U_{z_i}\rangle$	Field in a plane at $z = z_i$
$|S\rangle$	Sample
Q_{C_i}	Aperture function of Cassegrain C_i
M_{C_i}	Magnification of Cassegrain C_i
$\mathbf{K}_z$	Propagation operator
$\mathbf{I}_{d_1, d_2}$	Operator for the interferometer
$\mathbf{H}_{C_i}$	Transfer function (operator) for a Cassegrain C_i in focus
$\mathbf{G}_{C_i}$	Transmission function (operator) of Cassegrain C_i

Table 2. A list of symbols used along with their description

A.3 Point Spread Functions and Resolution

Point spread functions for the two configurations in table 1 are presented in Fig. 10. Simulation data for two point objects separated by four different distances is presented in Fig. 11 and Fig. 12. Data in Fig. 11 corresponds to the high NA configuration in table 1 and Fig. 12 corresponds to the lower NA configuration. All data is at 3950 cm^{-1}. Axes in all the images are scaled to the effective size of the detector-intensity-image at the sample. From these images it is evident that two points separated by 1 μm cannot be resolved using either $\text{NA}_{C_2 out} = 0.65$ or $\text{NA}_{C_2 out} = 0.5$, whereas they can be resolved in both configurations at a separation of 4 μm. However, $\text{NA}_{C_2 out} = 0.65$ can resolve two points separated by 2.4 μm (which is the resolution according to Rayleigh criterion), while $\text{NA}_{C_2 out} = 0.5$ cannot. Points at a separation of 3 μm can be just resolved using $\text{NA}_{C_2 out} = 0.5$. Data presented here illustrates the best image quality obtainable from systems with the optical configurations in table 1 without discretization (i.e using an analog detector). Discretized data obtained at the optimal pixel size (as calculated in section 2.2) have all the information needed to construct images of this quality.
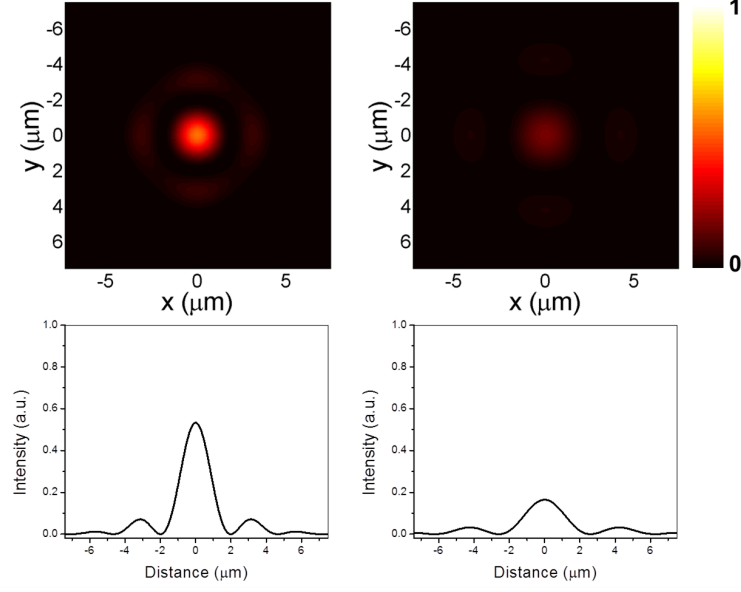
Fig. 10. Point spread functions. Data on the left corresponds to a configuration with $\mathrm{NA}_{C_2 out} = 0.65$ and data on the right corresponds to a configuration with $\mathrm{NA}_{C_2 out} = 0.5$.
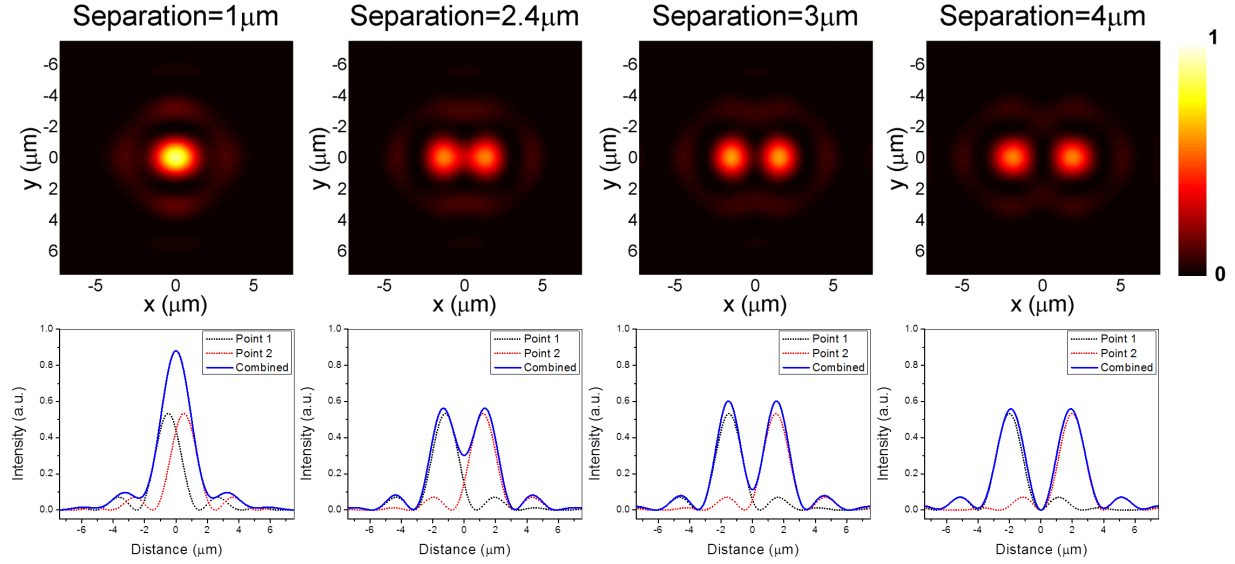

Fig. 11. Detector intensity at 3950 cm^{-1} for two point objects separated by distances indicated on top. Corresponding profile plots at $y = 0$ are presented in the bottom row. Cassegrain C_2 has $\mathrm{NA}_{C_2 out} = 0.65$. Axes are scaled to the effective image size at the sample.
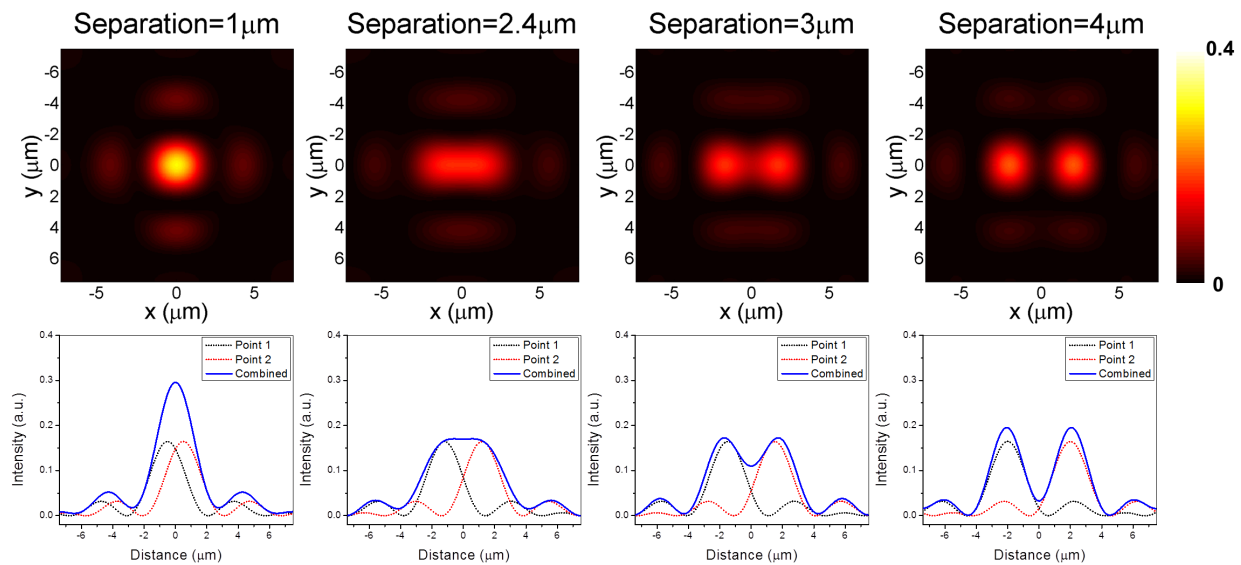
Fig. 12. Detector intensity at 3950 cm^{-1} for two point objects separated by distances indicated on top. Corresponding profile plots at $y = 0$ are presented in the bottom row. Cassegrain C_2 has $\mathrm{NA}_{C_2out} = 0.5$. Axes are scaled to the effective image size at the sample.

References

[1] E.N. Lewis, P.J. Treado, R.C. Reeder, G.M. Story, A.E. Dowrey, C. Marcott, and I.W. Levin, Anal. Chem. **67**, 19, 3377 (1995).

[2] R. Barer, A.R.H. Cole, and H.W. Thompson, Nature **163**, 4136, 198 (1949).

[3] R.C. Gore, Science **110**, 2870, 710 (1949).

[4] J.M. Kwiatkoski and J.A. Reffner, Nature **328**, 837 (1987).

[5] N. Jamin, P. Dumas, J. Moncuit, W.H. Fridman, J.L. Teillaud, G.L. Carr, and G.P. Williams, Proc. Natl. Acad. Sci. U.S.A. **95**, 9, 4837 (1998).

[6] G.L. Carr, Rev. Sci. Instrum. **72**, 1613 (2001).

[7] P. Dumas, N. Jamin, J.L. Teillaud, L.M. Miller, and B. Beccard, Faraday Discussions **126**, 289 (2004).

[8] F. Briki, B. Busson, L. Kreplak, P. Dumas, and J. Doucet, Cell. Mol. Biol. (Noisy-le-Grand, France) **46**, 5, 1005 (2000).

[9] L.M. Miller and P. Dumas, Biochim. Biophys. Acta **1758**, 7, 846 (2006).

[10] M. Offroy, Y. Roggo, P. Milanfar, and L. Duponchel, Anal. Chim. Acta **674**, 2, 220 (2010).

[11] R. Bhargava and I. Levin, *Spectrochemical Analysis Using Infrared Multichannel Detectors* (Wiley-Blackwell, 2005).

[12] C. Petibois, M. Cestelli-Guidi, M. Piccinini, M. Moenner, and A. Marcelli, Anal. Bioanal. Chem. **397**, 6, 2123 (2010).

[13] M.J. Nasse, M.J. Walsh, E.C. Mattson, R. Reininger, A. Kajdacsy-Balla, V. Macias, R. Bhargava, and C.J. Hirschmugl, Nat. Methods (2011).

[14] P. Lasch and D. Naumann, Biochim. Biophys. Acta **1758**, 7, 814 (2006).

[15] J. Widengren and U. Mets, *Single Molecule Detection in Solution* (Wiley Online Library, 2002).

[16] B.J. Davis, P.S. Carney, and R. Bhargava, Anal. Chem. **83**, 2, 525 (2011).

[17] B.J. Davis, P.S. Carney, and R. Bhargava, Anal. Chem. **82**, 9, 3474 (2010).

[18] R. Reddy, B. Davis, P.S. Carney, and R. Bhargava, IEEE International Symposium on Biomedical Imaging 738 (2011).

[19] B.J. Davis, P.S. Carney, and R. Bhargava, Anal. Chem. **82**, 9, 3487 (2010).

[20] J.W. Goodman, *Introduction to Fourier Optics* (Roberts & Company Publishers, 2005).

[21] P.A.M. Dirac, *The Principles of Quantum Mechanics* (Oxford University Press, 1958).

[22] I.W. Levin and R. Bhargava, Annu. Rev. Phys. Chem. **56**, 429 (2005).

[23] D.C. Fernandez, R. Bhargava, S.M. Hewitt, and I.W. Levin, Nat. Biotechnol. **23**, 4, 469 (2005).

[24] R. Bhargava, D.C. Fernandez, S.M. Hewitt, and I.W. Levin, Biochim. Biophys. Acta **1758**, 7, 830 (2006).

[25] R. Bhargava, R. Schwartz Perlman, D.C. Fernandez, I.W. Levin, and E.G. Bartick, Anal. Bioanal. Chem. **394**, 8, 2069 (2009).

[26] R. Bhargava and I.W. Levin, Anal. Chem. **73**, 21, 5157 (2001).

[27] P.R. Griffiths and J.A. De Haseth, *Fourier Transform Infrared Spectroscopy* (John Wiley & Sons, 1986).

[28] R. Bhargava, S.Q. Wang, and J.L. Koenig, Appl. Spectrosc. **54**, 4, 486 (2000).

[29] R.K. Reddy and R. Bhargava, Analyst **135**, 11, 2818 (2010).

[30] B.E.A. Saleh and M.C. Teich, *Fundamentals of Photonics* (John Wiley & Sons, 2007).